Université d'Ottawa · University of Ottawa

Excitonic Effects in Cu_2O:

Scattered Light, Resonant Absorption, and Bose-Einstein Condensate Amplification

By

©André Merizzi

Thesis submitted to the
Faculty of Graduate and Postdoctoral Studies
in partial fulfillment of the requirements
for the degree of Master of Science in Physics

Department of Physics

University of Ottawa
Ottawa, Ontario
December 10, 2001

Abstract

Experimental results are presented on excitonic effects related to the Bose-Einstein condensation (BEC) of excitons in Cu_2O. Such effects include resonant light polarization dependent absorption, exciton creation and diffusion by absorption of scattered light, and resonant high density exciton packet induced absorption. These results are then utilized, in conjunction with similar results on excitonic BEC, to develop a plausible model for condensate amplification. Condensates are initially created at T=1.8K with high intensity ND:YAG pulses ($\lambda = 532\,nm$) and then stimulated by a secondary source tuned around the 1S orthoexciton resonance ($\lambda = 609.51\,nm$); the latter induces the observed condensate amplification. By careful analysis of the various interactions between the secondary light source, the crystal, and the condensate itself, an improved understanding of how the secondary pulse excitations interact with the passage of a high density exciton packet is obtained.

Sommaire

Des resultats expérimentaux portant sur les effects excitoniques qui se relient à la condensation de Bose-Einstein (CBE) seront présentés. De tels effets incorporent la dépendance en polarization de l'absorption de lumière resonnante, la création et la diffusion d'excitons créés par de la lumière diffusive, et l'absorption différentielle induite par la présence d'un paquet excitonique de haute concentration. Ces résultats, en conjonction avec des résultats semblables portant sur la CBE excitonique, sont par la suite utilisés afin de développer un modèle plausible pour le phénomène d'amplification d'un condensat. Le condensat est initiallement créé à basse température (T=1.8K) à l'aide de pulses intenses générés par un laser ND:YAG (λ=532nm). Il est ensuite stimulé par une seconde source lumineuse réglée près de la résonnance des orthoexciton 1S (λ=609.51nm); cette deuxième source est strictement responsable du phénomène d'amplification. Une étude poussée des interactions multiples présentes entre la seconde source, le cristal, et le condensat, mène à une meilleure compréhension des interactions qui ont lieu entre la source lumineuse secondaire et le passage d'un paquet excitonique de haute concentration.

Remerciements

J'aimerais d'abords remercier Dr. Emery Fortin pour son aide et son encouragement tout au long de ce projet. J'aimerais également remercier Mathieu Massé, Pierre Leblanc et Luc Charron pour leur aide au laboratoire et pour les plusieurs discussions pertinantes que nous avons entretenues a l'égars de ce projet. Je remercie Laurette McCormick pour sa présence et son support durant ces derniers mois. Finalement, je remercie mes parents, sans qui je n'aurais pu completer mes études avec tant de succès.

Statement of Originality

Unless otherwise stated the results presented in this thesis come from experiments performed by the author at the University of Ottawa. Some of the results printed in this thesis were presented at the following conferences:

- Excitonic Peer Pressure: Using it to Your Advantage, A. Merizzi, CUPC conference at the University of Alberta, November 2000.
- Amplification of an Excitonic Bose-Einstein Condensate Cu_2O by Sequential Orthogonal Excitation, A. Merizzi, M. Massé and E. Fortin, APS conference in Seattle, WA, March 2001.
- Excitonic Effects in Cu_2O: Scattered Light, Resonant Absorption, and Bose-Einstein Condensate Amplification, A. Merizzi, OCIP Graduate Student Seminar, December 2001.

Results have also been presented in the following publication:

- Anomalous Optical Absorption in Cu_2O in the Presence of an Excitonic Bose Condensate, A. Merizzi, M. Massé, E. Fortin *Solid State Communications* , **120-11**, 419 (2001).

Contents

List of Figures

List of Tables

Introduction

Bose-Einstein condensation (BEC) of excitons has been an interesting topic in both experimental and theoretical research for the past few years [1, 2]. In particular, excitons in Cu_2O have been shown to be suitable candidates for BEC studies [3, 4, 5], where excitonic superfluidity was observed experimentally through ballistic propagation of excitonic packets at near sonic velocities ($4.5 \times 10^6 mm/sec$) [3] . Significant condensate amplifications were also observed using resonant secondary continuous wave (CW) excitation [5, 6]. Various theories have since been put forth to explain such experimental results [7, 8, 9, 10, 11], including recently proposed exciton-phonon coupling effects [12]. Recent results have focussed on the use of resonant pulses, as opposed to the CW illumination mentioned above, making spatial condensate probing possible by careful time-delayed stimulation [13, 14]. Although extensive work has been done to characterize and to better understand the condensate and its environment [6, 14], further experiments are required to fully comprehend the processes involved in condensate amplification and the effects surrounding probe-condensate interactions.

Cu_2O excitons are suitable for BEC studies for many reasons. For starters, they present an easily available boson system through photon absorption. In addition, their low effective mass permits condensation to occur at relatively high temperatures ($2K$) obtainable in superfluid ^4He. Finally, 1S paraexciton (spin zero) decay to the ground state is forbidden, resulting in a long exciton lifetime. This then permits exciton transport experiments to take place over long distances.

Previous experimental works on excitonic BEC by Benson [6] and Massé [14] have mainly concentrated on the various parameters that influence and control the initial condensation of a high density exciton packet in Cu_2O. Namely, their work verified the critical exciton density requirements for condensation with temperature, for pump wavelengths at $532 nm$ and $585 nm$. Such results lead to the convincing conclusions that observed excitonic signals were in fact produced by ballistic exciton condensates. In addition, work was also conducted on spatial interference between two such condensates, a

clear proof of quantum coherence. Finally, some initial work was presented on condensate amplification by secondary CW and pulsed excitation, and NDA, the normalized differential attenuation of the secondary amplifying pulses. These results provide the starting block for the present thesis, which seeks to thoroughly examine and qualify condensate amplification by pulsed secondary optical excitation and the various interactions that take place between the condensate and the amplifying stimulus. Careful attention is then given to three types of measurements. The first deals with the measured differential attenuation of the secondary excitation induced by the passage of an exciton packet, the second, with excitonic signals provided by the absorption of scattered light within the crystal volume, and the third, with excitonic signals provided by the travelling packet itself. By studying the variation of these results with such parameters as probe wavelength, intensity and polarization, as well as packet-probe synchronization, a better understanding of what actually happens inside the crystal when an exciton packet is stimulated by a secondary light source can be attained.

The thesis is divided into five chapters. The first provides a brief, yet adequate coverage of the theoretical concepts relevant to the experiments; such topics include Bose-Einstein Condensation (BEC), excitons, and the amplification of a Bose condensate. In the second chapter, the lasers, sample preparations, and experimental setups will be presented, followed by a brief description of the various preliminary equipment tests conducted to suppress unwanted experimental misinterpretations. Chapter three presents the first of the results, concentrating on single laser experiments. The chapter will discuss results obtained through the lateral excitation of Cu_2O samples by a pulsed laser beam tuned near the exciton resonance and around the exciton band edge; measurements are aimed at characterizing the optical absorption and light scattering properties of our samples within the spectral region of interest of $600 - 615\,nm$. Chapter four will then present results related to double excitation experiments. Condensates created with an initial YAG pulse are probed by a secondary pulse tuned either around the exciton resonance or near the exciton absorption edge. Studied secondary pulse related effects include condensate amplification, and the normalized differential attenuation (NDA) of the secondary pulse induced by the passing of a travelling condensate. Finally, a fifth chapter is provided, offering a final analysis of results needed to formulate a revised model believed to adequately explain condensate amplification. It will incorporate results, both from the present thesis and from previous works by Benson [6] and Massé [14], on amplification and on NDA, leading to an improved understanding of how the secondary pulse excitations interact with the passage of a high density exciton packet.

Chapter 1

Theory

This first chapter provides a brief, yet adequate coverage of the theoretical concepts relevant to the experimental results presented in this thesis. First, general Bose-Einstein condensation theory will be presented using an ideal bose gas as an approximation for our system. This will be followed by a look at excitons and excitonic BEC in Cu_2O. Finally, condensate amplification will be discussed.

1.1 Bose-Einstein Condensation

Although the aim of this project is not directly to study the Bose-Einstein condensation of a particular system, it does involve the observation of excitonic condensate amplification, and related condensate-induced effects. Previous experimental works have thoroughly observed and analyzed the basic system, consisting of single, exciton Bose condensates. This project takes their work as a starting block, and assumes that their results and conclusions are right. Despite this, it is important to have a good knowledge of the basis before moving further. A brief introduction to BEC is therefore presented in this first section.

1.1.1 Bosons

To properly study particle interactions at low temperatures and at high densities, one must take into account related quantum effects. In this regime, particle wave functions dictate the types of interactions that can take place in a given system. Quantum particles divide into two main categories: fermions (half-integer spin particles) and bosons (integer spin particles). The fermion wave function is odd under particle exchange,

$$\Psi(\vec{r_1}, \vec{r_2}) = -\Psi(\vec{r_2}, \vec{r_1}), \tag{1.1}$$

whereas that for the boson is even.

$$\Psi(\vec{r_1}, \vec{r_2}) = \Psi(\vec{r_2}, \vec{r_1}). \tag{1.2}$$

The wave function symmetry of fermions and bosons leads to their two main properties; in fermionic systems, quantum degeneracy is forbidden by the Pauli exclusion principle, whereas for bosonic systems, it is actually encouraged. These effects are sometimes respectively termed statistical repulsion and statistical attraction. For bosons, this effect can become precipitous at high density and low temperature, leading to Bose-Einstein condensation. Unlike regular states of matter, a Bose condensate's behavior is governed by quantum statistical mechanics and can not be compared to typical everyday materials. For example, a condensate will take the form of a superfluid, in which viscosity goes to zero, resulting in a drag free motion.

1.1.2 Ideal Bose Gas

An ideal Bose gas consists of noninteracting bosons in a system where quantum statistics govern the behavior of the particles. Experimental conditions presented in this paper are well approximated by this model. Starting with the boson partition function, we will eventually derive the equations of state for an ideal Bose gas, which in turn, can predict the basic properties of an ideal quantum gas. The boson partition function L, in the Grand Canonical Ensemble is given by:

$$L(z, V, T) = \sum_{N=0}^{\infty} z^N e^{-\beta \sum \epsilon_{\vec{p}} f_{\vec{p}}} = \prod_{\vec{p}} \left[\sum_{f_{\vec{p}}} \left(z e^{-\beta \epsilon_{\vec{p}}} \right)^{f_{\vec{p}}} \right], \tag{1.3}$$

where N is the number of particles, V the volume, T the temperature, $f_{\vec{p}}$ is the occupation number of a state with energy $\epsilon_{\vec{p}}$, $\vec{p}$ is the momentum, β is equal to $\frac{1}{k_B T}$ and z is the fugacity (the fugacity is related to the chemical potential μ by $z = e^{\beta\mu}$). The total number of particles is limited by the condition $\sum f_{\vec{p}} = N$, as the sum of occupation numbers must return the total number of particles. For bosons, $f_{\vec{p}}$ is any positive integer, state degeneracies are unlimited. The sum over $f_{\vec{p}}$ is a geometric series $\left(\sum_{s=0}^{\infty} r^s = \frac{1}{1-r}\right)$ reducing the partition function for bosons to:

$$L(z, V, T) = \prod_{\vec{p}} \frac{1}{1 - z e^{-\beta \epsilon_{\vec{p}}}}. \tag{1.4}$$

We can then obtain the equations of state:

$$\frac{PV}{k_BT} = \log L(z,V,T) = -\sum_{\vec{p}} \log(1 - ze^{-\beta\epsilon_{\vec{p}}}), \tag{1.5}$$

$$N = z\frac{\partial}{\partial z}\log L(z,V,T) = \sum_{\vec{p}} \frac{ze^{-\beta\epsilon_{\vec{p}}}}{1 - ze^{-\beta\epsilon_{\vec{p}}}}. \tag{1.6}$$

In the limit as $V \to \infty$ the possible values of $\vec{p}$ form a continuum and the sum over $\vec{p}$ in equations 1.5 and 1.6 is replaced by an integration such that $\sum_{\vec{p}} \to V \cdot \frac{2s+1}{h^3} \int d^3\vec{p}$ where s is the particle spin and h is Planck's constant. Equations 1.5 and 1.6 can be rewritten to give:

$$\frac{P}{k_BT} = -\frac{4\pi \cdot (2s+1)}{h^3} \int_0^\infty dp\, p^2 \log(1 - ze^{-\beta p^2/2m}) - \frac{1}{V}\log(1-z), \tag{1.7}$$

$$n = \frac{4\pi \cdot (2s+1)}{h^3} \int_0^\infty dp\, p^2 \frac{1}{z^{-1}e^{\beta p^2/2m} - 1} + \frac{1}{V}\frac{z}{1-z}. \tag{1.8}$$

where $n = N/V$ is the density.

The ground state term has been taken out of the sum before it was converted to an integral. This is done since the boson ground state term can be as important as the rest of the states. One can now integrate equations 1.7 and 1.8, providing the relations between pressure(P), density(n), temperature(T) and fugacity(z) for an ideal Bose gas.

$$\frac{P}{k_BT} = \frac{(2s+1)}{\lambda^3} g_{5/2}(z) - \frac{1}{V}\log(1-z), \tag{1.9}$$

$$n = \frac{(2s+1)}{\lambda^3} g_{3/2}(z) + \frac{1}{V}\frac{z}{1-z}, \tag{1.10}$$

$\lambda = \sqrt{\frac{2\pi\hbar^2}{mk_BT}}$ is the thermal wavelength and $g_n(z) \equiv \sum_{l=1}^{\infty} \frac{z^l}{l^n}$.

From the partition function 1.3, one can also derive the average occupation number $< f_{\vec{p}} >$ given by:

$$< f_{\vec{p}} > = -\frac{1}{\beta}\frac{\partial}{\partial \epsilon_{\vec{p}}} \log L = \frac{ze^{-\beta\epsilon_{\vec{p}}}}{1 - ze^{-\beta\epsilon_{\vec{p}}}}. \tag{1.11}$$

For the ground state ($\epsilon_{\vec{p}} = 0$), $< f_{\vec{0}} >$ is simply $z/(1-z)$. Equation 1.11 then becomes:

$$\frac{< f_0 >}{V} = n - \frac{2s+1}{\lambda^3} g_{3/2}(z). \tag{1.12}$$

where $g_{3/2}(z)$ increases monotonically over the range $z = 0 \ldots 1$ with $g_{3/2}(1) = 2.612$. Equation 1.12 implies that there is a finite number of particles in the ground state if:

$$n > \frac{2s+1}{\lambda^3} g_{3/2}(z). \tag{1.13}$$

This macroscopic occupation of the ground state is termed Bose-Einstein condensation. From 1.13, one finally obtains a temperature-dependent expression for the critical density above which particles in the ground state of an ideal Bose gas will condense.

$$n_c = 2.612 \cdot (2s+1) \cdot \left(\frac{mk_B}{2\pi\hbar^2}\right)^{3/2} T^{3/2}. \tag{1.14}$$

Dividing both sides of 1.13 by n, one can also determine the fraction of total particles within the condensate:

$$\frac{< f_0 >}{N} = 1 - \frac{2s+1}{n\lambda^3} g_{3/2}(z). \tag{1.15}$$

We then substitute $g_{3/2}(z)$ by $g_{3/2}(1)$ ($z \rightarrow 1$ for a non-zero condensed fraction), and use $g_{3/2}(1) = \frac{n\lambda_c^3}{2s+1}$, where λ_c is calculated at the critical temperature T_c, in equation 1.15 to obtain:

$$\frac{< f_0 >}{N} = \begin{cases} 1 - \left(\frac{T}{T_c}\right)^{3/2} & T \leq T_c \\ 0 & T \geq T_c \end{cases}. \tag{1.16}$$

Figure 1.1 shows a graphical representation of equation 1.16. For $T < T_c$, a fraction of the total particles occupy the ground state, whereas for $T > T_c$, none of the energy states is significantly degenerate. In the first case a condensate will form, and all remaining particles will spread thinly over the excited states. In the latter case, particles are spread over all available energies, and there is no condensation. This paper studies the condensation of $s = 0$ excitons (better known as paraexcitons) in Cu_2O crystals (discussed in section 1.2.2). In our experiments, initial exciton densities are estimated at approximately $10^{18}\, cm^{-3}$. Using this value for n_c in equation 1.14, and substituting m by the paraexciton mass of $2.7m_0$ [15], where m_0 is the mass of an electron, one obtains a critical temperature of approximately $T_c = 16\, K$. With equation 1.16, one calculates a condensed fraction of $\sim 95\,\%$ for a sample at $T = 2\, K$.

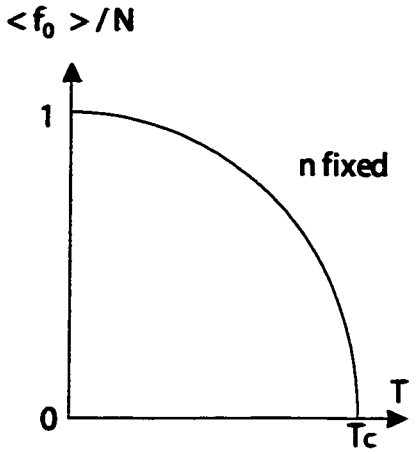

Figure 1.1: Average occupation of the ground state as a function of temperature.

1.2 Excitons

1.2.1 Semiconductor Band Structure

Electrons in a crystal are confined to energy bands generated by the periodicity of the lattice. These bands are separated by voids (know as band gaps) where energy states are forbidden; an electron can only move from one band to another if energy of equal or greater value than the band gap is provided to the system. Conduction is defined as an electron's ability to move within one of these bands under the influence of an electric field; this is only non-zero when there is at least one partially empty band. The lowest filled energy band is known as the valence band, and the next one above it, the conduction band. If the conduction band is empty, then electrons can not travel, and the material is characterized as an insulator. If the conduction band is partially filled, then it is a conductor. A semiconductor is characterized as being somewhere in the middle between the two above cases. Essentially, a semiconductor is an insulator for which thermal energy is generally sufficient to promote electrons from the valence band to the conduction band, providing a weak current in the presence of an electric field. This is generally the case for small band gap insulators, or again for doped insulators which exhibit semiconductor properties through the thermal excitation of embedded impurity states.

Semiconductor band gaps may be classified under two types: direct gaps and indirect gaps. As illustrated in figure 1.2, the bands are schematically plotted as functions of $\vec{k}$, the electron wave vector. In A), a direct transition is shown as a straight vertical line

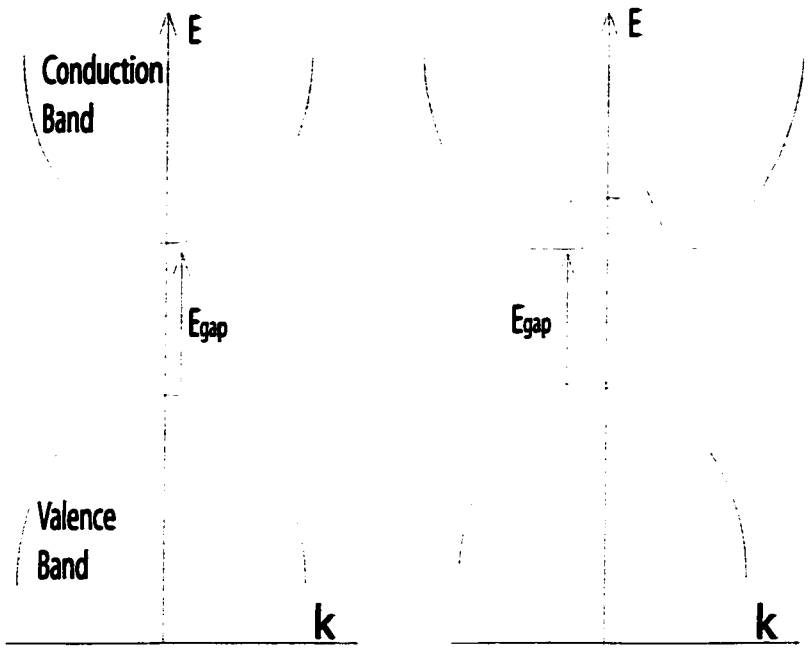

Figure 1.2: A) direct transition, B) indirect transition.

joining the maximum of the valence band and the minimum of the conduction band. This transition requires no change in $\vec{k}$; it may then occur by the simple absorption of a photon of energy $E_g = \hbar\omega_g$, where E_g is the band gap energy and where ω_g is the frequency of the resonant photon. In B), an indirect transition is depicted. The conduction band minimum is not centered over the valence band maximum, leading to phonon assisted transitions. Absorption is then only permitted by the emission or absorption of phonons, which induces the required change in electron momentum $\hbar\vec{k}$. Absorbed photons will then be of energies $\hbar\omega = E_g \pm E_{phonon}$ for emitted (+) and absorbed (-) phonons respectively. In any case, photon absorption is dictated by the electron transition probability between two states. This is then proportional to the density of states of the initial and final energy bands. Experimentally, one usually refers to the absorption coefficient, a measure of the relative light intensity loss for a given trajectory length within the absorptive medium. It is usually presented in the form of the Beer-Lambert equation given by:

$$I = I_0 e^{-\alpha x}, \tag{1.17}$$

where α is the absorption coefficient, and x is the distance travelled within the sample.

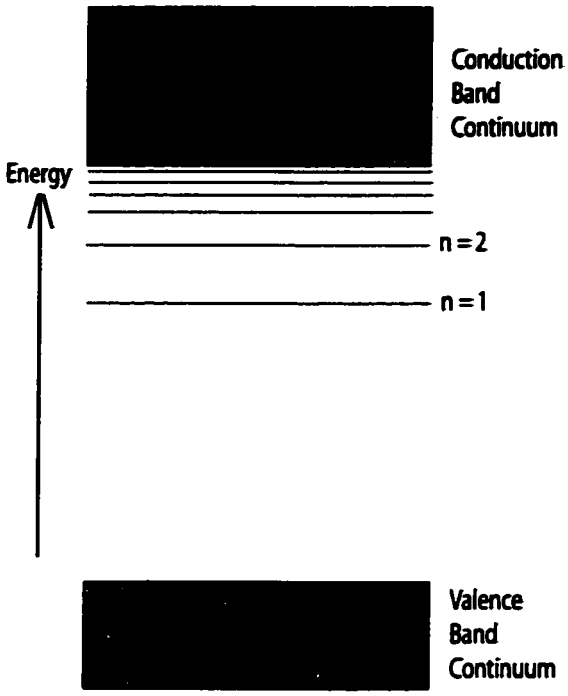

Figure 1.3: Exciton energy levels for $\vec{k} = 0$.

1.2.2 Excitons in Cu_2O

When an electron is excited into the conduction band, it is still relatively close to the hole it left behind in the valence band. Possessing opposite charge, they can bind together much like an electron and a proton do to form a hydrogen atom, in this case creating an exciton. Formed within a crystal, the Coulomb interaction between the two particles of an exciton is screened by the periodic lattice field. This new pair is of neutral charge and of spin 0 or 1; S=1 excitons are called orthoexcitons and S=0 excitons are called paraexcitons. Their binding energy, much like that of a hydrogen atom, is given by the following series:

$$E_B = \frac{e^4 \mu_{ex}}{2\hbar^2 \epsilon^2 n^2} \qquad n = 1, 2, 3, \ldots , \tag{1.18}$$

where e is the electronic charge, ϵ is the static dielectric constant of the medium ($\simeq 7$ in Cu_2O [16]) and $\mu_{ex} = m_e m_h/(m_e + m_h)$ is the exciton reduced mass where m_e and m_h are the electron and hole effective mass respectively. From equation 1.18, schematically represented in figure 1.3, one can see that the exciton energies are smaller than the band gap and will then permit the absorption of light at wavelengths otherwise expected to

be completely transmitted.

For the specific case of excitonic BEC in Cu_2O, the n=1 paraexciton is the best candidate (for reasons discussed in section 1.2.4). Yet, since the creation of $1S$ paraexcitons by direct single photon optical absorption is forbidden, one must resort to other indirect methods to create the exciton states of interest; three such processes are exploited in our experiments. Firstly, initial exciton densities are created at the sample surface using a pulsed YAG laser tuned at $532\,nm$. These light pulses generate high energy electron-hole pairs in the conduction band which gradually fall back to the 1S state through a series of phonon-emitting transitions. Paraexciton packets then travel (ballistically if condensation requirements are met) through the crystal (as will be discussed in the section 1.2.4) and are detected at the opposite crystal face (see section 2.2). The second and third methods involve the creation of orthoexcitons by either the phonon-assisted absorption of light tuned near the $n = 1$ exciton band edge ($\sim 605\,nm$) or the direct quadrupole-permitted absorption of light tuned at the orthoexciton resonance. The latter of the two processes invokes direct excitation of the $1S$ orthoexciton line, which is centered at $2.033\,eV$[1] and width of approximately $1\,\mu eV$ [17]. In both cases, the relatively short lived orthoexcitons either disassociate before reaching our exciton detector (see section 2.2), or down convert to the relatively longer lived paraexciton state of interest.

1.2.3 Polarization Dependent Aborption at the 1S Orthoexciton Resonance

Quadrupole-permitted photon absorption at the 1S orthoexciton energy in Cu_2O may be polarization dependent along a given crystalline direction. It is shown in [18] that the oscillator strength's proportional variation with crystal orientation can be expressed as:

$$f_{quad} \propto (1 - 2[(l_1 l_2)^2 + (m_1 m_2)^2 + (n_1 n_2)^2]) = Z \tag{1.19}$$

$$\vec{q} = [l_1, m_1, n_1]$$

$$\vec{\varepsilon} = [l_2, m_2, n_2]$$

[1]Note: Although this energy corresponds to a wavelength of $609.83\,nm$, absorption spectra taken on our samples present an absorption peak at approximately $609.51\,nm$, which corresponds to an energy of $2.034\,eV$ (section 3.1). The small difference in energy is likely attributed to a small calibration error in our equipment; yet, for continuity, we will hereafter refer resonance to the observed wavelength of $609.51\,nm$.

where $\vec{q}$ is the resonant light's wavevector and $\vec{\varepsilon}$ is its polarization vector in the crystal lattice frame. For example, if $\vec{q} \parallel [1\bar{1}0]$ and $\vec{\varepsilon} \parallel [110]$, $f_{quad} = 0$. If polarization is then turned, absorption will vary as a squared sinusoidal, reaching a maximum for $\vec{\varepsilon} \parallel [001]$. This effect is further discussed in section 2.3.1, verified in chapter 3 and utilized as an experimental tool in chapter 4.

1.2.4 Bose-Einstein Condensation of Excitons

Excitons created in ultra-pure semiconducting Cu_2O crystals are excellent candidates for BEC. Because of their small mass ($2.7 m_0$ [15]) and radius ($\approx 0.7 nm$ [19]), the criterion for the ideal bose gas approximation ($n r_{ex}^3 << 1$, where n is the exciton density and r_{ex} is the exciton radius) is satisfied for densities up to $10^{20} cm^{-3}$, well below maximum densities reached in this laboratory. Furthermore, due to the exciton's small radius, Mott dissociation (breakdown of the excitons into an electron-hole plasma at $n r_{ex}^3 \approx 0.3$) does not take place for $n < 10^{21} cm^{-3}$, and hence need not be considered in our experiments. The repulsive exciton-exciton potential reported in [20] also promotes the creation of excitonic condensates, as it discourages the formation of biexcitons and all other excitonic compounds, providing added stability to the exciton system. Finally, paraexciton condensates may be created and observed at relatively modest temperatures. Unlike atomic BEC, which requires temperatures in the nK range, excitonic BEC can be achieved at superfluid helium temperatures around $2K$. At this temperature, the critical density for condensation (equation 1.14) is of the order of $10^{17} cm^{-3}$. With the lasers presented in section 2.1, densities of $10^{16} \rightarrow 10^{19} cm^{-3}$ are obtained, permitting adequate study of the condensation process.

The initial YAG pulse generates a high density of excitons in the sample near the illuminated crystal face. This depth dependent density can be calculated as such: the density of excitons in a layer dx parallel to the illuminated surface is equal to the loss of photons by optical absorption in this region divided by dx (we assume that every absorbed photon generates one exciton). Using equation 1.17, and the fact that $I(x) \propto \frac{N(x)}{A}$ where $N(x)$ is the number of photons in the crystal at a distance x from the illuminated surface A, the density can be expressed as:

$$n(x) = -\frac{1}{A}\frac{d}{dx}N(x) = -\frac{1}{A}\frac{d}{dx}N_0 e^{-\alpha x} = \frac{\alpha N_0}{A}e^{-\alpha x} \tag{1.20}$$

where α is the absorption coefficient and N_0 is the number of incident photons. Due to the large absorption coefficient (α) at $\lambda = 532 nm$, the excitons will then be driven to

travel through the crystal by a large density gradient expressed as:

$$\Delta n(x) = \frac{d}{dx} n(x) = \frac{-\alpha^2 N_0}{A} e^{-\alpha x}, \tag{1.21}$$

If the density is sufficient for condensation, the exciton packet will travel through the crystal at rates approaching sonic velocity, ($v_s = 4.5 \times 10^5\, cm/s$ [21] in Cu_2O), displaying properties of superfluidity [3]. If the density is insufficient, the packet will still diffuse through the crystal, but at a slower velocity as drag is induced by the crystal.

Theoretical work by Loutsenko and Roubtsov [7] has brought forth plausible solutions for this system that seem to support the above contentions on excitonic BEC in Cu_2O. It takes into account the interactions between the excitons and phonons present in the crystal (also present in reported experiments). It predicts that for a given material there exists a critical velocity v_c, above which superfluidity is achieved. For Cu_2O, the predicted velocity is around $0.5 - 0.7 v_s$. Above the speed of sound, no solutions apply. Between v_s and v_c, stationary solutions are found, with a particle distribution described with a soliton shape:

$$n(x) = n_0 sech^2\left(\frac{x - x_0}{\Delta}\right) \qquad \frac{1}{\Delta} = \beta n_0, \tag{1.22}$$

with a peak position at x_0 and an amplitude n_0 related to its spatial width Δ by the parameter β. If $v < v_c$, the packet is then predicted to travel diffusively through the crystal, with a particle density described by the solution of a 1D diffusion equation with drift term.

In previous experimental works [6, 14], the above theoretical derivations have been justified. For modest densities, exciton packets are observed to travel diffusively through the samples at velocities below predicted critical values; packets were successfully fitted with the aforementioned 1D diffusive equation solutions. At higher densities, packets are observed to condense and to travel ballistically at velocities between the predicted $v_c$and the accepted value for v_s. A distinguishable kink in the variation of the packet velocity with initial exciton density is observed, providing a reasonable measure of the critical density required for condensation. The solitonic exciton distribution provided by equation 1.22 was also relatively successful in fitting the detected condensates. In a following work [12], it was determined that the soliton shape could be somewhat modified as the packet travelled through the crystal, manifested by the appearance of an incoherent tail formed behind the moving coherent part of the exciton packet (the condensate). This is in agreement with initial observations by Benson [6], who was first to bring forth the

comet analogy for our travelling condensate. It is predicted that the travelling packet is comprised of a condensed core, surrounded by a coma and followed by a tail of uncondensed excitons. This analogy will be useful when discussing condensate amplification by secondary laser pulse excitation (see sections 1.3, 2.4.5 and 4.1).

One observation remains to be made. While the condensate travels through the crystal, it will also be accompanied by a great number of phonons, generated by the initial pulse, which will travel throughout the crystal. In the works mentioned above [7, 12], such a phonon field was incorporated in calculations to properly describe our experimental system. What has not been fully derived, is the effect of a travelling high density exciton-phonon packet on the crystal itself. It is believed that the propagation of these packets could induce certain distortions in our samples. Results in chapter 4 will suggest that such perturbations include absorption line broadening and crystal symmetry breaking; these will be manifested by the observation of the differential optical absorption of a secondary light source, and the removal of polarization-dependent optical absorption for certain crystal orientations, in the presence of a condensate. Not only will these crystal effects present great means for exciton packet detection, they will also provide information on the the packet itself, and on condensate amplification, discussed in the next section.

1.3 Condensate Amplification

Previously discussed in section 1.1.1, bosons (excitons), unlike fermions, do not obey the Pauli exclusion principle preventing multiple occupancy of a given quantum state; this is what makes BEC possible. The probability for a boson to join a state already occupied by another boson increases linearly with the occupation number of the final state. Under the right conditions, this "attractive" behaviour may also become precipitous. Much like photons (massless Bose particles) can produce and amplify laser light, optically inactive paraexcitons, also called cold excitons, may participate in the amplification of an excitonic condensate.

As presented in [5], the basic spontaneous exciton scattering process combines the annihilation of an exciton of energy E_i and wavevector $\vec{K}_i$, the creation of an exciton of energy E_f and wavevector $\vec{K}_f$, and the simultaneous absorption or emission of an acoustic phonon. This is the basic chain of events when hot excitons are injected into the crystal. The initial exciton (E_i, $\vec{K}_i$) is coupled to a continuum of final states, defined by the set of vectors ($\vec{K}_f$, $\vec{q}$) which satisfy these conservation laws:

$$E_i = E_f \pm \hbar\omega_q \qquad \vec{K}_i = \vec{K}_f \pm \vec{q}, \tag{1.23}$$

constrained to:

$$E_{i,f} = \frac{\hbar^2 K_{i,f}^2}{2m_{eff}}, \qquad \hbar\omega_q = \hbar|\vec{q}|v_s, \tag{1.24}$$

where v_s is the longitudinal sound velocity and m_{eff} is the exciton effective mass. This scattering induces the diffusive motion of the exciton packet.

For the stimulated process, an incident exciton field (f_c, E_c, $\vec{K}_c$) induces the exciton scattering, where $f_c > 1$ is the occupation number of mode c. Conditions on E_f and $\vec{K}_c$ are given by:

$$E_f = E_c \qquad \vec{K}_f = \vec{K}_c \tag{1.25}$$

The time rate of change of the average number of bosons in mode c gives the growth of the bosonic rate [22]:

$$\frac{\partial f_c}{\partial t} = \frac{2\pi}{\hbar}\sum_q \gamma^2(q)\{f_{c+q}(1+f_c)[(1+f_q)\delta(\hbar\omega_q + E_c - E_{c+q}) + f_q\delta(\hbar\omega_q - E_c + E_{c+q})] \\ -(1+f_{c+q})f_c[(1+f_q)\delta(\hbar\omega_q - E_c + E_{c+q}) + f_q\delta(\hbar\omega_q + E_c - E_{c+q})]\} \tag{1.26}$$

where $f_i = f_{c+q}$ and f_q are respectively the occupation probability of excitons and acoustic phonons with energy E_q and $\hbar\omega_q$ and $\gamma(q) = \gamma_0\sqrt{q}$ is the matrix element of the exciton-phonons interaction. An excitonic Bose condensate with $f_c >> 1$ on the R.H.S. of equation 1.26 can provide the triggering term for stimulated excitonic transition. Yet, stimulated exciton scattering can still occur even below the Bose condensation threshold because modes near $\vec{K} = 0$ have already large occupation numbers in the quantum-degenerate statistical regime. The first and second terms in equation 1.26 account for the amplification and loss process respectively. Amplification occurs through stimulated exciton scattering induced by the excitonic field (f_c, E_c, $\vec{K}_c$), whereas the loss is expressed by excitons scattering out of the mode f_c by the creation of an exciton of wavevector $\vec{K}_c \pm \vec{q}$. The larger term governs the outcome: a gain, or a loss. One important point remains; in [23], it is shown that unlike a laser, stimulated emission can be observed at densities under the critical density for BEC.

In this thesis, efforts are concentrated on the characterization of the various parameters that govern and influence Bose condensate amplification. It is understood that cold

excitons injected into the crystal volume can interact with a travelling condensate to amplify it, but more needs to be known about which excitons in particular lead to the observed gains in excitonic signals. In chapters 3 and 4, results are aimed at isolating various parameters generated by the creation of excitons in various parts of the crystal and through various processes in and around the condensate. Signals generated by the absorption of scattered light will be used to observe the influence of excitons created throughout the crystal, and not necessarily close to the travelling packet, on amplification. In addition, careful attention will be brought to the observation of the differential attenuation of lateral and scattered light stimuli, induced by the passage of the initial exciton packet. Results will show that only excitons created in the near vicinity of the condensate and its surrounding uncondensed excitons will participate in condensate amplification; not only do these excitons scatter into the condensed state, but their addition to the travelling high density packet will further induce the condensation of initial high density incoherent excitons travelling in the comet-like packet coma and tail. In addition, the observation of absorption line broadening and crystal symmetry breaking in the presence of a travelling exciton packet will bring proof of condensate-induced local crystal distortions which may in fact play a role in amplification.

Chapter 2

Experiment

This second chapter presents an overview of the lasers and equipment used for our experimental work. It also describes the samples, their preparation, and the construction and function of the sample-mounted exciton detector. This is followed by a look at the various experimental setups required for the successful acquisition of the data presented in the next two chapters. The chapter then ends with a quick look at preliminary equipment tests conducted to suppress any possible experimental artifacts found in our data.

2.1 Lasers

2.1.1 Pulsed Lasers

The pulsed laser set utilized in our experiments consists of a Lumonics frequency doubled Nd:YAG laser ($\lambda = 532\,nm$) of pulse duration $\delta t \approx 10\,ns$ and a Lumonics Hyperdye 300 pulsed laser ($\delta t \approx 9\,ns$) pumped by the YAG; both lasers are vertically polarized. The latter is set to produce radiation in the visible, at wavelengths around the Cu_2O 1S orthoexciton resonance of $609.51\,nm$. Peak output powers for these two lasers are measured at approximately 15 MW and 3.5 MW for the YAG and Dye lasers respectively. These powers are measured as follows:

$$P_{peak} = \frac{P_{avg}}{f\delta t} \tag{2.1}$$

where P_{avg} is the measured average power on a conventional power meter, f is the laser repetition rate ($10\,Hz$ in this case) and δt is the pulse duration. For most cases, both the YAG and dye lasers are operated at the same time; only half of the YAG beam is then

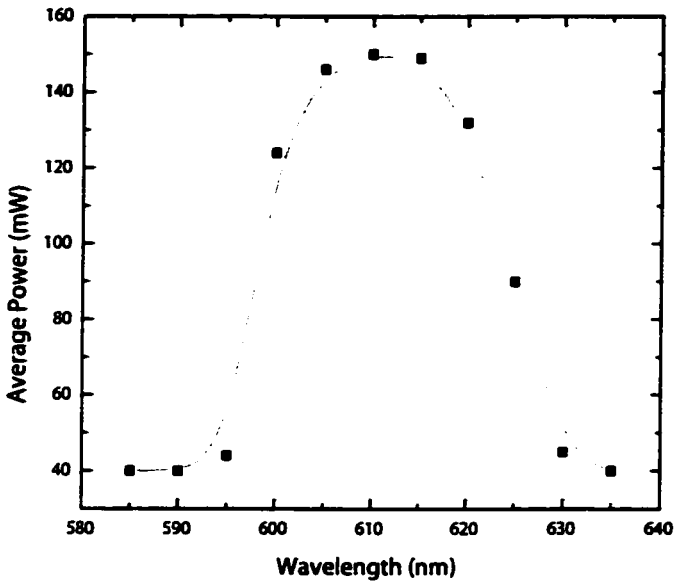

Figure 2.1: Pulsed dye laser average power variation over range of output wavelengths.

utilized for pumping, resulting in usable dye peak powers of approximately $1.7\,MW$. In the results sections, peak laser intensities, defined as:

$$I_{peak} = P_{peak}/A_{spot} \tag{2.2}$$

where P_{peak} is as defined in equation 2.1 and A_{spot} is the laser excitation spot area, will be reported instead of peak laser powers; generally, intensities will be given in units of $I_0 = 10^5\,W/cm^2$. In all cases, square pulse intensity profiles are assumed at the excitation spot, the laser beam generally being somewhat larger than the sample holder conduit available for sample excitation.

For the dye laser to produce the desired output wavelength range, a proper dye solution is made; it is a mixture of $87\,mg/L$ of Kiton Red 620 and $24\,mg/L$ of Rhodamine 640 in methanol. The laser average output power variation with output wavelength is presented in figure 2.1. Since the output is relatively flat between $605 \ldots 615\,nm$ (spectral region of interest), we need not worry about intensity variations with laser tuning in the results presented further.

2.1.2 Laser attenuation

In order to excite the crystal with variable laser intensities, two methods of beam attenuation are utilized. The first consists of using stackable neutral density filters, providing attenuations over many orders of magnitude. These filters are robust and can be used with any of the lasers. Their only downfall is that if set improperly, they may slightly deviate the laser beam from its previous path, leading to a realignment of all related optical components. The second method makes use of a computer-controlled multi-prism variable attenuator. This item varies intensities over approximately 2 orders of magnitude without altering the light path. Since it is computer-controlled through a step-motor, careful calibration of this instrument can lead to very accurate intensity dependent measurements. It is therefore setup in conjunction with the pulsed dye laser, the prominent experimental tool in our experiments. For simplicity, laser intensities will often be presented in terms of optical density (OD) attenuation. These can be converted to actual measures of intensity by this simple formula:

$$I = I_0 10^{-OD} \tag{2.3}$$

For instance, an OD of 0.3 corresponds to an attenuation factor of 2, and so on.

2.2 Exciton-Mediated Photovoltaic Effect

Detection of excitonic BEC in Cu_2O has been attempted through photoluminescence experiments [21, 24, 25, 26, 27]. Unfortunately, the orthoexciton lifetime ($\sim 1\,ns$) is shorter than the condensate formation time, making orthoexciton photoluminescence difficult in BEC studies. The paraexcitons on the other hand, have a relatively long lifetime, giving them ample time to form a condensate. Yet, they have a very low radiative efficiency, once again dismissing photoluminescence as a suitable detection technique. One must then resort to other methods to detect the travelling condensate. In this project, we call on a technique developed by solar cell researchers termed the exciton mediated photovoltaic effect [28].

The detector consists of two contacts: one is an ohmic semitransparent gold contact, which permits adequate currents with only small voltages, and the other is a rectifying copper contact. At the interface of the latter, the Fermi levels line up and lead to a bending of the energy bands. Figure 2.2 offers a schematic of this effect. The potential barrier (Φ_B) at the interface is of the order of $1\,V$ [29, 30], which results in a high electric

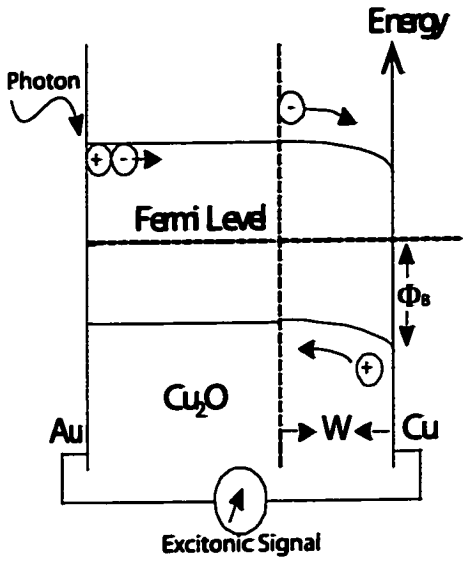

Figure 2.2: Schematic of the exciton-mediated photovoltaic effect.

field region of depth W ranging around $10 \ldots 100\,nm$ in Cu_2O [31]. The static electric field created is of the order of $\Phi_B/W \approx 10^5 - 10^6\,V/cm$, which corresponds nicely to the required exciton dissociation field $\approx 10^6\,V/cm$. This means that a fraction of the excitons will dissociate and produce a measurable current.

Unfortunately, the setup as shown in figure 2.2 may only be utilized with low intensity lasers as higher intensities would damage the gold electrode (set on the front excitation surface). Secondly, the high series impedance of the crystal at low temperatures ($\sim 1\,M\Omega$) would result in high time constants for the detected signal which is not acceptable in our experiments, requiring nanosecond resolution. This was corrected by depositing the gold electrode on the back surface with the copper electrode. Many configurations were studied [6] and the one illustrated in figure 2.3 offered the best signals. The present detector consists of a Au ring surrounding a Cu spot ($r = 1\,mm$). The effective detector volume generated by the Cu/Cu_2O barrier is then $\approx \pi r^2 W$, where r is the Cu spot radius and W is the high electric field region depth. This implies that only the excitons which travel across the crystal to the detector will induce a current. Clearly, if parasitic light travels around the crystal and hits the detector face directly, it will also create a signal. A sturdy sample holder (section 2.3.6) is therefore required to isolate the desired signal.

The present exciton detector configuration (figure 2.3) was carefully studied in [6] by direct $532\,nm$ pulse illumination. Detection was found to be linear over a large range of laser intensities spanning many orders of magnitude. For direct illumination, the

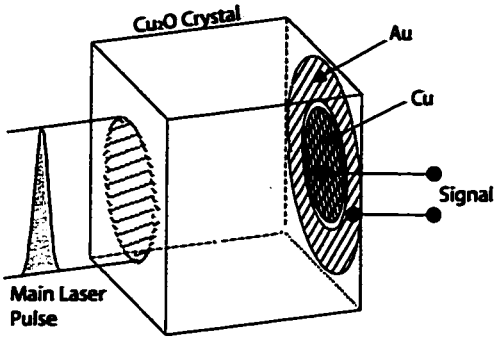

Figure 2.3: Electrode configuration for high intensity time-resolved photovoltaic detection.

efficiency was recorded at $\sim 1\%$; it fell to $\sim 0.1\%$ for the back cell geometry utilized in most experiments (figure 2.3). These results are similar to those obtained by solar cell researchers [33]. The time resolved signal $S(t)$ in mV can then be given as a function of the exciton density near the electrodes $n(t)$, the velocity of the excitons v, the detector area A and the detector efficiency η (in units of $\frac{mV}{exciton/sec}$), by:

$$S(t) = \eta n(t) v A \tag{2.4}$$

2.3 Sample Preparation

This section presents the complete, step by step instructions for preparing our samples. It starts off with a quick presentation of the samples themselves, followed by polishing, etching, and mounting procedures.

2.3.1 Sample orientations

As briefly presented in section 1.2.3, a cuprous oxide monocrystal can exhibit optical polarization-dependent absorption at the 1S orthoexciton resonance along some of its crystalline axes. Proper selection of crystal orientations can therefore be important, not only to maximize the oscillator strength, namely the absorption, but also to provide the possible experimental advantage of varying absorption with polarization. Inherently, this feature can be used as a tool to vary cold exciton populations in the crystal (see section 2.4) as light polarization is rotated with regards to the probed sample. One can then study how related signals vary with this new parameter, helping to shed some light

$\vec{q}$	$\vec{\varepsilon}_{\phi=0}$	$Z(\phi)$
[001]	-	0
[111]	-	1/3
$[1\bar{1}0]$	[111]	$\sin^2(\phi + 35.26^1)$
$[11\bar{2}]$	[111]	$\frac{1}{3}(\sin^2(\phi) + 1)$

Table 2.1: Polarization-dependent absorption in Cu_2O for various crystal orientations.

on the processes involved in our experiments.

This project deals with two high-quality natural grown Cu_2O crystals in particular. The first measures $6.4 \times 4.9 \times 4.7 mm$ and is oriented along the $[111] \times [1\bar{1}0] \times [11\bar{2}]$ crystal axes respectively. The faces are clean and undamaged, ideal for polarization dependent experiments which require a precise determination of the crystalline plane of excitation. This crystal will hereafter be referred to as sample (F), named after its owner, professor D. Fröhlich from Universität Dortmund in Dortmund, Germany, who loaned it to us for the purpose of these experiments. The second crystal (sample (1)) measures $1.94 \times 3.69 \times 3.56 mm$ and is purportedly oriented along the $[001] \times [1\bar{1}0] \times [110]$ crystal axes respectively. Although the (001) faces are relatively clean and undamaged (largest surface), the other faces of this somewhat older sample present a series of minor cracks and dents. Since its orientation has not been verified for quite a while now (crystal faces may be somewhat slanted by repeated polishing), polarization dependent experiments are not conducted on this sample.

Using equation 1.19, we can predict the polarization dependent absorption pattern for the various crystal faces of our samples. In table 2.1, these results are presented, where $\vec{q}$ and $\vec{\varepsilon}_{\phi=0}$ are the incident light wavevector and polarization vector (for relative polarization angle $\phi = 0$) in the crystal frame of reference respectively, and where $Z(\phi)$ is a function directly proportional to optical absorption in the crystal. Notice that the [111] axis of sample (F) presents no polarization dependent absorption; polarization dependent experiments are then conducted along the other two directions, $[1\bar{1}0]$ and $[11\bar{2}]$. In both cases, the [111] axis is kept as a reference ($\phi = 0$) for measures of the relative polarization angle. Also note that in certain results of chapters 3 and 4, the function $1 - Z(\phi)$ is reported instead of $Z(\phi)$, since actual measurements made are of transmitted intensities, and not directly of absorption.

[1] $35.26 = cos^{-1}(\frac{2}{\sqrt{6}})$, the angle between the crystal [111] and [110] axes. A beam incident along the $[1\bar{1}0]$ crystal axis and polarized along the [110] crystal axis will not be absorbed.

1	▷ 10 μm Al_2O_3 powder on glass sheet with distilled water for $\sim 1\,min$, longer if epoxy and/or electrodes persist. ▷ Rinse with distilled water/methanol solution in ultrasonic cleaner. ▷ Wipe dry with tissue paper. *N.B: This step removes the greatest quantity of material. Since crystals are small, one should stop once previous electrodes/epoxy are removed.*
2	▷ 1 μm diamond paste on Microcloth with polishing fluid for $\sim 15\,min$. ▷ Rinse with distilled water/methanol solution in ultrasonic cleaner. ▷ Carefully touch dry with optical tissue paper.
3	▷ $< 1\,\mu m$ diamond powder on Microcloth with no lubricant for $\sim 1\,min$. ▷ Rinse with distilled water/methanol solution in ultrasonic cleaner. ▷ Carefully touch dry with optical tissue paper.

Table 2.2: Guidelines for sample polishing.

2.3.2 Polishing

The samples require polishing to remove unwanted scratches and dents from the crystal faces. These marks, amplified by the chemical etching process, provide local exciton disassociation points that reduce the efficiency of the exciton detector, and dampen the creation of high exciton surface densities required for BEC experiments. In addition, previous broken or damaged electrodes and leftover contact epoxy must be removed before depositing new ones. Table 2.2 presents the basic guidelines to sample polishing. Evidently, results and polishing times will vary with operator skill and experience.

All the polishing is done by hand with no particular type of holder. The sample is held between two fingers, or again at the tip of one finger when the crystal dimensions impose it, and is carefully moved in a circular motion over the polishing elements. Steps 2 and 3 can be done with the help of a turntable which accelerates the polishing process, but increases the procedure's level of difficulty (the small samples are sometimes hard to keep steady on the moving disk). In any case, one should try to vary the direction of the polishing motion to avoid the creation of bevel faces induced by nonuniform pressure. A microscope can be used to determine when to change powders. If a certain powder size has no more effect, it is time to change it. The finished product should give off a nice shine, with only minor microscopic imperfections.

1	▷ Rinse crystal in distilled water.
2	▷ Soak for $1\,min$ in methanol with final $20\,sec$ in ultrasonic cleaner.
3	▷ Etch for $3\,min$ in HBF_4 ($\sim 5\,\mu m/min$), then dilute quickly with distilled water.
4	▷ Repeat steps 1 and 2.
5	▷ Soak for $90\,sec$ in Bromine(2% vol.)/Methanol solution with final $30\,sec$ in ultrasonic cleaner.
6	▷ Repeat steps 2 and 5.
7	▷ Repeat steps 2 and 1. ▷ Quickly blow dry with He or N_2 to eliminate water spots.

Table 2.3: Guidelines for chemical etching.

2.3.3 Chemical Etching

Once the polishing is done, a chemical etch is performed to remove the top atomic layers of the crystal faces which may have been damaged during the polishing. This process can also be used instead of polishing to remove previous electrodes, but only if the crystal faces are still in good condition (etching amplifies marks and scratches). The etching process described in table 2.3 was developed by solar cell researchers and has been found to lower the surface recombination rate and maximize the barrier field at the Cu/Cu_2O interface [32]. It must be mentioned that this method was developed and verified for a crystal's (100) face and may not be as optimized for the other faces presented by our samples; since the crystals are cut to present three different faces, and since we can not adequately etch only one face at a time, we adopt this etching method as being satisfactory for all faces. Once the etch is done, the crystal dimensions, important for condensate velocity calculations and sample holder designs, are carefully remeasured to see how much material was lost in the polishing and etching procedures.

2.3.4 Electrode Depositions

To detect excitonic condensates and other excitonic signals, we make use of the exciton mediated photovoltaic effect, as discussed in section 2.2. The exciton detector consists of a Au ring electrode and a Cu circular spot electrode in its center. These electrodes are deposited via three successive vacuum evaporations (thickness $\sim 80-100\,nm$) using carefully crafted masks. Since the Cu/Cu_2O interface may chemically oxidize when exposed

1	▷ Put sample in sample holder. ▷ Secure with teflon tape without blocking excitation holes.
2	▷ Solder short gold wires to sample holder connectors.
3	▷ Form a small foot at the end of wires ▷ Position the wires on the electrodes.
5	▷ Use a small wire hook to drop epoxy at the foot of the wires
6	▷ Let cure for 3-4 days

Table 2.4: Guidelines for wire contacts.

to heat to form an undesired layer of CuO which reduces the detector efficiency, the gold ring is evaporated first. This is done in two steps with the same mask, which consists of a three segment ring, that is flipped and rotated 180° for the second evaporation. The Cu spot is then evaporated last.

The masks are fixed to the sample holder through four corner pegs. One must center the sample with the masks carefully to ensure quality electrodes. Since the electrodes cover most the the crystal surface, it is not unlikely that some evaporate will be deposited on one of the sample sides if the crystal is misaligned. The sample itself is held in place by four teflon screws also used to properly align the crystal. If the evaporations are done right, the Au ring and Cu spot will exhibit a constant $250\,\mu m$ separation.

2.3.5 Wire Contacts

Once electrodes are deposited, wire contacts may be affixed. This is by far the most delicate procedure in the sample's preparation; a steady hand and a very relaxed environment are therefore critical assets when affixing the contacts. $50\,\mu m$ diameter gold wires are used to collect the signal; 2-3 wires are used on the gold electrode, which does not adhere very solidly to the crystal face, whereas one wire is often sufficient for the copper electrode. Since heating the sample would drastically reduce the detector efficiency, we must use an epoxy that will cure at room temperature. Evidently, this epoxy must also withstand multiple trips from room temperature (RT) to 2K and back again. Epo-Tek 410E (later modified to Epo-Tek 4110E), a two-part silver epoxy, is found to survive the harsh thermal cycles and cures at RT over a period of 3-4 days. Guidelines for contact fixation are presented in table 2.4.

Usually, when a mistake is made with the epoxy, the whole sample preparation process must be restarted. Sometimes, corrections can be made by light rubbing of the contacts

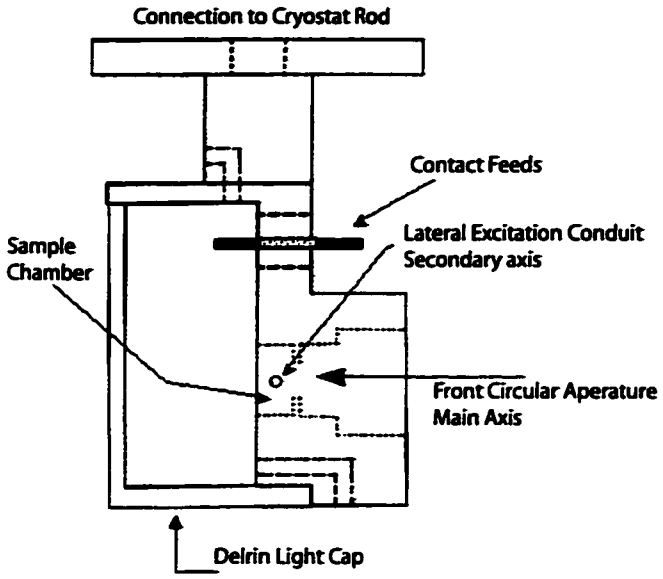

Figure 2.4: Sample holder schematic, as developed in [14].

with a cotton swab, but this will most likely remove some of the gold electrode as well. The epoxy must stay on the electrodes. Any contact created with the epoxy between the electrodes and the holder, the sample and the electrodes, or between the two electrodes themselves will either drastically reduce the detector functionality, or disable it completely.

2.3.6 Sample Holder

A sturdy sample holder (figure 2.4) is required to hold our samples immersed in superfluid helium while conducting our experiments. It must support the crystal and provide adequate optical access for stimulation, while keeping the detecting electrodes protected from intrusive parasitic light signals. The front face of the copper holder offers a $2\,mm$ (sample(1)) or $4\,mm$ (sample (F)) diameter circular aperture for YAG stimulation (initial condensate creation), and the side face offers a $0.5-1.0\,mm$ diameter circular conduit for secondary lateral stimulation at half crystal depth. Directly across from this side aperture, another hole is drilled to permit the insertion of a detecting optical fiber, which collects transmitted signals and feeds them to a detector situated outside the optical cryostat (see section 2.4.1). Finally, two posts, linked to a coaxial cable, permit excitonic signal transfers from the exciton detector (section 2.2) to the exterior data acquisition

equipment(see section 2.4.2). The holder is complete with a temperature sensor and a Delrin light cap.

Once the sample holder is constructed, a series of preparations are required before the sample can be mounted and dropped into the cryostat. A list of these procedures follows.

Ultrasonic Cleaning: Since the sample holder comes straight out of the machine shop, it has to be properly cleaned in order to avoid the crystal coming in contact with oils, greases and other harmful substances. To do this, the holder is immersed in methanol which is then put in an ultrasonic cleaner for approximately 5 minutes. This successfully cleans all sample holder surfaces.

Corona Dope: To reduce chances of short circuits in our setup, two coats of a basic black corona dope are applied to the sample holder. This also reduces reflections from the holder's shiny copper faces.

RTV Silicone: In order to get the wires to pass though the sample holder without creating any short circuits, vacuum feedthroughs are inserted in its base. These being partially translucent, parasitic light could then penetrate the light cap and falsify results. A thin layer of black RTV silicone is then applied to these areas to avoid such light to pass through.

Mounting: The sample holder is then mounted to the cryostat rod. The sample can then be carefully dropped into place and secured with small pieces of teflon tape. The light cap is then affixed and secured once again with teflon tape. The sample is ready.

2.4 Experimental Setup

2.4.1 Optical Cryostat

All of the experiments discussed in chapters 3 and 4 were performed in superfluid helium at temperatures $\sim 1.9 - 2.1\,K$. Since temperature variations in this range are small and have little, or no effect on presented results, a constant temperature of $\sim 2\,K$ is assumed.

In order to maintain such a low temperature while providing optical access to the sample, an optical cryostat (Janis Research model 8CNDT) with four window ports is used (each window consists of a pair of vacuum spaced fused quartz plates). In addition,

the cryostat is equipped with active cooling/heating mechanisms. These were used in previous experiments to conduct temperature dependent measurements. In the experiments discussed for this thesis, a constant temperature below helium's lambda point ($T = 2.17\,K$) was required, and hence no heating was necessary. Yet, to compensate for laser heating effects, additional cooling was occasionally needed.

Active cooling was achieved by pumping on the liquid He in the optical chamber, evacuating the cold gas out of the cryostat through the sample's access tube. The sample is attached at the bottom of a $1\,m$ Invar rod which is itself attached at its top to the cryostat with a vacuum tight seal cap; the cap provides electrical and optical access to the sample, permitting the passage of optical fibers utilized for light transmission measurements and electrical wires utilized to control the heaters (not used) and to carry the excitonic signal from the crystal to exterior equipment. By varying the pumping rate using an accurate computer-controlled valve, we can successfully control the temperature. By keeping the pumping rate at a constant maximum, and by varying the input of liquid He into the optical chamber (controlled by a needle valve), steady superfluid He temperatures were adequately maintained.

The sample chamber's temperature was carefully monitored by two sensors, one mounted on the optical chamber floor, and the other mounted directly at the end of the sample holding rod. Both sensors consist of silicon diodes with temperature calibrated resistances. The external controller (LakeShore Cryotronics DRC 80C) measures the temperature dependent resistance by sending short electrical pulses; the sample temperature is then displayed and recorded with every data acquisition.

2.4.2 Data Acquisition

Time resolved measurements are acquired with a digitizing oscilloscope (Tektronics model 620b) featuring two $500\,MHz$ channels operating at a maximum sampling rate of 2 $G\,Sample/s$. Two additional auxiliary channels ($500\,M\,Sample/s$) are also available (mainly used for triggering purposes). All channels are operated here at a $50\,\Omega$ impedance, providing time-resolved current measurements. Trace averaging is also performed through the oscilloscope, providing noise reduced measurements, indispensable to these experiments (background noise signals can be as large as the excitonic signals themselves). After adequate averaging (75 to 100 pulses), the data is transferred and stored on a computer through a GPIB interface with the oscilloscope.

The raw data can be further processed to facilitate analysis. The computer program

(TEK[1]) written and optimized by Eric Benson performs all of the required operations. An averaged background trace is first subtracted from the data; this removes all persistent equipment-induced noises form the signal that could not be removed through averaging. The trace can then be submitted to a Savitzky-Golay smoothing algorithm. Although this step can help to clarify certain aspects of the data, it also brings forth alterations to the raw data which can be misleading. For example, sharp peaks are rounded and broadened, and sometimes even smoothed out by the filter; this must be considered when studying a trace's fine structures. Results in Chapters 3 and 4 were only rarely passed through the smoothing algorithm when fine structure was not of interest, leading to (according to the author) truer results.

Once the processing is done, the data is converted to ASCII format and transferred to spreadsheet accessible files. If requested, additional measurements can be performed by TEK and printed to file. Such measurements include pulse amplitude, arrival time, pulse full width at half maximum (FWHM), as well as total integrated and baseline signals. For the majority, data was then treated with the Microcal Origin 6.0 software, providing graphs and traces presented in this thesis.

2.4.3 Optical Fibres, Connectors and Detectors

Optical fibres play an important role in our BEC experiments. Their main purpose is to gather transmitted lateral excitation signals, and to direct them to optical detectors outside the cryostat. Such measurements will then lead to transmission and normalized differential attenuation (NDA) analyses discussed further in chapters 3 and 4. Their other purpose is to provide a means to direct the secondary excitation, from the laser output to the crystal, using various path lengths. Both the detecting and exciting fibres are positioned halfway along the crystal side faces, directly across from one another, forming the secondary axis depicted in figure 2.9 (see figure 2.10 for complete experimental setup).

The exciting fibre is important to generate accurate time delays between the arrival of the initial condensate-creating laser pulse (YAG laser) and the secondary excitation. Through these variable delays (generated by various fibre lengths), one can spatially probe the travelling exciton packet at various points within its comet-like construction.

[1]The program TEK also controls two stepper motors (multi-prism variable attenuator and cryostat optical chamber pumping valve), calibrates the attenuator, transfers raw data form the oscilloscope to file, controls a spectrometer (used sparingly in this research project), records spectra from a lock-in amplifier and offers various graphical interfaces for data display and manipulation.

For example, phenomena such as condensate amplification (section 4.1) and NDA (section 4.2) were shown to vary considerably with pump-probe synchronization [13, 14]. If the secondary pulse hits the crystal when the condensate is still near the front crystal face, it experiences no NDA and amplification is at a minimum. However, when both the secondary pulse and the condensate are synchronized to meet near the centre of the crystal, NDA and amplification reach their maxima. Such observations are crucial in determining the factors that govern and influence amplification. We can then setup our experiments to maximize the observation of desired phenomena, such as the amplification and the NDA mentioned above, to yield better results for analysis. In most experiments discussed in this thesis, 1/2 transit delays (1 transit delay equals the time it takes for the condensate to travel from one end of the crystal to the other) will be utilized unless otherwise specified. This means that in most cases, we deal with maximal amplifications and normalized differential attenuations.

For both secondary excitation and transmitted secondary pulse detection, $200\,\mu m$ multi-mode fused silica fibres are used. The detecting fiber is brought out of the cryostat and connected to an optical detector (New Focus, model 1621) which directs its signals to the digitizing oscilloscope. Traces are then analyzed following the procedure described in the above section (2.4.2). As for the exciting fiber, it receives the focused pulsed dye laser at one end, and delivers it near the lateral excitation window. As discussed above, various fibre lengths can be utilized to vary the lateral pulse delay with regards to the main excitation pulse; if no fiber suits the desired delay, two or more shorter fibres may be connected together using special index-matching gel connectors; this is done at the expense of a modest $5 - 10\%$ laser intensity loss per connector. Once the pulse exits the fibre near the cryostat window, it is collimated and directed to the sample holder through which the sample can be illuminated. In many experiments, secondary pulse light polarization is of importance. In these cases, since we do not use polarization-conserving single mode fibers, the secondary pulses must also be polarized using a single polaroid polarizer (used in conjunction with an appropriate $\lambda/2$ plate for linear polarization direction control) before they are directed to the sample (discussed in section 2.5.1).

Before we incorporated optical fibres into our experimental setups, we had to verify that they did not bring forth any undesired changes to the pulses that travelled within them. It was then important to verify the change in pulse bandwidth and duration when a fibre was used. Tests compared the pulses when no fibre was used, to pulses having travelled through $160\,m$ of fibre.

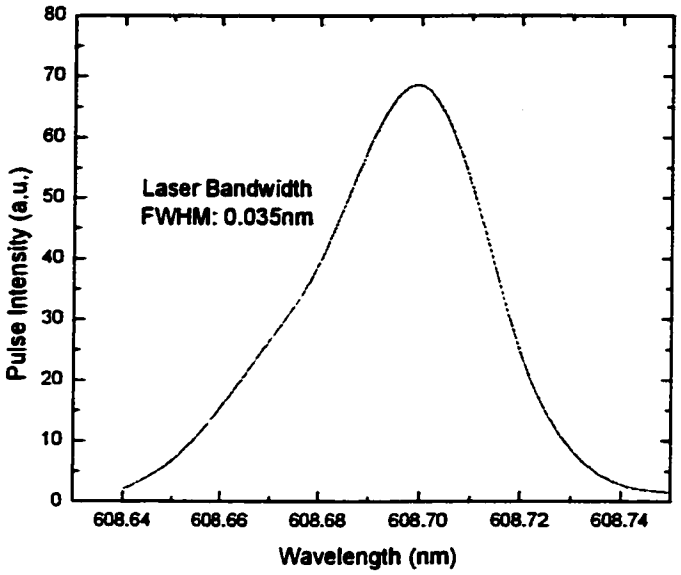

Figure 2.5: Pulsed dye laser bandwidth.

In figure 2.5, the dye laser bandwidth is measured at $\sim 0.35\,\text{Å}$which corresponds to approximately $110\,\mu eV$. When the pulse travels through the fibre, it experiences a mild spectral compression, reducing the bandwidth to $\sim 0.20\,\text{Å}$, corresponding to approximately $65\,\mu eV$ (figure 2.6). In both cases, the pulse bandwidth is of the same order of magnitude, and noticeably larger than the 1S orthoexciton transition line of interest (reported at $\sim 1\,\mu eV$ by experimental extrapolation [17]). This thus means that the spectral resolution obtainable with this laser is too low for direct characterization of the absorption line itself, but high enough, both with and without the fibre, to study condensate amplification and related signals with secondary pulse wavelength.

In figure 2.7, the dye laser pulse duration is determined to be $\sim 9\,ns$. When compared to the pulse duration after it has travelled through the fibre, it is found to be slightly increased to $\sim 12\,ns$ (figure 2.8). Again, this does not pose a serious problem, as both pulse durations are relatively quick on the timescale of our experiments, which range from $\sim 0.5 \ldots 3.0\,\mu s$. We are then not concerned about this slight temporal expansion.

From the above results, it is clear that the use of fibres to excite our samples brings no serious changes to the experiments. For simplicity, since we practically always use a fibre (of length between $50\,m$ and $600\,m$) to stimulate our samples, we will assume a pulse duration of $12\,ns$ and a pulse bandwidth of $\sim 70\,\mu eV$. This is not particularly accurate, but amply sufficient for our purposes.

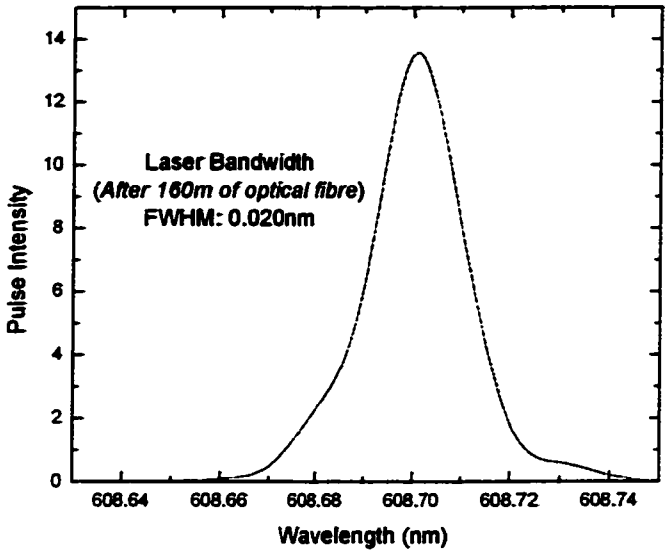

Figure 2.6: Pulsed dye laser bandwidth once it has travelled through approximately 160m of multimode optical fibre.

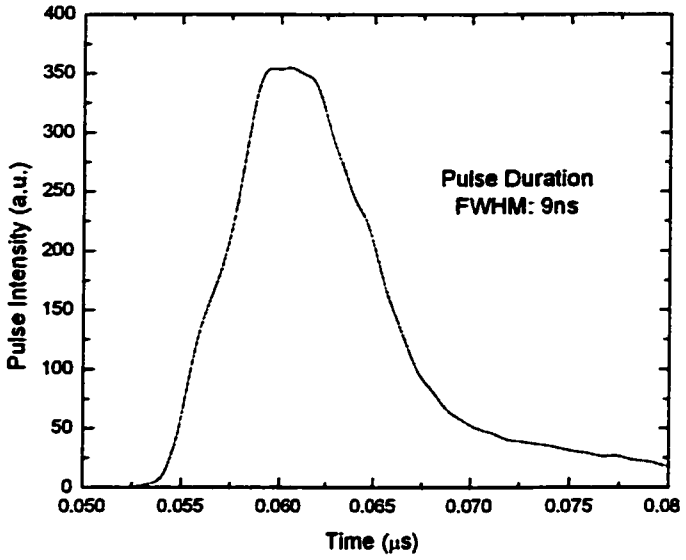

Figure 2.7: Dye laser pulse duration.

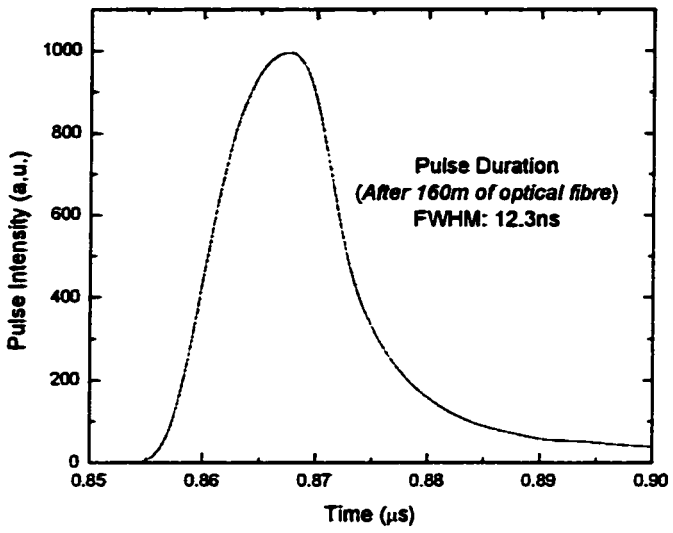

Figure 2.8: Dye laser pulse duration once it has travelled through approximately 160m of multimode optical fibre.

2.4.4 Single Pulsed Laser Excitation

In order to characterize the effects of a secondary pulse excitation on a travelling exciton condensate, it is important to analyze how this stimulus interacts with the crystal itself. Unlike previous single laser experiments (as reported in [6, 14]), where interests were geared at understanding the various parameters that governed the initial condensate creation with Nd:YAG laser pulses, single laser experiments conducted for this thesis study the weakly absorbed lateral pulse excitation of the crystal in the absence of a condensate (chapter 3); the crystal is illuminated as in figure 2.9 without excitation along the primary axis. These experiments provide details on sample absorption properties such as resonant polarization-dependent absorption along certain crystal axes (discussed in sections 1.2.3 and 2.3.1 and studied in section 3.1) and general absorption profiles around the orthoexciton resonance and the exciton band edge. They also provide information on light scattering within the crystal. The front signals, (discussed in section 3.2) are generated by the part of the lateral light pulses that scatters within the crystal towards the exciton detector. These signals provide information on secondary laser induced cold exciton populations within the crystal, which can be important when discussing condensate amplification (see section 4.1).

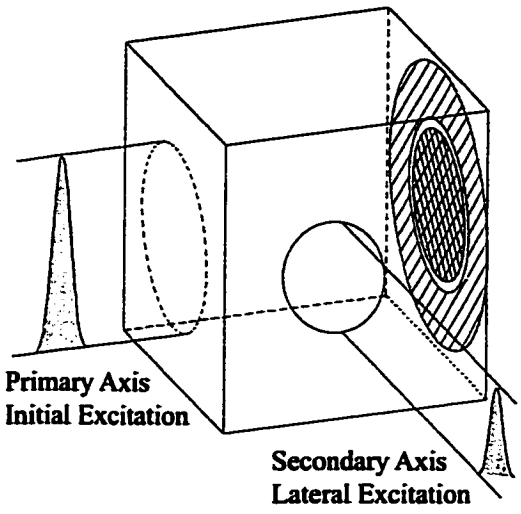

Figure 2.9: Lateral excitation of the sample depicting primary and secondary axes.

2.4.5 Orthogonal Double Pulsed Laser Excitation

This setup is used for the majority of experiments conducted for this project. It consists of using both the YAG laser for initial condensate creation, and the pulsed dye laser for time-delayed condensate probing. The orthogonal excitation of the sample is depicted in figure 2.9, where the YAG and lateral pulses are incident along the main and secondary axes respectively.

Figure 2.10 presents a complete schematic of the experimental setup used for double orthogonal pulse excitation. The YAG output is separated into two beams by a 50:50 beam splitter constructed to operate at $532\,nm$. One beam is directed to the front of the crystal to immediately create the initial exciton packet. The other beam is sent to the dye laser, where it generates pulsed radiation around the 1S orthoexciton resonance (see section 2.1.1). The generated pulses are passed through the computer-controlled multi-prism attenuator (and neutral density filters if needed), providing an accurately variable excitation intensity. They can then be focused into an optical fibre (of variable length) providing various time-delays with regards to the initial YAG pulse. At the fiber exit, the beam is collimated and shone through the sample holder's secondary excitation aperture. When polarization is of interest, the beam must first be polarized by a linear polarizer and passed through an appropriate $\lambda/2$ plate, used to vary the polarization angle as needed. The transmitted signal can then be collected via an optical fiber situated directly across the crystal from the excitation spot (see section 2.4.3).

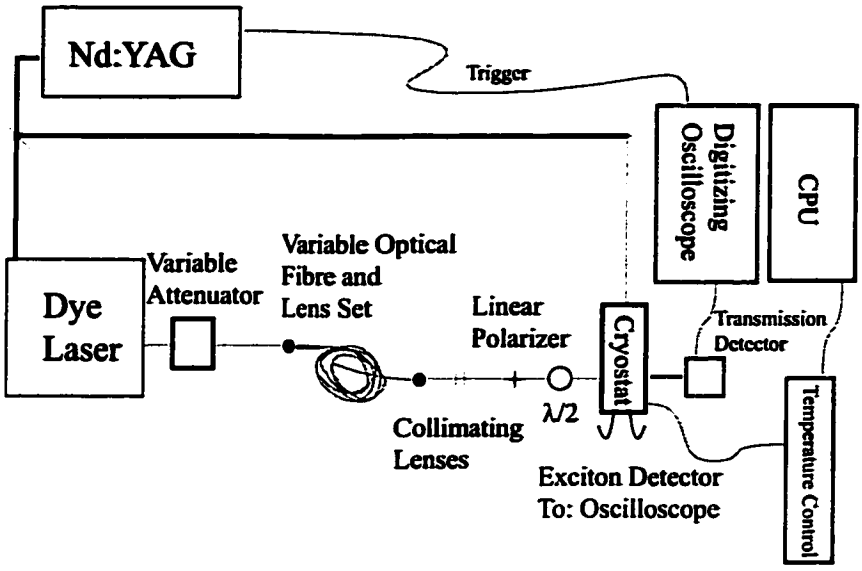

Figure 2.10: Most commonly used experimental setup: orthogonal double pulse excitation.

2.5 Preliminary Tests

2.5.1 Light Polarization Precision and Conservation

In order to properly study the polarization effects on our crystal, it is necessary to know the limits in precision that our equipment provides. Although we possess the manufacturers' specifications for every component, it is important to verify these numbers so as not to overestimate/underestimate the quality of our equipment.

Equipment important to polarization-dependent experiments include the pulsed dye laser (section 2.1.1), two Polaroid linear polarizers, and a half-wave plate. The latter was constructed for use at $632\,nm$; we thus verify its efficiency at $609.51\,nm$, the wavelength at which polarization becomes important in our samples. To first test the quality of the two polarizers, which will then be used to test the laser and the half-wave plate, a He-Ne laser of known polarization precision is used; the polarization of this laser is good to 500 : 1 (a vertically polarized beam will transmit up to a maximum of 0.2% of its measurable intensity through a horizontal polarizer). A complete look at these procedures is given in the next subsections.

Polaroid polarizers and $\lambda/2$ plate at $632\,nm$: Before any polarization tests can be conducted on the dye laser, the quality of our polarizers must first be known. As

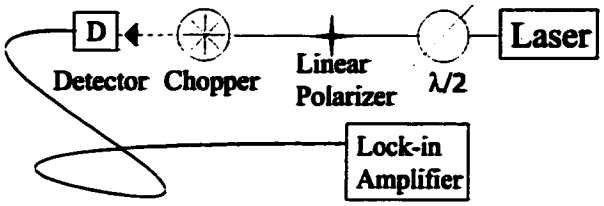

Figure 2.11: General setup for polarization precision and conservation tests.

mentioned above, we use a He-Ne laser polarized at 500 : 1 as our absolute value to which the quality of the polarizers will be compared. We will also use this laser to determine the quality of our half-wave plate, in other words, to determine how well polarization is conserved as light is transmitted through it. The simple setup required to conduct these first two preliminary tests is represented in figure 2.11.

In the first test, we simply rotate the polarizer and record the variation in transmitted intensity with an optical detector connected to a lock-in amplifier. We then take the ratio of the maximum transmission to the minimum transmission to determine the polarizer's quality. As for the half-wave plate, we keep the polarizer in a fixed position and turn the $\lambda/2$, hence turning the light's polarization and recording similar variations in transmitted intensity. The polarizers are evaluated at 500 : 1, which indicates that they are at least as precise as the He-Ne laser. The half-wave plate brings no variation to these results, indicating that the laser's polarization is not affected as it is transmitted through it. Nonetheless, we will have to retest the latter with the other laser as this property could change as a function of wavelength.

Pulsed dye laser and $\lambda/2$ plate at 609.51 nm: For this laser, the procedure is similar to the above, but the measuring equipment is different. Since we deal with a pulsed emission, we can not use the lock-in amplifier and must resort to a triggered oscilloscope to measure transmitted intensities. Using the same methods as above, we find a ratio of approximately 50 : 1 for the pulsed laser alone (higher than predicted by the manufacturer: 20 : 1), and one of 40 : 1 when we include the half-wave plate. This thus indicates that the half-wave plate does influence polarization conservation at this wavelength. But, as discussed in the next few chapters, a 2.5% uncertainty on polarization is acceptable, still permitting the acquisition of conclusive results. We then conclude that our equipment is accurate enough to proceed with polarization-dependent experiments, keeping in mind that we are

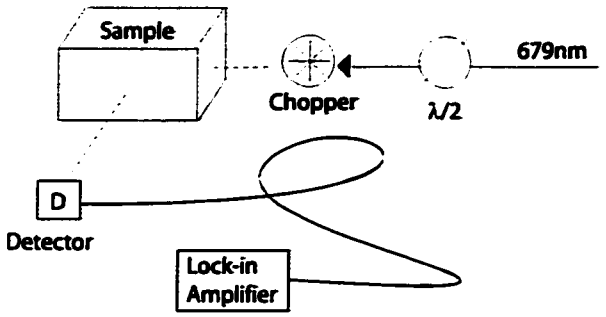

Figure 2.12: Equipment setup for Rayleigh scattering test.

$\vec{k}$	$\vec{k'}$	Rayleigh Effect
$[11\bar{2}]$	$[1\bar{1}0]$	7%
$[1\bar{1}0]$	$[11\bar{2}]$	8%
$[111]$	$[1\bar{1}0]$	3%
$[111]$	$[11\bar{2}]$	5%

Table 2.5: Extent of Rayleigh scattering in sample (F).

limited to an approximate polarization ratio of 40 : 1.

2.5.2 Light Scattering

In most experiments, polarization dependent variations in the various detected signals are used in the formulation of plausible models and conclusions for our system. The principal source of polarization dependent variations is believed to be the crystal's own resonant polarization-dependent absorption along some of its axes. Yet other sources, such as Rayleigh scattering, must be ruled out before proceeding with the analysis of these signals. Room temperature tests were thus conducted to measure the extent of Rayleigh scattering within the samples. A simple test configuration consisted of a polarized transmitting laser source (diode laser, $\lambda = 679\,nm$), a $\lambda/2$ plate, a chopper and an optical detector connected to a lock-in amplifier. The equipment was set up (figure 2.12) to measure the light scattered inside the crystal at a 90° angle from the exciting beam. Rayleigh scattering predicts that a beam with wavevector $\vec{k} \parallel \vec{x}$ and with a polarization vector $\vec{\epsilon} \parallel \vec{z}$ will be scattered into a beam $\vec{k'} \parallel \vec{y}$ of polarization $\vec{\epsilon} \parallel \vec{z}$. By detecting the variation of the scattered light intensity at 90° with incident polarization, we get an approximate measure of the extent of Rayleigh scattering within our sample. Table 2.5

gives the relative Rayleigh scattering effect for different crystal geometries; clearly, no more than $3-8\%$ of scattering is attributed to the polarization-dependent Rayleigh effect. This thus means that the other $90-95\%$ of observed scattering is induced by minor crystal imperfections in our samples of spatial dimensions greater than the probe wavelength; this scattering process is completely polarization-independent. As we will see in section 3.2, scattered light generated excitonic signals are significant in our experiments and will be considered to properly account for all excitons created within our samples.

Results

The next two chapters present results obtained in various experiments conducted on our samples. Chapter 3 presents results obtained through the lateral excitation of Cu_2O crystals by a pulsed laser beam tuned near the exciton resonance. In section 3.1, we look at the absorption properties of Cu_2O in the $600 - 615\,nm$ range, providing detailed information on the resonant polarization-dependent absorption available along certain crystal axes (discussed in sections 1.2.3 and 2.3.1). The following section (3.2) presents results related to the creation and detection of instantaneous and diffusive front signals; a front signal is generated by part of a light pulse, incident along the crystal's secondary axis, that is scattered along the crystal's main axis and detected by the excitonic detector situated at the back face of the crystal. The front signal variation with laser tuning and polarization is investigated, which will lead to a better understanding of the amplified condensate signals discussed in the next chapter.

In chapter 4, results are presented on interactions observed between a travelling condensate and the aforementioned secondary pulse excitations. In the first section, condensate amplification will be discussed in detail, observing the various parameters that influence the extent of the amplification; such parameters include secondary excitation wavelength, intensity and polarization, as well as the relative time delay separating the initial YAG pulse (which creates the travelling condensate) and the secondary pulse (which probes and amplifies the condensate). The next section then discusses other effects related to condensate-secondary pulse interactions measured through the differential attenuation of transmitted and scattered light. Throughout the chapter, efforts are aimed at determining how the secondary excitation interacts with the condensate, and how these interactions can be used to explain the observed condensate amplification.

Chapter 3

Light Absorption and Scattering Effects Near the 1S Orthoexciton Resonance and Band Edge

In order to properly understand the phenomena attributed to the secondary excitation of our samples, it is important to understand what actually happens to these lateral pulses once they enter the crystal. The present chapter aims to shed some light on this problem, presenting results related to the absorption and scattering of the lateral pulse in the spectral region of interest ($603 - 612\,nm$).

3.1 Optical Absorption

The optical absorption spectrum for Cu_2O ($T = 2\,K$) at wavelengths around $603-612\,nm$ presents three different regions of interest: resonant n=1 absorption, n=1 phonon-assisted absorption, and higher energy absorption into the band edge. In figure 3.1, the direct 1S orthoexciton absorption line, the first important region, is presented through transmission measurements as centered at $609.51\,nm$ ($2.034\,eV$) and of width of $\sim 60\,\mu eV$. These values compare to reported values of $2.033\,eV$ and $\sim 1\,\mu eV$ [17]. It is clear that our peak absorption value is only slightly shifted from the accepted value due to a dye laser calibration error. As for the measured line width, it is limited only by the dye laser bandwidth, estimated at $\sim 70\,\mu eV$ in section 2.4.3. Measurements at resonance are henceforth made and reported at a wavelength of $609.51\,nm$ while the spectral resolution of our data is limited by the laser bandwidth stated above.

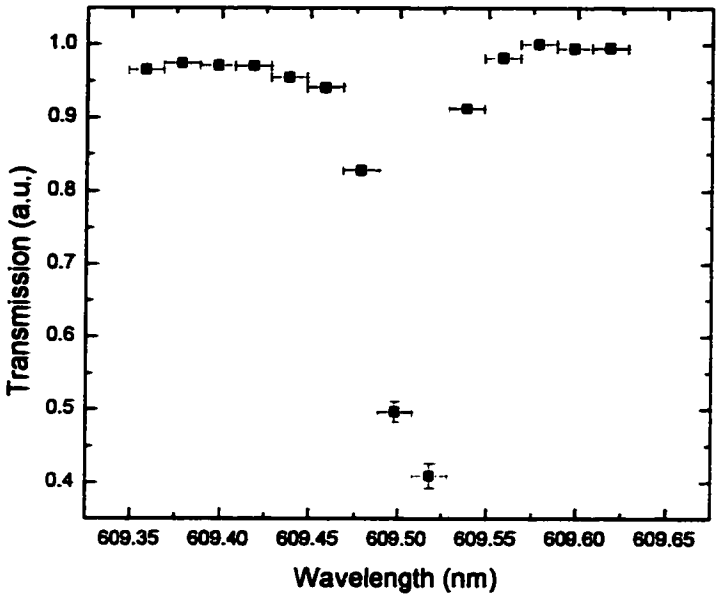

Figure 3.1: Resonant n=1 absorption around 609.51 nm. The spectral resolution is limited by the dye laser bandwidth.

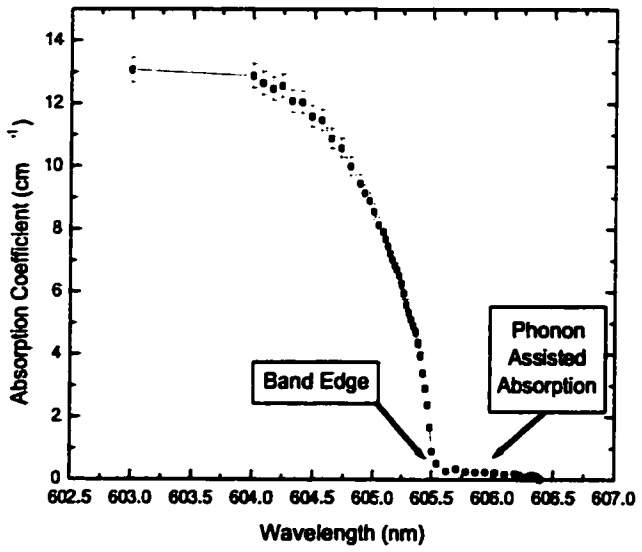

Figure 3.2: Absorption spectrum for Cu_2O around the band edge depicting phonon-assisted n=1 absorption and higher energy absorption into the band edge.

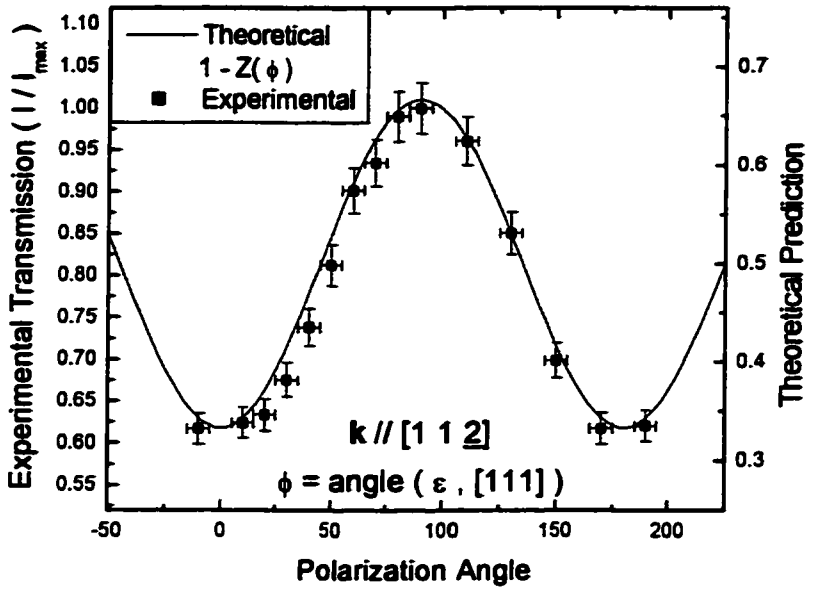

Figure 3.3: Resonant polarization-dependent absorption in Cu_2O for incident $\vec{k} \parallel [11\bar{2}]$.

The next two important features of the absorption spectrum are found at lower wavelengths around $605\,nm$. In figure 3.2, n=1 phonon-assisted absorption is first encountered at $\sim 606.4\,nm$. This type of absorption continues until the band edge is reached at $\sim 605.4\,nm$, after which absorption increases significantly. In our experiments, attention is brought to all three regions, separating results in three categories: measurements near resonance $(609.51 \pm 0.50)\,nm$, measurements near the band edge $(605 \pm 2)\,nm$, and off resonance measurements ($607\,nm - 609\,nm$, $610\,nm \ldots$). Special attention is brought to near resonance experiments, as the absorption profile is well defined, and polarization effects (section 3.1.1) may be exploited.

3.1.1 Resonant Polarization-Dependent Absorption

One of the parameters utilized to study the condensate amplification effects presented in the next chapter is the polarization of the secondary laser pulse. As presented in section 1.2.3 and further applied to our samples in section 2.3.1, absorption is polarization-dependent along certain axes in Cu_2O. In figures 3.3 and 3.4, absorption at resonance is plotted at various beam polarizations for two crystal orientations. In the first graph, the beam is incident along the crystal's $[11\bar{2}]$ axis. Taking the polarization vector $\vec{\varepsilon} \parallel [111]$ as the zero mark for the polarization angle ϕ, we look for the expected absorption function

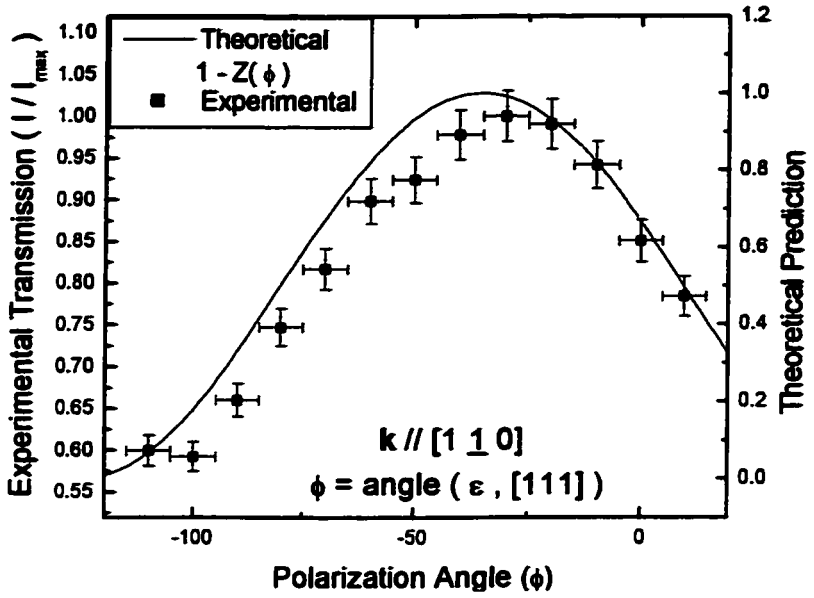

Figure 3.4: Resonant polarization-dependent absorption in Cu_2O for incident $\vec{k} \parallel [1\bar{1}0]$.

$Z(\phi) = \frac{1}{3}(\cos^2(\phi) + 1)$ for this crystal configuration (see table 2.1). In the second graph, the beam is incident along the crystal's $[1\bar{1}0]$ axis. With $\vec{\varepsilon} \parallel [111]$ again taken as the zero mark for the polarization angle ϕ, we now look for the expected absorption function $Z(\phi) = \sin^2(\phi + 35.26)$ for this second orientation (table 2.1). As we can see, absorption measurements in both cases[1] follow the predicted transmission variations given by $1 - Z(\phi)^2$. Notice that although experimental data is similar to theoretical predictions in quality, their are not identical in quantity, hence the individual scales. This is due to a variety of experimental parameters, such as the laser bandwidth, which is much larger than the absorption line itself, and the quality of the beam polarization once the light reaches the sample, which can be slightly altered by partial multiple reflections in the sample holder and crystal. Nonetheless, a clear polarization effect is measurable and can be utilized as an experimental tool for double pulse experiments (chapter 4). For simplicity, since two crystal orientations were utilized to conduct polarization measurements, the 0° polarization angle on following graphs will hereafter always be set at the appropriate minimum absorption angle.

[1]Small shift in data in fig 3.4 likely attributed to a simple systematic reading error.

[2]As mentioned in section 2.3.1, we can not measure absorption directly and must rely on transmitted light measurements to verify the polarization-dependent absorption rules of the 1S orthoexciton transition line. We thus assume that the function $1 - Z(\phi)$ adequately defines polarization-dependent transmission.

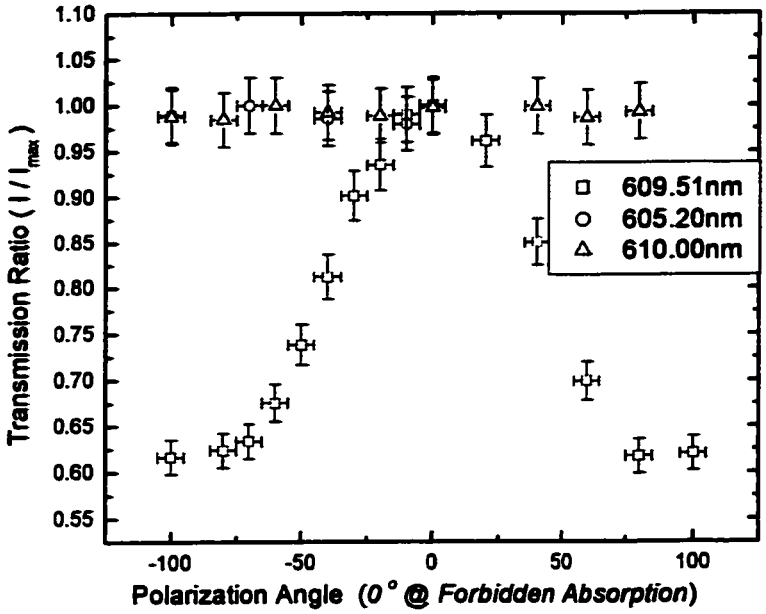

Figure 3.5: Polarization-dependent absorption is strictly a resonant effect.

In order to satisfy ourselves that variations in figures 3.3 and 3.4 are really a measure of the 1S orthoexciton polarization-dependent quadrupole absorption line, we observe transmission variations with beam polarization for different wavelengths. In figure 3.5, transmission ratios (defined as the transmitted intensity for a given polarization (I) divided by the maximum recorded transmitted intensity (I_{max})) are plotted for three exciting wavelengths: at resonance ($609.51\,nm$) where polarization-induced variations are detected, near the band edge ($605.20\,nm$) where absorption is expected to remain constant, and off-resonance ($610.00\,nm$) where no absorption is expected, and therefore, where no polarization-dependent variation in the transmitted intensity is expected either. With these three measurements, we can rule out certain alternative explanations for the polarization-dependent absorption observed at resonance in figures 3.3 and 3.4. For starters, if variations were related to the experimental setup and to equipment misalignment, they would be detected at all the above wavelengths, even off-resonance. Also, if they were related to another polarization-dependent absorption phenomenon not limited to the direct absorption line, variations would be detected near the band edge. In addition (not related to figure 3.5), one can also rule out Rayleigh scattering, which is a polarization-dependent effect, as it would not effect direct transmission, but only scattered light measurements made at 90° from the incident axis. The latter, which was introduced in section 2.5.2, will be further discussed in section 3.2.2 in conjunction

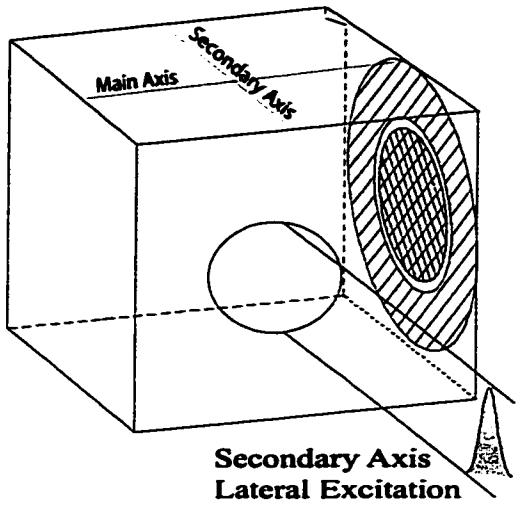

Figure 3.6: Front signals are generated by single lateral excitation along the secondary axis, where part of the light is then scattered within the crystal along the main axis.

with the measure of front signals, a byproduct of light scattering in the crystal. Having isolated the source of the observed polarization dependence in transmitted signals, we can now use polarization as a tool to study the effect of variational absorption along the secondary axis on various measurements, including front signals (section 3.2.2) and condensate amplification (section 4.1.3).

3.2 Front Signal

An important signal which has been ignored in past research is the lateral beam's front signal. This signal is generated by the part of the lateral light pulse that is scattered by minor sample imperfections within the crystal volume towards the exciton detector; this signal is **not** the exciton packet discussed later as a Bose-Einstein condensate. In figure 3.6, the excitation geometry for front signal analysis is depicted, showing clearly the lateral excitation along the secondary axis, which will then be partly scattered within the crystal along the main axis. In the next few sections, a complete look at this signal's variation with wavelength and polarization will be provided, helping to better understand the front's nature.

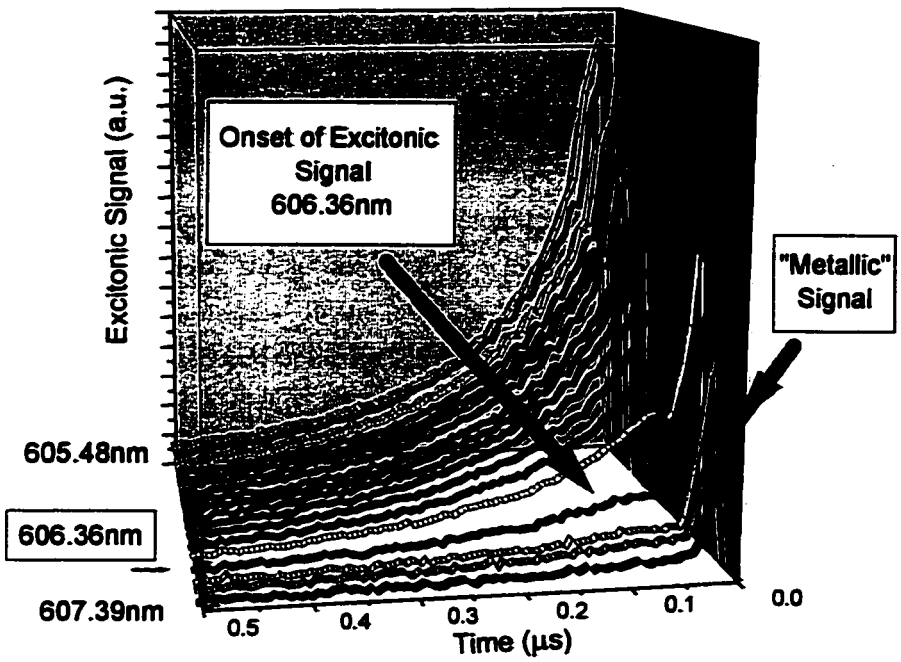

Figure 3.7: Front signal variation with lateral laser tuning around the Cu_2O band edge; the instantaneous and diffusive excitonic signals appear around 606.36 nm.

3.2.1 Front Signal Variation with Wavelength

A first attempt at understanding the front signal comes from its spectral analysis; we study the front over the $603 - 610\,nm$ range. In figure 3.7 the time-resolved front signal is plotted for a series of consecutive wavelengths from $605.48\,nm$ to $607.39\,nm$. From this perspective, we clearly observe the front signal's three components. At $607.39\,nm$, there is no absorption, both along the main and secondary axes. The only signal is generated by a direct excitation of electrons from the metallic electrodes across the potential barrier to the conduction band, producing a weak photocurrent. As the wavelength is decreased to approximately $606.36\,nm$, two excitonic signals start to emerge; the first is related to absorption of scattered light in the immediate vicinity of the electrodes, producing a weak, immediate excitonic signal, the second is related to excitons created through the absorption of the scattered light along the main axis. The same principle used to explain the propagation of an exciton packet (section 1.2.4) explains the increase in size and shape of this last diffusive signal. The more the light is absorbed, the greater the amount of excitons along the main axis, and hence, the larger the diffusive packet. At $606\,nm$, the three signals are combined and indistinguishable.

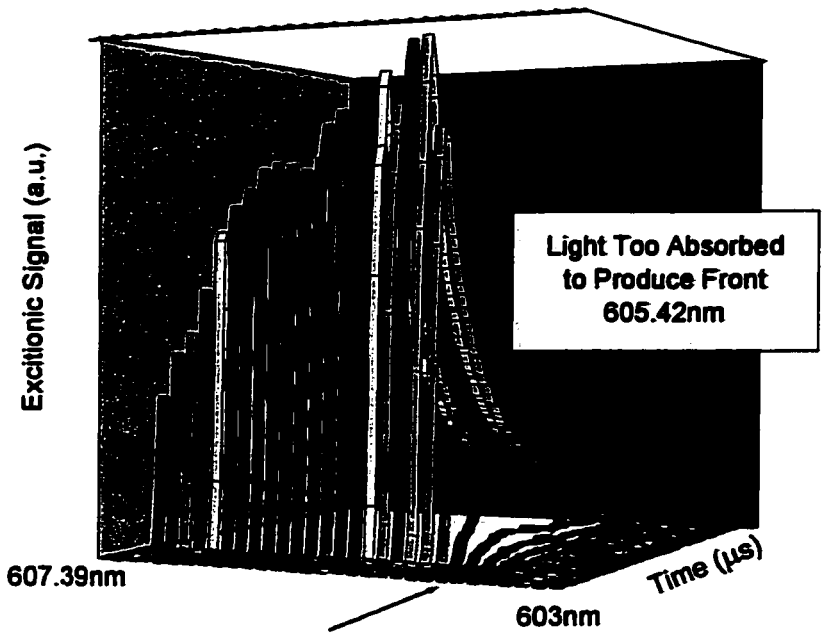

Figure 3.8: Front signal variation with lateral laser tuning around the Cu_2O band edge; both excitonic signals and the metallic signal vanish around $605.42\,nm$ due to increased optical absorption.

In figure 3.8, the same sequence of front signals is presented from another perspective, this time starting at $603\,nm$. For the first few wavelengths, no front signal is detected. This is due to the relatively high absorption factor at these wavelengths; light can not even reach the electrodes directly to produce the metallic signal observed in figure 3.7 (this also indicates that no parasitic light can reach the electrodes without first penetrating the crystal). As the wavelength is increased, light is less and less absorbed, which means that a diffusive exciton packet can be created by light scattering along the main axis and detected at the electrodes ($\sim 605.42\,nm$); again, neither a metallic nor an instantaneous excitonic signal is observed. Finally, as the wavelength is increased further, the three signals are finally observed.

Clearly, it is also important to look at the front signal as we approach the orthoexciton resonance. In figure 3.9, time-resolved front signals are presented in this spectral region, starting from completely off-resonance (608.39) to near resonance ($609.52\,nm$). As one notices, the same three signals observed near the band edge surface near resonance; first, a single metallic signal is detected off-resonance, followed by the weak apparition of both an instantaneous and a diffusive excitonic signal as resonance is approached,

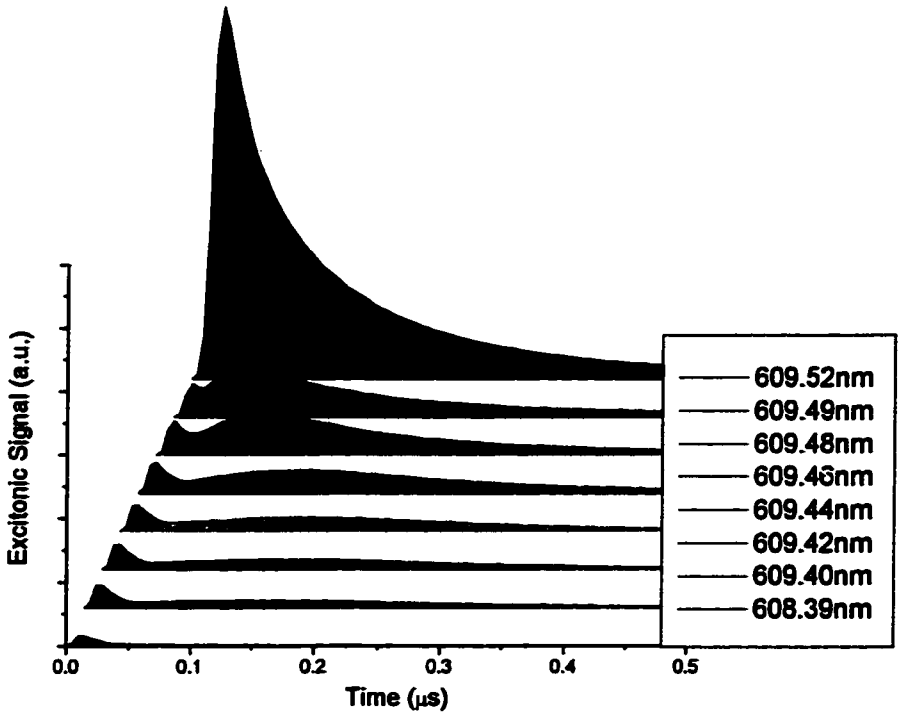

Figure 3.9: Variation of the front signal shape near resonance; the three front signal constituents are observed as they were near the band edge.

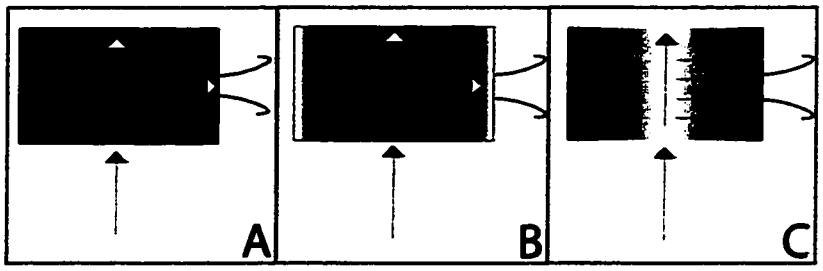

Figure 3.10: Front signal construction: A) Instantaneous metallic signal, B) Instantaneous excitonic signal, C) Diffusive excitonic signal *The exciton detector is represented by the curved lines on the back crystal face.*

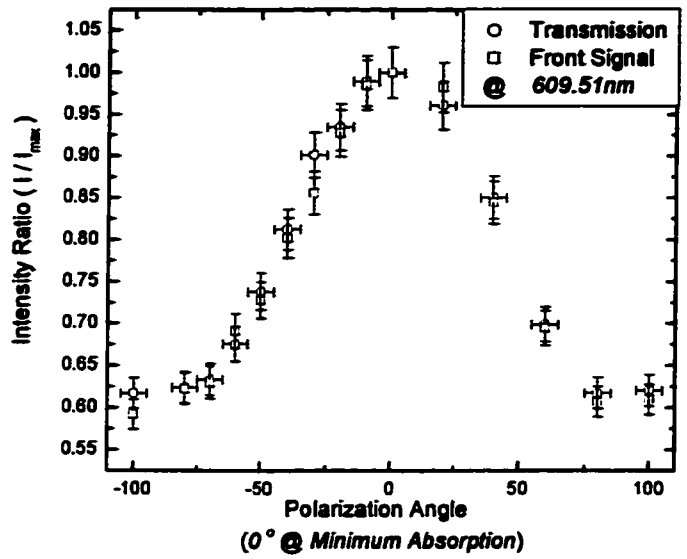

Figure 3.11: Front signal relative intensity variation with polarization; front and transmission variations are identical.

finally a large signal is observed near resonance which combines all of the front signal constituents.

To better illustrate the three components of the front signal, a schematic of the three processes is offered in figure 3.10. Diagram A illustrates the first metallic signal generated instantaneously directly into the electrodes. Diagram B presents the second mechanism involved in the creation of the front signal. Part of the light is scattered toward the electrodes and is not absorbed until it reaches the back surface of the crystal; it then generates a localized exciton density which is detected immediately. Finally, diagram C shows how the diffusive signal is generated; as the beam traverses the crystal, it is scattered in all directions, creating a decreasing density of excitons along the main axis. As these excitons diffuse toward the detector, driven by a density gradient (as discussed in section 1.2.4), they generate a long time-delayed signal.

3.2.2 Front Signal Variation with Polarization

To further our study of the front signal, we take a look at its variation with polarization at resonance; this may help isolate the front's effect on a travelling condensate as studied in the next chapter. In figure 3.11, the front signal amplitude and the optical transmission along the secondary axis (also seen in figure 3.5) are plotted with angle

of light polarization. In both cases, quantities are normalized using respectively, the detected maximum front amplitude and transmitted intensity; this thus provides a measure of how much each signal is affected by polarization. This figure clearly illustrates that the front varies much like the transmission, both curves peaking at the minimum absorption angle and displaying the same relative variation with polarization; this was verified for both available crystal axes. If the above results were caused by Rayleigh scattering, maximal front signals would be detected for a vertical polarization only (which, as discussed in section 2.5.2, would scatter light horizontally along the main axis toward the electrodes), independent of the crystal orientation; the above result thus suggests that the front signal's variation is related to the polarization-dependent absorption along the crystal's secondary axis (absorption is polarization-independent along the main axis [111]: table 2.1). Near the minimum absorption angle, less light is absorbed along the secondary axis, and therefore more light is accessible for scattering along the main axis; a larger front signal is detected. Away from the minimum absorption angle, more light is absorbed along the secondary axis, and less light is scattered towards the electrodes; the front signal is smaller. (*N.B: No off-resonance variation with polarization is detected in the metallic front signal; if Rayleigh scattering were of concern, this signal would vary.*)

In figure 3.13, we look at the same front polarization variation as above, but at various points in the time-resolved signal (figure 3.12). This permits to verify whether the front intensity dependence on polarization is strictly limited to the instantaneous excitonic signal (figure 3.10 B) or whether it is also observable in the diffusive component of the signal. Figure 3.12 shows a time-resolved front signal (for a certain polarization), and indicates the various times at which polarization variations will be studied. In figure 3.13, the relative variations in polarization are depicted for the selected times, showing a similar variation throughout the signal. The entire exciton density along the main axis induced by the lateral pulse thus varies with polarization as does the front and transmitted intensities. This observation will be of importance for the condensate amplification studies presented in the next chapter.

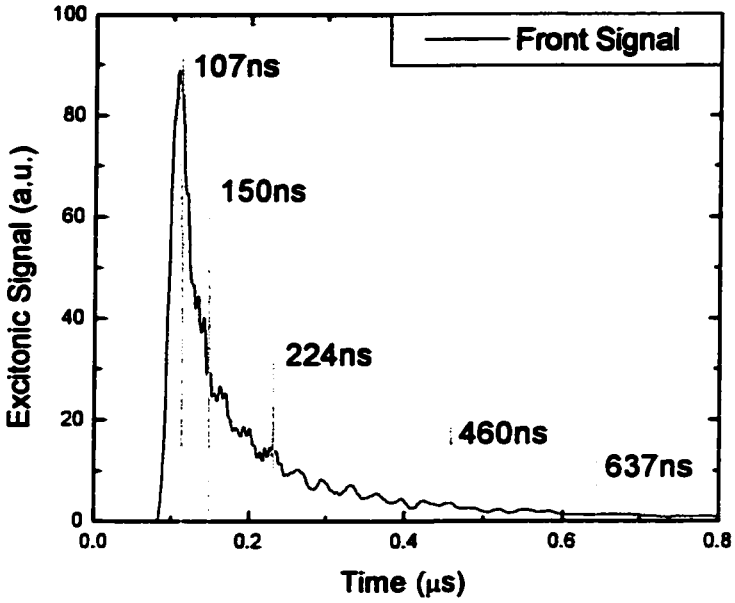

Figure 3.12: Typical time-resolved front signal at resonance. Vertical lines indicate times at which polarization measurements are made for analysis in fig 3.13

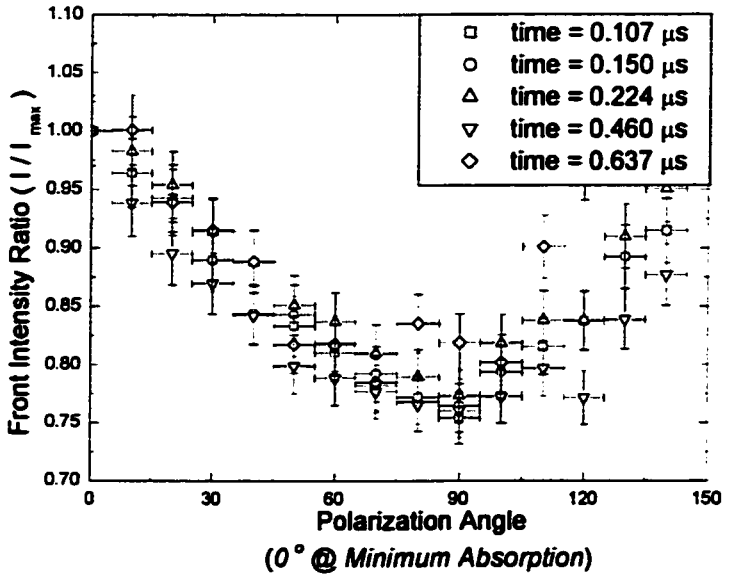

Figure 3.13: Front signal relative intensity variation with polarization; measured variations are similar throughout the duration of the signal.

Chapter 4

Condensate Amplification and Anomalous Differential Attenuation

In the present chapter, results are presented on interactions observed between a travelling condensate and a secondary pulse excitation tuned either around the 1S orthoexciton resonance or near the band edge. In the first section, condensate amplification will be discussed in detail, presenting the various parameters that influence the extent of the amplification experienced by a given exciton packet; such parameters include secondary excitation wavelength, polarization and intensity, as well as the relative time delay separating the initial YAG pulse (which creates the travelling condensate) and the secondary pulse (which probes and amplifies the condensate). The next section (4.2) then discusses other effects related to condensate-secondary pulse interactions measured through the differential attenuation of transmitted and scattered light. Throughout the chapter, efforts are aimed at determining how the secondary excitation behaves in the presence of a condensate, and how these interactions can be used to explain the observed condensate amplifications. Due to the length of this chapter, all key results will then be discussed again in chapter 5, where they will be used, in conjunction with previous results obtained by Benson [6] and Massé [14], to elaborate a plausible model for condensate amplification.

4.1 Exciton Condensate Amplification by Lateral Secondary Excitation

It was previously observed that when an excitonic Bose condensate is illuminated by a secondary CW light source tuned around the band edge, it is significantly amplified [5].

Later, it was demonstrated that a similar amplification takes place when a pulsed secondary excitation, tuned near the band edge or at the 1S orthoexciton resonance, is used instead of a CW light source [13, 14]. The pulsed excitations offer various advantages over the CW radiation. For one, the pulses contain a countable number of photons, with a well defined spectral distribution; the CW is less stable, displaying spectral shifts (greatly affecting experiments at resonance) and large intensity variations. As the CW laser is continuously filling the crystal with cold excitons, it is impossible to probe only a specific part of the travelling exciton packet; however this can be done with pulsed illumination through carefully synchronized probe-condensate delays. For these reasons, the present section will discuss results obtained using secondary pulsed excitation of the condensate; in all cases, the orthogonal double pulse experimental setup presented in figure 2.10 is utilized.

The initial condensate is predicted (in [6, 13, 14]) to consist of a comet-like construction; its constituents include a condensed core, surrounded and followed by an uncondensed coma and tail respectively. As suggested in section 1.2.4, the passage of such exciton packets (accompanied by the many phonons generated during its creation) will also induce a local distortion in the sample, much like that observed when a crystal is submitted to an external stress. Probe-condensate experiments then deal with interactions between the probe, the excitons within and around the condensate, and the locally distorted crystal.

The secondary pulse, which can be time-delayed to intersect the travelling packet's path at various points before or within the comet-like structure, interacts with one (or various) part(s) of the packet and amplifies it to produce signals like the one presented in figure 4.1 (from [34]). Notice that the secondary pulse, as presented in section 3.2, will produce a series of signals on its own which need to be considered to fully analyze the observed condensate amplifications. For example, the study of front effects on detected excitonic signals will be considered, providing information on the influence of excitons created along the crystal main axis (figure 2.9) by the absorption of scattered light. It will be shown that although the fronts have an effect on the detected condensate signals, they do not play a key part in condensate amplification per se. Instead, results indicate that only the excitons directly created within and around the packet actively participate in the amplification process of interest. Note that, as mentioned in section 1.3, the cold excitons created by the secondary pulse do not produce the detected amplifications by their simple addition to the condensate. Rather, results suggest that the significant gains in excitonic signals are generated by the further condensation of the initial high density

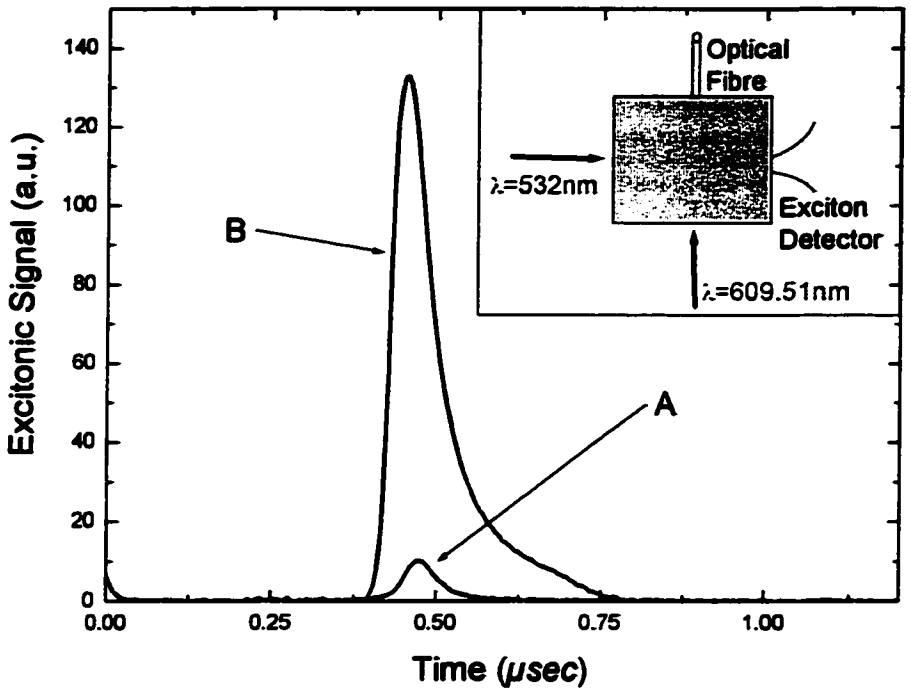

Figure 4.1: Excitonic Bose-Einstein condensate amplification by sequential orthogonal excitation of sample (1). A) Condensate created by a YAG pulse ($I \sim 100\, I_0$) incident on the front face of the crystal. B) Lateral condensate amplification by a relatively weak secondary resonant pulse ($I \sim 0.15\, I_0$) synchronized to meet the condensate at the center of the crystal. Inset: Experimental configuration. [34]

incoherent excitons travelling in the comet-like packet coma and tail, induced by the presence of the local secondary cold exciton population.

In figure 4.1 (from [34]), typical amplification by resonant secondary pulse excitation is clearly depicted; the experimental setup utilized to generate the observed signals is illustrated in the inset. Trace A) represents an excitonic condensate created by single YAG illumination ($I \sim 100\, I_0$) and trace B) represents the amplified condensate when a secondary pulse excitation tuned at the 1S orthoexciton resonance ($I \sim 0.15\, I_0$) is synchronized to meet the condensate at the center of the sample. The ratio of signal amplitudes, hereafter termed the amplification factor, is significant when one considers the relatively modest intensity of the secondary pulse.

In the next few subsections, such signals will be analyzed with the variation of probe wavelength, intensity, polarization and synchronization with the travelling packet. This

will help illustrate that amplification is strictly induced by cold excitons directly created within and in the near vicinity of the condensate.

4.1.1 Amplification Variation with Secondary Excitation Wavelength

The first step taken to study condensate amplification is to observe how this effect varies with secondary excitation wavelength. In figures 4.2 and 4.3, amplified condensates, and their related front signals, are temporally and spectrally resolved, showing the onset of the amplification phenomenon at resonance and around the band edge. Results are provided by lateral illumination of both samples (1) and (F) respectively (samples discussed in section 2.3.1) at secondary excitation wavelengths ranging from approximately $603\,nm$ to $611\,nm$; in both cases, the secondary pulse is synchronized to meet the travelling exciton packet at the center of the sample. Notice that although both crystals present different signal amplitudes, the same general tendencies can be observed in either graph. Amplification reaches a maximum around the orthoexciton resonance, and again near the band edge. For wavelengths where there is no absorption, either between $607 - 609\,nm$, or beyond $610\,nm$, only the initial YAG induced condensate is detected; there is no amplification. Also notice that as wavelength is reduced around $603\,nm$, amplification starts to disappear. This is because the absorption coefficient rapidly becomes too strong and the secondary pulse can hardly reach the packet to amplify it; notice that no front signal is observed either (fronts discussed in section 3.2).

The quantitative differences observed between graph 4.2 and graph 4.3 are most likely related to the crystals' purities. In sample (1), travelling exciton packet signals are strong. This means that relatively weak YAG intensities can still produce detectable exciton packets; this sample was used in the past [6, 14] to monitor condensation thresholds with regards to initial YAG intensities, and hence to initial local exciton densities, and temperature. In comparison, travelling exciton packet signals in sample (F) are very weak; single YAG illumination condensates are therefore very hard to observe, their generated excitonic signals being of the order of our equipment's sensitivity limits. In addition, amplified signals are still somewhat weak, forcing us to operate at relatively high YAG and dye laser intensities in order to produce signals of sufficient amplitudes for analysis. Finally, front signals in sample (F) are relatively strong (as seen in figure 4.3) compared to those generated by the condensates; this provides an additional problem. As will be discussed shortly, front-induced signals in the detected exciton packets are

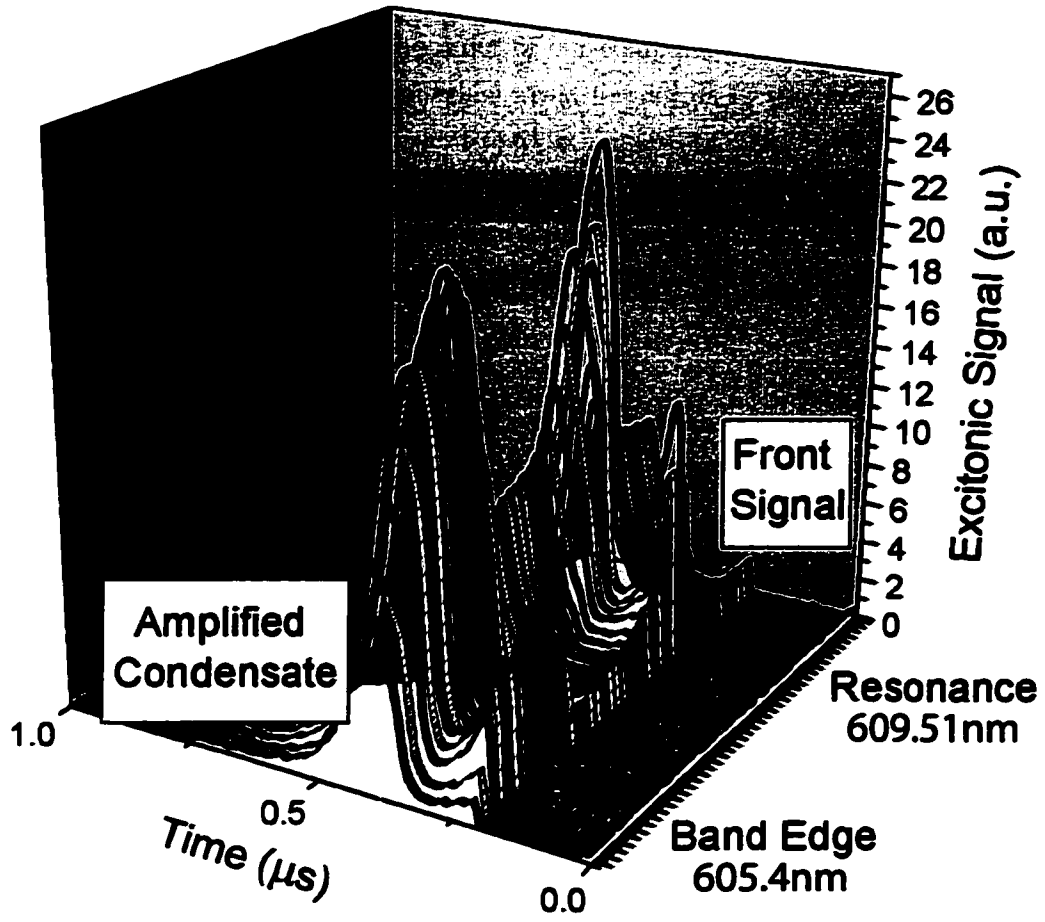

Figure 4.2: Excitonic Condensate amplification by synchronized lateral secondary excitation. Amplification is maximal around the band edge and at the 1S orthoexciton resonance. (Sample (1): $I_{YAG} \sim 10I_0$, $I_{Probe} \sim 0.3I_0$)

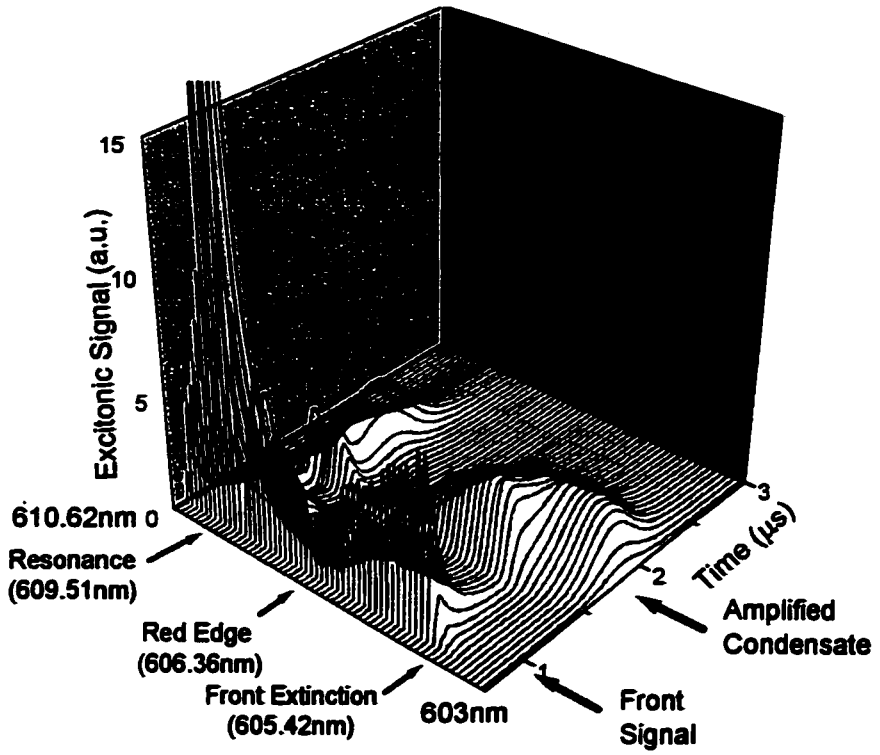

Figure 4.3: Excitonic Condensate amplification by synchronized lateral secondary excitation. Amplification is maximal around the band edge and at the 1S orthoexciton resonance. (Sample (F): $I_{YAG} \sim 100I_0$, $I_{Probe} \sim 0.3I_0$)

of little interest as they do not represent an actual part of the condensate. This leading edge "shoulder", present in amplified condensate signals shown in figures to come, appears only for strong relative front signals, which are unfortunately inevitable in sample (F). Yet, its appearance will later help dismiss the front's importance in condensate amplification. Sample (F) is then mainly used in polarization experiments for its polarization dependence in absorption along certain crystal axes. Nonetheless, amplification experiments with both crystals offer similar qualitative results. In any case, the sample studied in a given graph will be specified if needed to remove confusion.

We first take a closer look at condensate amplification around resonance. In figure 4.4, a strong initial condensate is amplified in sample (1). For clarity, the initial unamplified condensate is presented, marked here for secondary excitations of $608.62\,nm$ and $610.62\,nm$ where there is no absorption, and hence, no amplification. Amplification only occurs when the probe is tuned at resonance; otherwise, secondary excitation has

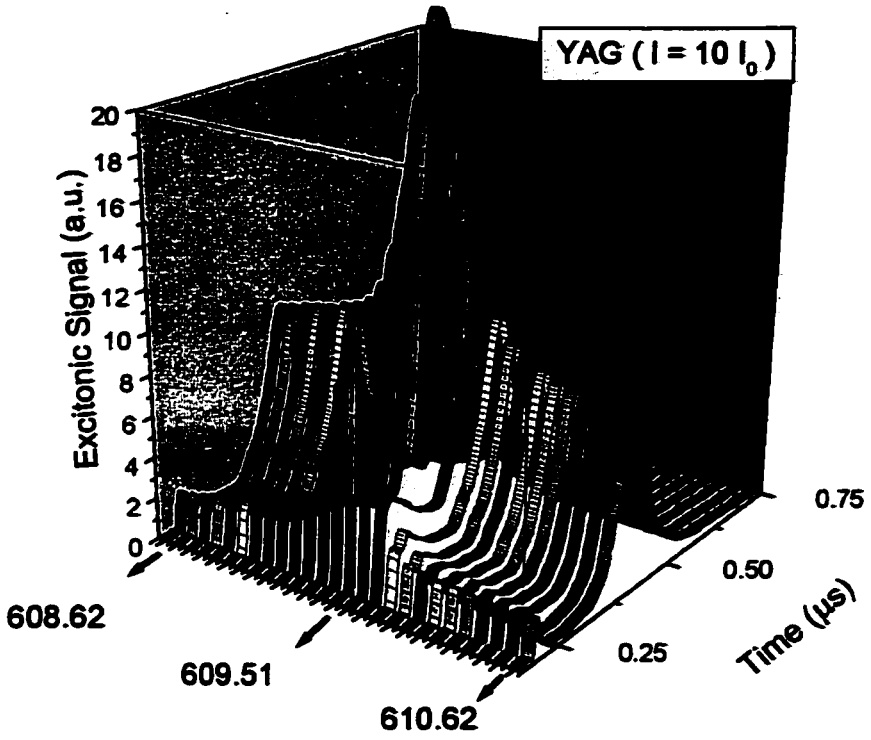

Figure 4.4: In the presence of an initially condensed packet, the amplified signal does not significantly change shape or velocity. It is a sharp resonant effect.(Sample (1): $I_{YAG} \sim 10I_0$, $I_{Probe} \sim 0.3I_0$)

no effect on the initial signal. Since the initial exciton packet is already in a condensed state, it presents a nice solitonic temporal distribution. Clearly, variations observed in the condensate amplitude with probe wavelength shows amplification as a sharp resonant effect. In figure 4.5, the same traces are plotted once again, this time giving a better impression of the shape variations encountered as the secondary wavelength nears resonance. The bottom trace, taken at $608.62\,nm$, is not amplified, showing the smooth solitonic shape of the YAG-induced condensate. As the wavelength is increased, the condensate is amplified with no significant increase in velocity. At the same time, the front signal increases, and a front-induced shoulder appears to intermixe with the condensate to produce the observed combined signal. At resonance, both are indistinguishable.

From the figure 4.5, one could argue that the condensate does not actually experience an amplification, but that its leading edge front-induced signal blends into the condensate signal to give the impression of amplification; figure 4.6 helps to dismiss this argument.

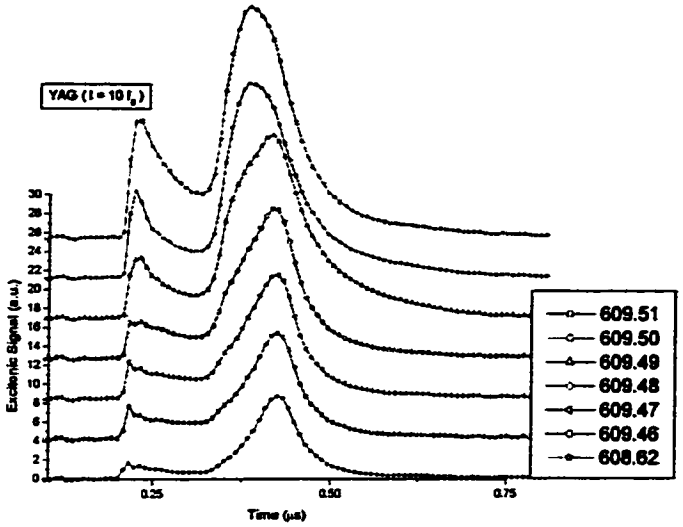

Figure 4.5: A resonantly amplified condensate increases in amplitude but is not significantly accelerated. The front-induced shoulder and the condensate are indistinguishable at resonance. (Sample (1): $I_{YAG} \sim 10I_0$, $I_{Probe} \sim 0.3I_0$)

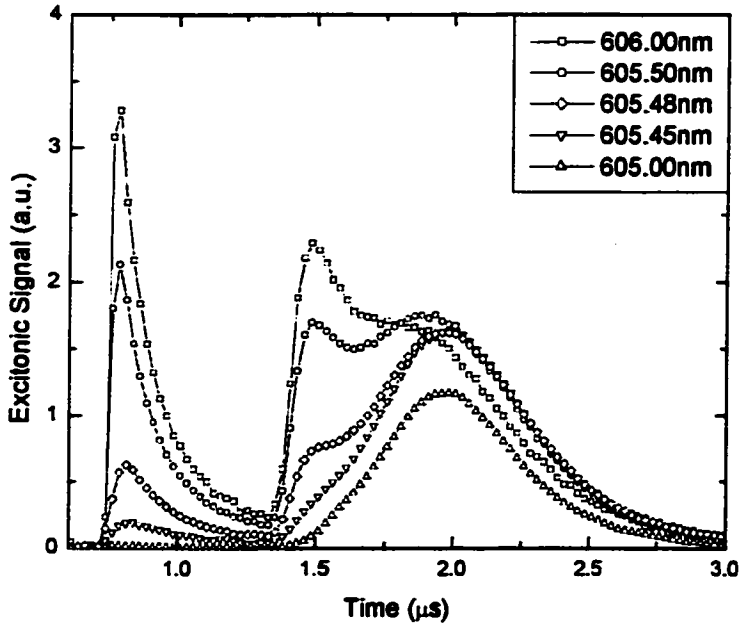

Figure 4.6: Synchronized lateral condensate amplification around the band edge illustrates the existence of a front-induced shoulder detected with the amplified condensate. (Sample (F): $I_{YAG} \sim 100I_0$, $I_{Probe} \sim 0.3I_0$)

In this figure, amplification takes place for a secondary excitation wavelength around the band edge. The first signal, which is detected at approximately $750\,ns$ (appropriate delay for probe-packet synchronization in sample (F)) is attributed to the front signal, discussed in detail in section 3.2; it displays a sharp instantaneous peak, followed by a diffusive tail. The second pulse detected is the amplified condensate[1]. When the probe is tuned at $605\,nm$, absorption is too strong to produce a front signal[2]; the detected amplified condensate is nicely distributed. As the wavelength is increased, so is the front, which induces the additional signal in the leading edge of the amplified condensate. This front-induced "shoulder" is strictly related to the cold exciton population created along the main axis by the scattered probe. Results presented later (section 4.1.3) will help to support this contention. It is proposed that as the condensate travels along the main axis (along with the local crystal distortion it generates), the cold excitons found in its path that were not directly created in its vicinity (within the condensate and its surrounding incoherent cloud) will be trapped within the leading coma of the travelling comet-like packet, amplifying it considerably. Whether this gain can be significant enough to induce a micro-condensation of the leading incoherent coma is still quite uncertain (and difficultly verifiable). This front-induced shoulder is then of secondary interest in this thesis, as it does not seem to participate directly in the amplification of the initial condensate.

4.1.2 Amplification Variation with Secondary Laser Intensity

Another parameter which may be varied to study condensate amplification is the secondary pulse intensity. Although it has been studied before [6, 14], it is important to review how amplification varies with probe intensity to better analyze results on polarization in the next section (4.1.3)

In figure 4.7, amplified condensate amplitude variations with secondary pulse intensity are plotted over many orders of magnitude. Clearly, as the intensity increases, so does amplification; yet, as reported in [5], when the probe intensity becomes too high, saturation is observed. For the purpose of this thesis, we content ourselves with a simple

[1]Notice that the single YAG-induced packet does not show on this graph. Since these results were obtained with sample (F), the unamplified packet is too small and noisy to be displayed successfully with the other traces.

[2]Even though absorption is high, light can still reach the travelling packet, where it can create the cold excitons that induce amplification. Yet, higher absorption means that less light will be scattered toward the electrodes, and what little light is scattered, will be quickly absorbed near the packet. This is why no front is observed while amplification still takes place.

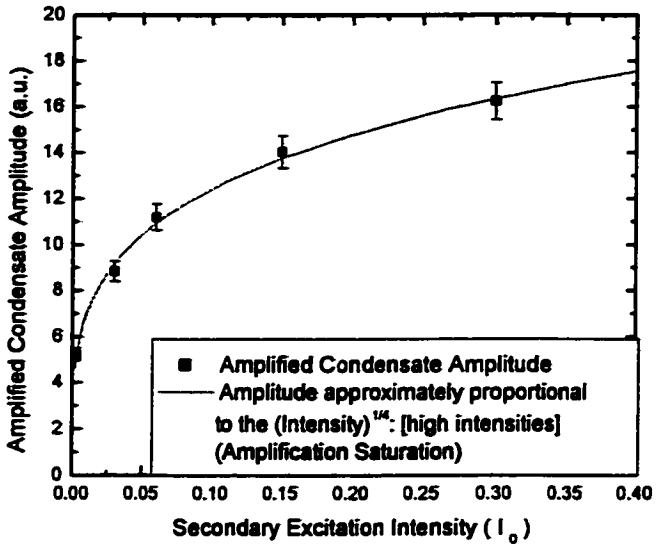

Figure 4.7: Amplified condensate amplitude variation with resonant secondary excitation intensity (high intensity regime). YAG intensity remains constant at $\sim 10\,I_0$ (Sample (1)). The condensate and the secondary pulse are synchronized to meet at the center of the crystal.

fit of these few points. All we need for the next section is a variation tendency, and hence, the fit presented in figure 4.7 provides sufficient information; we observe that the amplified condensate amplitude, which could just as well be replaced with the amplification factor, is approximately proportional to the probe intensity to the one fourth (exponent fitted to 0.250 ± 0.008).

In figure 4.8, amplified condensate amplitude variations with secondary pulse intensity are plotted, this time, in the lower intensity region. In this regime, amplification does not saturate, and is observed to be relatively linear with intensity. Since we do not reach saturation, the more we inject excitons into the initial packet, the more it is amplified.

The reason we look at these two regimes is to predict what to expect in other experiments where the secondary excitation intensity is not varied directly, but through polarization-dependent absorption. In the next section, experiments conducted in sample (F) deal with probe polarization. Of course, as mentioned before, signals in this sample are relatively weak, and therefore, we must operate at high YAG and probe intensities. We thus operate in the high intensity regime presented in figure 4.7 where amplification varies sublinearly with intensity. We keep this in mind while studying the results presented in the next section.

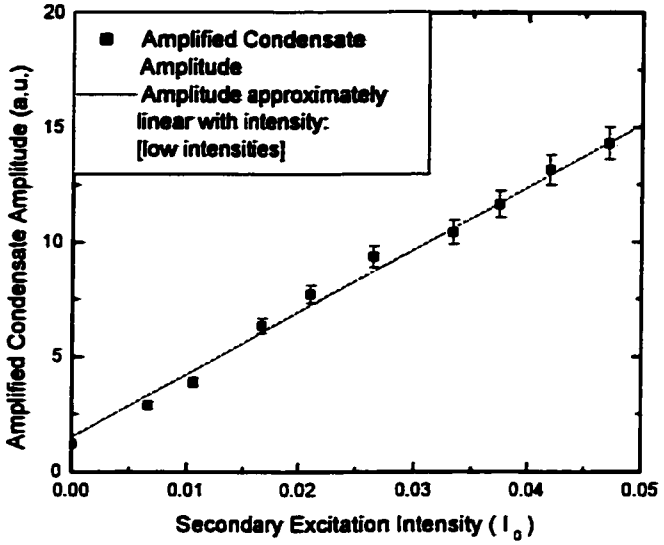

Figure 4.8: Amplified condensate amplitude variation with resonant secondary excitation intensity (low intensity regime). YAG intensity remains constant at $\sim 10\, I_0$ (Sample (1)). The condensate and the secondary pulse are synchronized to meet at the center of the crystal.

4.1.3 Amplification Variation with Secondary Excitation Polarization

The resonant secondary excitation's polarization is a useful tool in our condensate amplification experiments; by varying the probe polarization at resonance, we consequently vary the number of cold excitons created along the secondary axis, and as presented in section 3.2.2, along the primary axis as well. Essentially, this method for varying the cold exciton population in our sample differs from that of varying the secondary laser intensity as it provides a greater contrast between light-induced and exciton-induced phenomena. Simply, when absorption is maximal, less light is available for transmission and scattering; this results in the observed minima in front signals. As the polarization angle is rotated, less light is absorbed, therefore less excitons are created along the secondary axis, and more light is available for scattering, hence the stronger front signals. The simple rotation of the angle of polarization then both reduces (increases) the amount of excitons created along the secondary axis while increasing (reducing) the amount of light wandering within the crystal; this then provides better contrast between various effects, which, as we will see shortly, vary differently with variations in probe polarization.

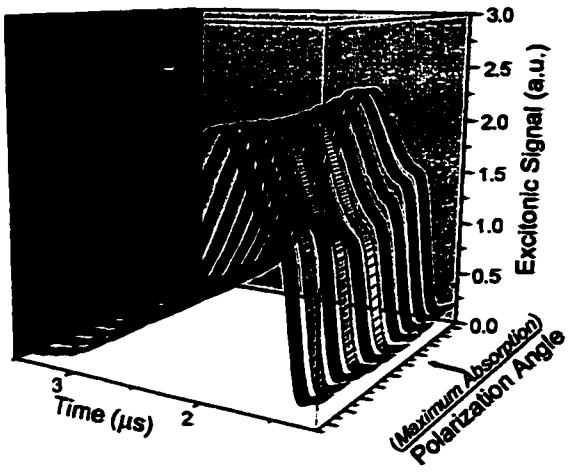

Figure 4.9: Amplified condensates for various resonant secondary excitation polarizations. Secondary pulse delay $\sim 830\,ns$. (Sample (F): $I_{YAG} \sim 100I_0$, $I_{Probe} \sim 0.3I_0$)

Varying the probe intensity, on the other hand, would not provide as good a contrast, as an increase (decrease) in intensity would correspond to both an increase (decrease) in the number of excitons created along the secondary axis and an increase (decrease) in the number of wandering photons. As we will see, probe polarization experiments will help support our contention that amplification is not generated by cold excitons present throughout the crystal volume, but induced only by those created within the "interaction volume" generated by the passage of the initial excitonic packet. Results will reinforce observations in section 4.1.1 which indicated that the front signals, generated by the diffusion of excitons along the main axis, are not responsible for the amplification of interest, but only for the creation of an additional leading-edge shoulder detected with the amplified condensate.

The sample is excited by a lateral beam tuned at resonance. Since both the $[1\bar{1}0]$ and the $[11\bar{2}]$ axes in sample (F) present polarization-dependent absorption, they are used interchangeably, presenting identical qualitative results[1]. In figure 4.9, amplified condensates are plotted versus secondary resonant pulse polarization; the secondary pulse is synchronized to meet the condensate at the center of the crystal (this corresponds to a YAG-secondary pulse delay of $\sim 830\,ns$). Both the amplified packet and the front-induced shoulder show a mild variation with polarization, yet the latter's variation seems slightly more pronounced than the former. Most likely, the condensate variation with

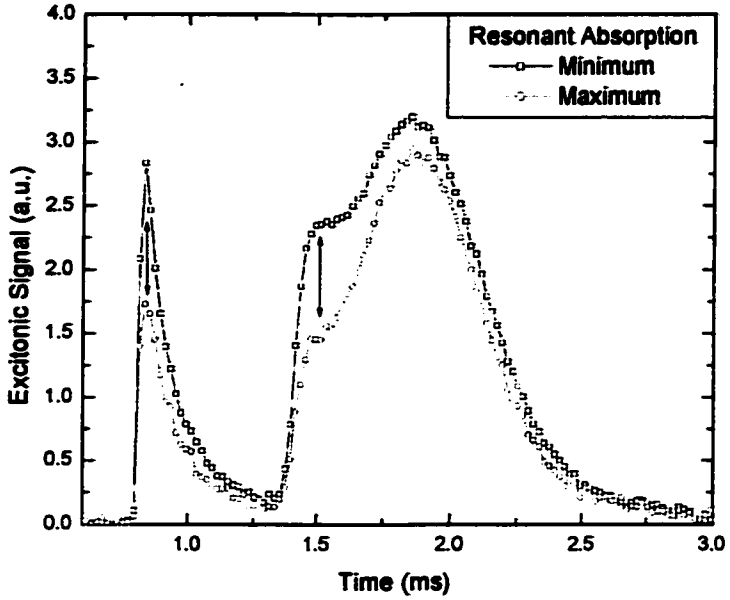

Figure 4.10: Fronts and amplified condensates for two resonant secondary pulse polarizations. The front and front-induced shoulders vary with polarization. Secondary pulse delay $\sim 830 ns$. (Sample (F): $I_{YAG} \sim 100 I_0$, $I_{Probe} \sim 0.3 I_0$)

probe polarization is a simple remnant of the front-induced signal tail.

In figure 4.10, two of the traces from figure 4.9 are plotted again, this time next to their respective front signals for two secondary pulse polarizations (minimum and maximum resonant absorption). Clearly, when the front is minimal, so is the amplified condensate, and vice versa. Interestingly, the front-induced shoulder's variation with polarization is clearly more pronounced than the amplified packet's, and more particularly, the front-induced shoulder and the front signal variation with polarization are of similar amplitudes. This strongly supports the contention of a combined amplified signal, comprised of both a front-induced hump, likely attributed to an amplification of the front of the travelling comet-like packet's coma, and a front-independent amplified condensate, the signal of interest. To strengthen this argument, we look at figure 4.11 which plots the amplified condensate's relative variation with polarization and compares it with the appropriate absorption and front signal relative variations with polarization. While the

[1]Reminder: As presented in section 2.3.1, all polarization-related experiments are conducted in sample (F). Since excitonic signals are relatively weak in this sample, high laser intensities are required. Typically, $I_{YAG} \approx 100\, I_0$ and $I_{probe} \approx 0.3\, I_0$; this puts us in the saturated amplification regime presented in figure 4.7.

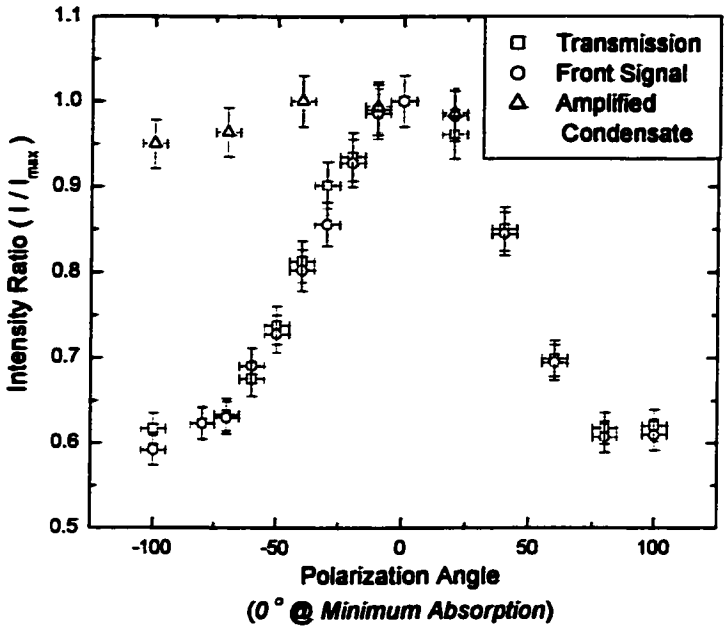

Figure 4.11: Amplified condensate variation with polarization is negligible compared to the front and the absorption variations.(Sample (F): $I_{YAG} \sim 100I_0$, $I_{Probe} \sim 0.3I_0$)

front and absorption points display a noticeable 40% variation with polarization, the amplified condensate only records a negligible 5% which could easily be attributed to the front-induced shoulder's tail.

To further support this argument, we study similar traces for various secondary pulse delays. In figure 4.12, two traces are plotted for a YAG-secondary pulse delay of $\sim 490\,ns$. At this point the front has a noticeably smaller effect on the amplified packet as there is greater separation between the front and amplified signals. Accordingly, the front's variation with polarization is less noticeable in the amplified condensate signal as the front-induced shoulder is necessarily smaller. Pushing further, figure 4.13 plots the same traces for a shorter delay of only $210\,ns$. This time, no polarization variation is detected in the amplified condensate and the front-induced shoulder is practically non-existent.

Clearly, whatever polarization-dependent variation is observed in the amplified condensate is likely attributable to the front-induced shoulder discussed in the previous section (4.1.1). This is then of secondary interest; yet, it helps support the argument that the diffusive excitons participating in the creation of the front signals are irrelevant in direct condensate amplification. What remains to be discussed, is why amplification itself does not display any variation with probe polarization.

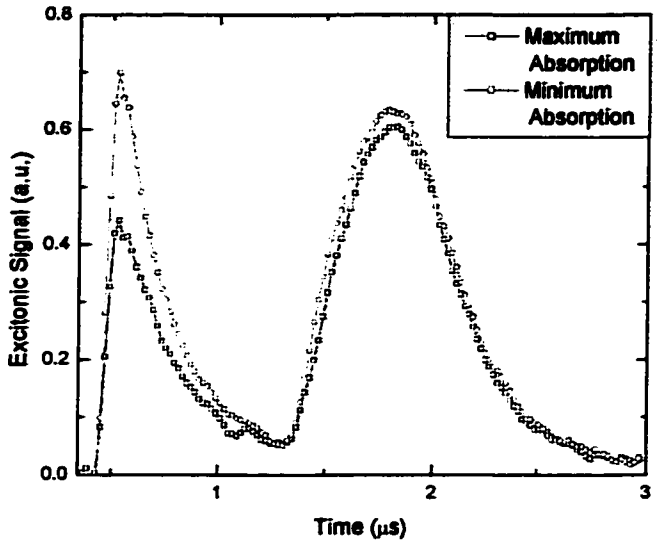

Figure 4.12: Fronts and amplified condensates for two resonant secondary excitation polarizations. The front-induced shoulder is slowly disappearing as the secondary pulse delay is shortened. Secondary pulse delay $\sim 490\,ns$. (Sample (F): $I_{YAG} \sim 100I_0$, $I_{Probe} \sim 0.3I_0$)

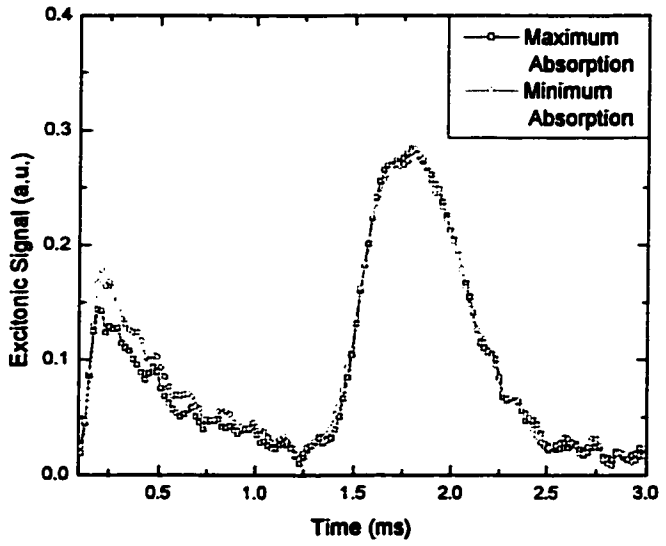

Figure 4.13: Fronts and amplified condensates for two resonant secondary excitation polarizations. The front-induced shoulder is essentially non-existent and the amplified signal does not display any variation with polarization. Secondary pulse delay $\sim 210\,ns$. (Sample (F): $I_{YAG} \sim 100I_0$, $I_{Probe} \sim 0.3I_0$)

A first explanation for the lack of polarization dependency in condensate amplification deals with the local crystal perturbation induced by the passage of the initial exciton packet. As we presented in section 1.2.4, crystal absorption is likely locally altered in the presence of a condensate. As will be further discussed in section 4.2, the packet-induced distortion is observed to locally broaden the resonant absorption line and break the crystal symmetry related polarization-dependent absorption. This would thus entice a polarization-independent absorption in and around the condensate, for any crystal orientation. If amplification is in fact induced by the local absorption of light within the exciton packet "distortion volume", then it will be necessarily polarization-independent as well. As we will see in later results, this model is quite plausible. Yet, another matter remains. Even if amplification is a result of polarization-independent local absorption, the amount of light reaching this "distortion volume" will vary slightly with polarization nonetheless; as light absorption outside the interaction volume varies, so will the light intensity reaching the packet. We thus turn to figures 4.14 and 4.15 to explain what happens.

In figure 4.14, the comet-like exciton packet is shown as travelling through the center of the crystal. The probe, aligned and synchronized to meet the packet in its locally distorted volume, will interact with a small part of the packet. If we zoom into this region, delimited by the dashed lines and depicted in figure 4.15, we can approximately divide our crystal into two absorptive regions: a normal, symmetry-conserving region displaying the expected polarization-dependent absorption, and a locally distorted region where symmetries are removed and where absorption remains constant with polarization. Evidently, the amount of light reaching the interaction region where amplification takes place is determined by the amount of light that is transmitted through the first unperturbed section. By calculating the intensity variations observed at the distortion region boundary, we can assess, using results from the previous section (4.1.2), what kind of amplification variation with polarization could be expected.

Since we do not know the exact size of the interaction region, we will assume that we can subdivide our sample into three equal sections. If anything, the local distortion volume should be larger than 1/3 of the crystal since the initial YAG excitation spot on sample (F) consists of a $4\,mm$ diameter circle on a $4.7\,mm \times 4.9\,mm$ crystal surface. For simplicity, we will use a $4.8\,mm$ crystal cross-section, dividing our crystal into three equal sections of $\approx 1.6\,mm$ in depth. Using $\alpha = 3.5\,cm^{-1}$ for the absorption coefficient in Cu_2O at $\lambda = 609.51\,nm$, and $x = 0.16\,cm$ in the Beer-Lambert equation (eq. 1.17), we obtain $I_{min} \approx 0.57 I_{max}$, where I_{max} (I_{min}) is the intensity at the zone boundary for forbidden

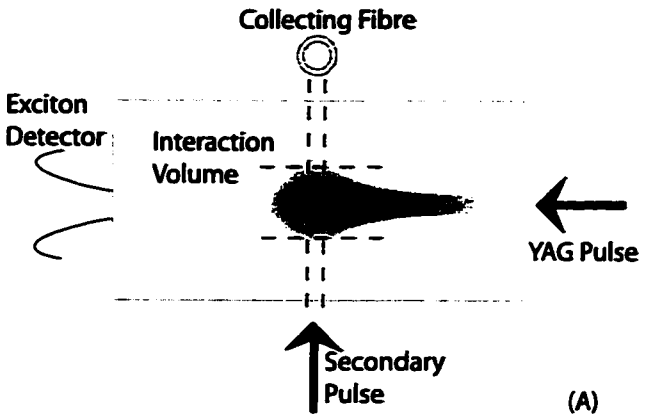

Figure 4.14: Depiction of interaction volume, delimited by the dashed lines, involved in condensate amplification.

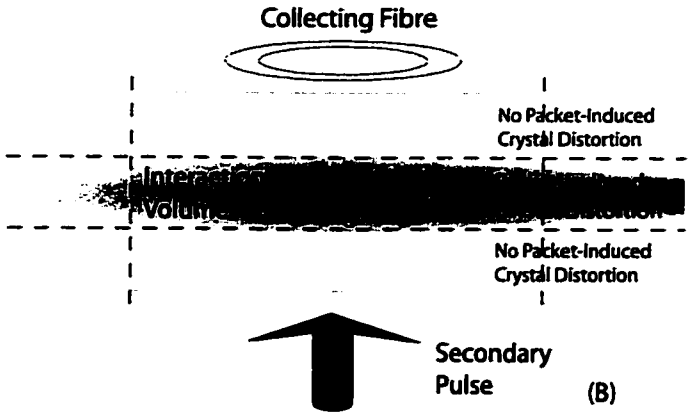

Figure 4.15: Interaction volume for condensate amplification: packet-induced crystal distortion removes symmetries.

(permitted) absorption. This provides a maximal intensity variation observable at the interaction region boundary for absolute polarization-dependent absorption in region 1 of $\approx 43\%$. Now, since we operate at relatively high probe intensities in this sample, we recall (section 4.1.2) that $Amplification \propto I_{probe}^{1/4}$. Therefore, for a 43% intensity variation at the zone boundary, we can only expect a $\approx 13\%$ amplification variation with polarization. This, of course, is for a perfectly polarized and collimated beam, whose absorption in region 1 is 100% polarization-dependent. In addition, this calculation assumes an interaction region size which may in fact be somewhat underestimated. Keeping this in mind, it comes to no surprise that no amplification variation with polarization greater than a few percent is detected in our experiments.

The above arguments, combined with results presented in this section and section 4.1.1, help to support our model on condensate amplification. The latter suggests that excitons, created locally by the dye laser within an interaction volume induced by the passage of the initial exciton packet, will generate the observed amplification by inducing the condensation of neighboring quasi-condensed excitons present in the comet-like packet coma and tail. We propose, based on the experimental observations presented in this chapter, that neither the excitons created outside the local crystal perturbation along the secondary axis, nor the diffusive excitons created along the main axis in front of the travelling packet contribute to the direct primary amplification process of interest. The next section, dealing with additional probe absorption observed in the presence of a travelling exciton packet will support this model, leading to a better characterization of the packet-induced local crystal distortion.

4.2 Normalized Differential Attenuation

To further investigate the effects of the secondary excitation in our condensate amplification experiments, we study the normalized differential attenuation (NDA), a resonant effect related to the passage of the exciton packet. The NDA is defined as $(I - I_p)/I$ where I (I_p) is the residual lateral laser pulse intensity as detected by the collecting fibre in the absence (presence) of an exciton packet. Similar measurements were shown to be useful in the detection of cold excitons in Cu_2O by differential transmission spectroscopy (DTS) [35]. However, while such results relate to the screening of np absorption lines, those presented in the present chapter pertain to the additional absorption of the secondary excitation detected at the 1S orthoexciton resonance (section 4.2.1).

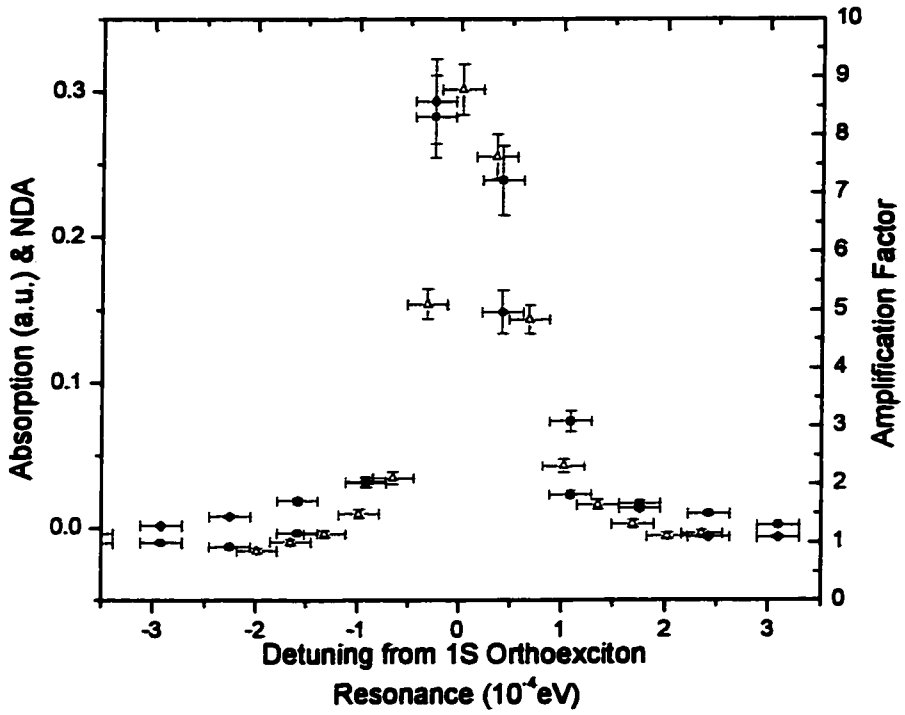

Figure 4.16: NDA and condensate amplification variation near resonance (zero detuning mark at 1S orthoexciton resonance). Left axis: relative absorption (solid squares) and NDA (solid circles). Right axis: amplification factor (open triangles). (Sample (F): $I_{YAG} \sim 100 I_0$, $I_{Probe} \sim 0.3 I_0$)

4.2.1 NDA: A Resonant Effect

Figure 4.16 plots the NDA, the amplification factor (defined in section 4.1) and the relative absorption spectrum in the vicinity of the $n = 1$ exciton line; the zero detuning mark is set on the 1S orthoexciton line ($2.033\,eV$, section 1.2.2). Both the condensate amplification and the NDA are clearly seen to be sharp resonant effects within the limits of the laser bandwidth (section 2.1.1). For amplification, this strongly points to an excitonic effect, as no amplification is detected off-resonance (as seen in section 4.1.1). As for the NDA, a few explanations can be put forward to explain this effect.

For starters, one could predict a resonant interaction between the excitons in and around the condensate, and the stimulating photons themselves; this first mechanism is unlikely. As discussed in section 1.2.2, direct absorption in the paraexciton state is forbidden. We thus first create orthoexcitons (whose transition is quadrupole permitted),

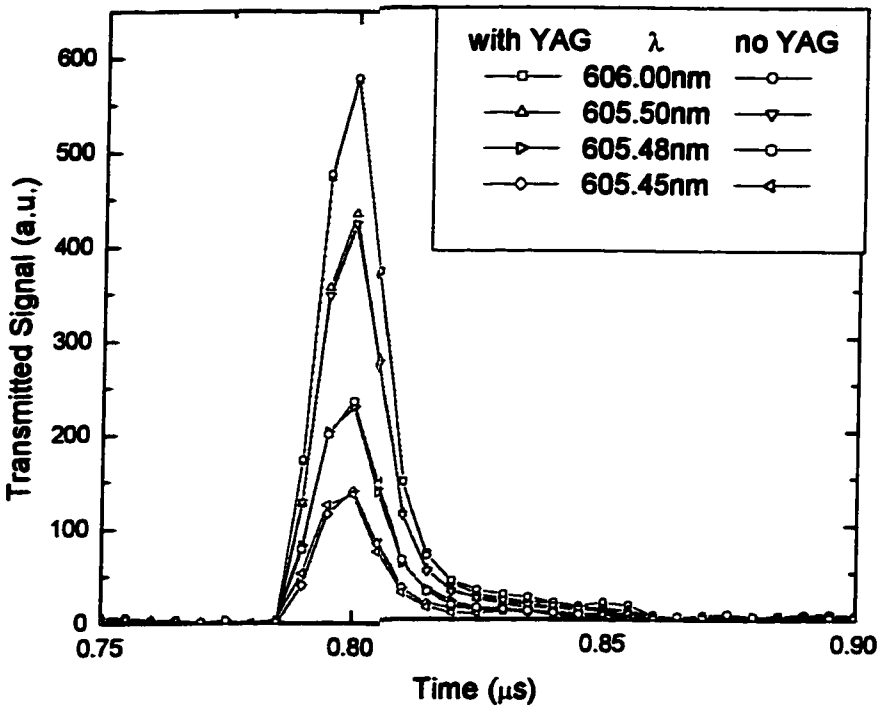

Figure 4.17: Transmitted intensities around the band edge in the presence and in the absence of YAG illumination. No NDA is observed. (Sample (F): $I_{YAG} \sim 100 I_0$, $I_{Probe} \sim 0.3 I_0$)

which will then down convert to their less energetic counterpart ($\Delta E \approx 12 meV$), the paraexciton. This thus means that probe photons are not resonant with packet excitons, but resonant with crystal absorption. Another explanation for the NDA effect could reside in some type of resonant scattering event. The probe, reaching the condensate and its surrounding excitons, could be additionally scattered away from the secondary axis, resulting in a reduced transmission measurement. Yet, results in section 4.2.4 will show that measured scattered signals (front signals - section 3.2) show no sign of increase in the presence of a condensate. Actually, they will be shown to experience similar attenuations, which leads us to the most probable explanation for NDA.

As proposed in sections 1.2.4 and 4.1, the passage of comet-like exciton packets, composed of condensed and quasi-condensed particles, will generate a local crystal distortion. It is believed that this packet-induced distortion will locally broaden the orthoexciton absorption line. Since our probe laser's bandwidth is somewhat larger than the absorption

line itself ($\sim 60:1$), this broadening will manifest itself as a measured differential attenuation, which we observe clearly in figure 4.16 to occur at the orthoexciton resonance, within probe laser bandwidth limits.

To support this model, we then look for NDA around the band edge. As discussed in section 3.1, the absorption profile in this region is much flatter than at resonance; the concept of line-broadening then becomes irrelevant. In figure 4.17, the transmitted signals I and I_p are measured for various wavelengths around the band edge; as predicted by the line-broadening model, no additional attenuation is detected at these wavelengths in the presence of a condensate. Likely, the observed NDA at resonance is in fact generated by the local crystal distortion induced by the passage of the exciton packet. NDA at resonance would then present a great means for detecting the passage of such packets. We thus continue our studies of NDA at resonance, with such parameters as probe intensity and wavelength, to verify this statement.

4.2.2 NDA Variations with both YAG and Secondary Laser Intensities

To support further the contention of packet-induced NDA, figures 4.18(a) and 4.18(b) [34] respectively plot NDA and unamplified condensate amplitude variations with YAG pulse intensity. Comparing trends in both graphs, it is observed that as the condensate increases in amplitude, so does the NDA. This indicates that the resulting additional attenuation is closely related to the amplitude of the initial condensate and thus to the number of excitons present in the probed volume. Inherently, if the travelling exciton-phonon packet increases in size, which is directly related to the initial YAG intensity, then the local crystal perturbation induced by the existence of this packet will likely also increase in intensity and in effective volume. Consistent with discussions of distortion-induced line-broadening, the larger the condensate, the larger the additional absorption. The above model then adequately explains the results observed in figure 4.18.

In figure 4.19(a) [34], the NDA is observed to remain constant as the secondary pulse intensity is varied over two orders of magnitude. Simply put, the NDA is in sorts, a measure of an increased effective local absorption coefficient induced by the condensate. Like any other optical absorption, NDA measures the probability that a resonant photon will be additionally absorbed, independent of the light intensity. Inherently, no matter how many resonant photons are injected into a given interaction volume, they will be

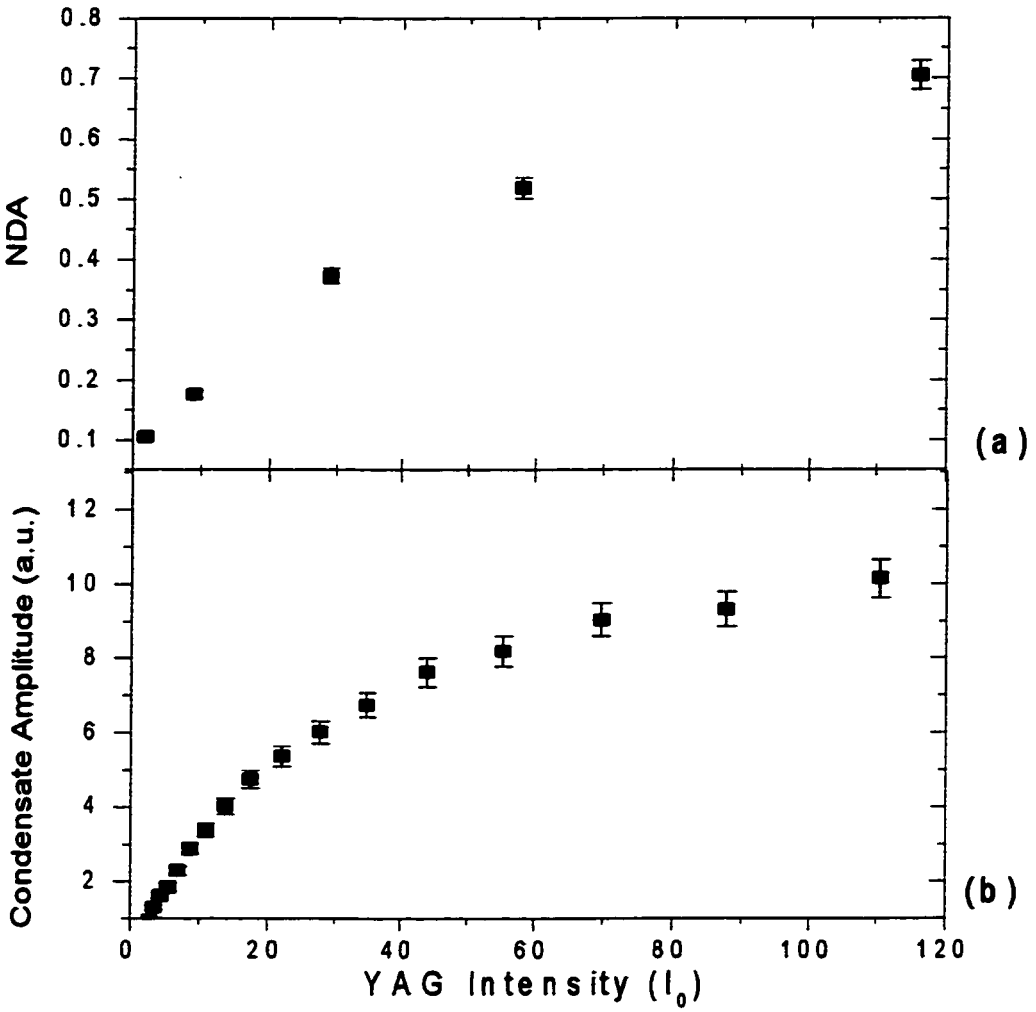

Figure 4.18: NDA (a) and condensate amplitude (b) variation with YAG pulse intensity. (Sample (1): $I_{Probe} \sim 0.3I_0$) [34]

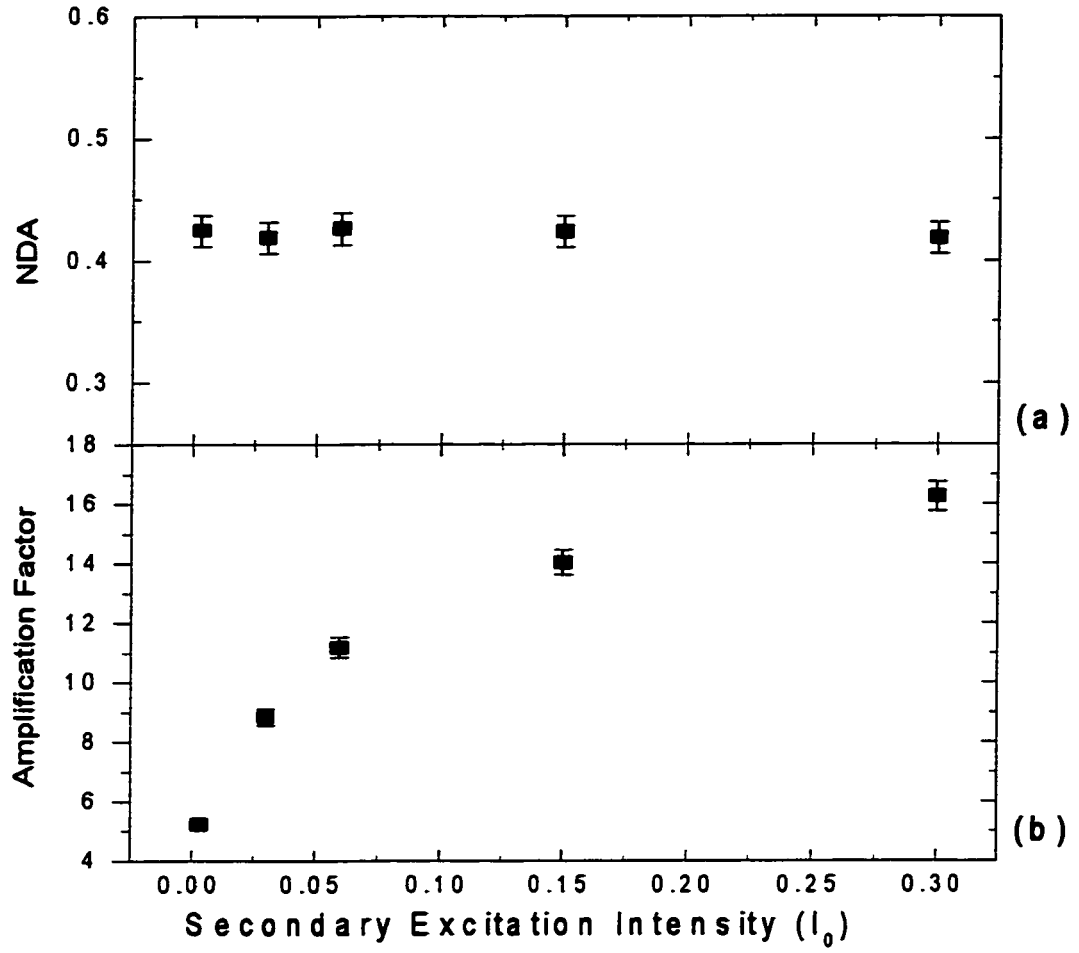

Figure 4.19: (a) NDA remains constant with resonant pulse intensity. Condensate amplification factor (b) increases with resonant pulse intensity. (Sample (1): $I_{YAG} \sim 100I_0$) [34]

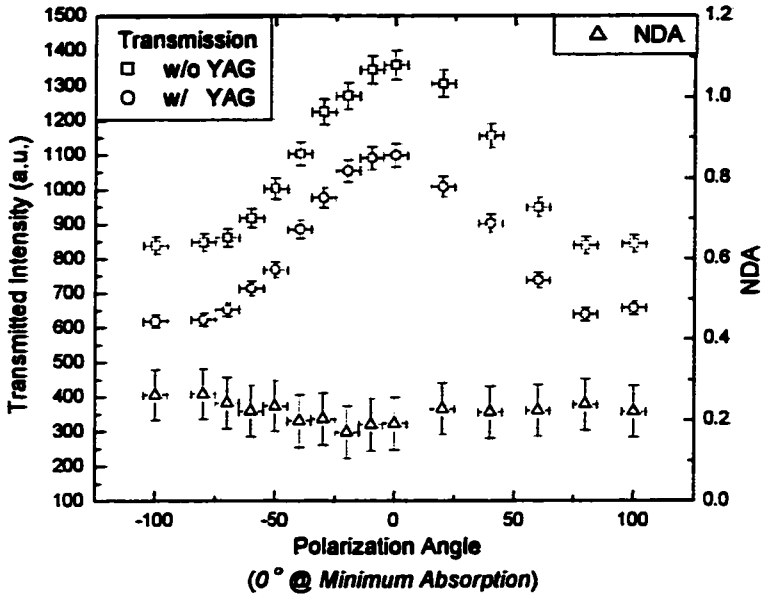

Figure 4.20: Transmission and NDA variation with resonant pulse light polarization along $[1\bar{1}0]$ axis. Transmitted intensities (open squares) and transmitted intensities in the presence of a condensate (open circles). The NDA (open triangles) remains relatively constant.

subjected to the same supplementary probability of absorption. The constant differential attenuation observed in figure 4.19(a) then comes as no surprise. Of course, if we accept that amplification is strictly related to the number of interacting excitons created within the condensate and its surrounding cloud of quasi-condensed excitons, then the increase in amplification with secondary pulse intensity depicted in figure 4.19(b) [34] is to be expected. Clearly, as more and more photons are additionally absorbed within the travelling packet, more and more excitons from the packet coma and tail can be induced to scatter into the condensate to amplify it. Hence, not only is NDA a great means for detecting the passage of a condensate, it can also help to study condensate amplification as both effects are closely related.

4.2.3 NDA Variations with Secondary Excitation Polarization

In this section, the NDA is studied as a function of resonant pulse light polarization. Essentially, variations with polarization should only be observed in signals dependent on the absorption of resonant light in the unperturbed crystal. As previously discussed in

section 4.1.3, where amplification was observed to remain relatively invariant with probe polarization, the local crystal distortion induced by the passage of the exciton packet can likely remove crystal symmetry within the packet volume, resulting in polarization-independent absorption in this interaction region. Additionally, if the NDA is a manifestation of a condensate-induced local increase in the effective absorption coefficient, which, following the above statement, would be polarization-independent, NDA itself should not display any variations with probe polarization.

In figure 4.20, the two top traces show the transmitted signals collected by the transverse optical fibre in the case where no condensate is present (upper trace) and in the case where the beam is intersected by the exciton packet. Both traces follow the squared sinusoidal shape expected by the absorption theory (section 2.3.1), maximizing transmission at the minimum absorption angle in both cases. What is interesting is that the NDA, as predicted above, remains relatively constant, independent of polarization. Even though the transmitted signals, both with and without the interceptive condensate, vary with polarization, the additional absorption remains constant. As discusssed in section 4.1.3, the crystal can be subdivided into two absorption regions: a region where the unperturbed crystal absorbs in the conventional way, respecting symmetry, and a distorted region where absorption is broadened, hence additionally absorptive, and where symmetry is broken. The transmitted signal in the presence of the condensate helps to illustrate both regions; the typical sinusoidal variation with polarization is induced by the unperturbed region, and the relatively constant drop in transmitted intensity is attributed to the absorption within the distortion volume. Once again, NDA is strictly linked to the passage of the condensate, and its invariance with polarization suggests at least an indirect implication in condensate amplification (as proposed in section 4.1.3).

4.2.4 Front Signal Normalized Differential Attenuation: F-NDA

Front Signal Normalized Differential Attenuation (F-NDA), is much like NDA, but instead of dealing with transmitted signals detected by the collecting optical fibre, it relates to the observed attenuation of front signals (section 3.2) in the presence of an excitonic condensate. Like NDA, F-NDA is defined as $(F - F_p)/F$ where $F\,(F_p)$ is the excitonic front signal amplitudes as detected by the exciton detector in the absence (presence) of an exciton packet. This subsection aims to characterize this F-NDA, and to show that it is simply another example of condensate-induced additional absorption.

Referring to section 3.2, we recall that the instantaneous and diffusive front signals

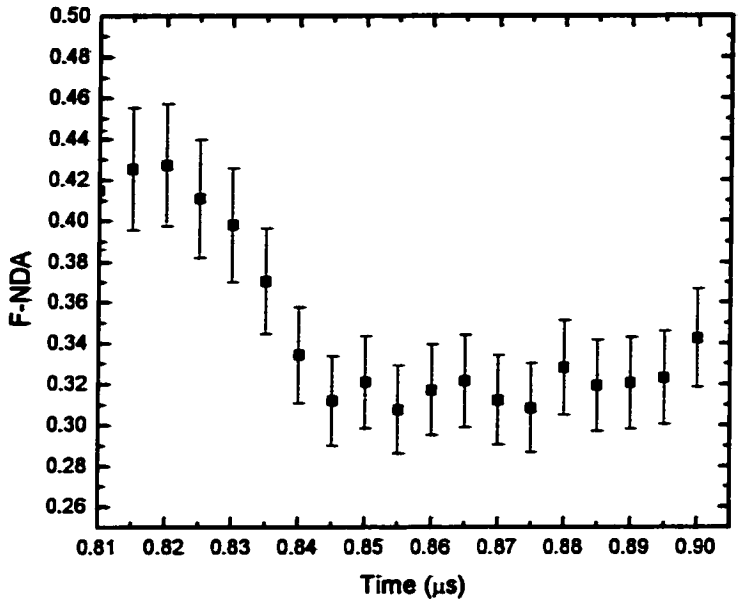

Figure 4.21: F-NDA measured at various points in the time-resolved front signals at resonance. The two reported sections illustrate the F-NDA effect on the instantaneous and diffusive front signals respectively.

are temporally resolvable, consisting of a sharp signal, followed by a diffusive tail. In figure 4.21, F-NDA is plotted for various points within a temporally resolved front signal generated by a secondary pulse tuned at resonance. Notice that two different regions can be selected; the first is attributed to the differential attenuation of the instantaneous front, and the other, of the diffusive tail. Although the reason for the difference in F-NDA values for the two front components is not entirely clear, it is likely related to the fact that the instantaneous F-NDA is more similar to NDA than its counterpart, as it measures direct light absorption at the electrodes. The diffusive F-NDA on the other hand is a little more complicated as one must take into account the diffusive exciton interactions with the travelling packet itself, which could inherently reduce the effect. In any case, both can serve the same purpose to study the local packet-induced crystal distortion.

In figure 4.22, the F-NDA measurements in figure 4.21 are plotted with secondary excitation detuning from resonance; the open squares and circles respectively measure F-NDA in the instantaneous and diffusive fronts. Both instantaneous and diffusive F-NDA, like NDA, are found to be strictly resonant with absorption. Clearly, if the lateral pulse is additionally absorbed at resonance by the travelling packet, then light scattered within

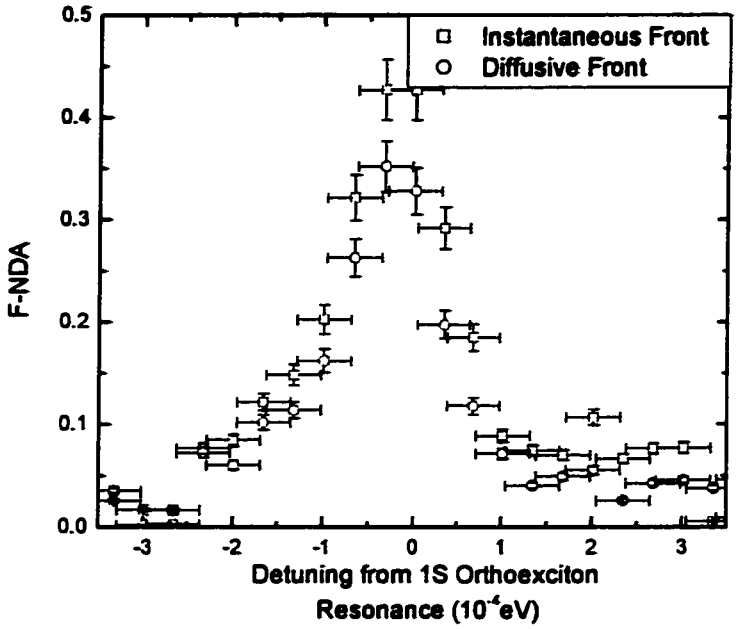

Figure 4.22: Instantaneous and diffusive F-NDA measured around the resonance. F-NDA, like NDA is a sharp resonant effect.

this interaction volume will also experience an additional absorption, hence the attenuated fronts. If this is the case, then F-NDA is simply NDA measured on the scattered light signal. The following arguments will support this concept, showing similarities in F-NDA and NDA variations with secondary pulse intensity and polarization.

In figure 4.23, front amplitudes F and F_p are plotted, along with their attributed F-NDA, with secondary pulse polarization. The two top traces show the front signal amplitudes measured by the exciton detector in the case where no condensate is present (upper trace) and in the case where the beam is intersected by the exciton packet. Both traces follow the squared sinusoidal shape observed in section 3.2.2, maximizing their intensity at the minimum absorption angle in both cases. The bottom trace plots their respective normalized differential attenuation, which remains relatively constant. Just like NDA, F-NDA is invariant with probe polarization. As discussed in section 4.2.3, the additional absorption generated by the passage of the exciton packet is invariant with polarization. The scattered light responsible for the front signals is then differentially attenuated by this distortion volume where polarization has no bearing on its absorption. Yet, the fronts still display their usual polarization dependence individually, as absorption along the secondary axis is still polarization-dependent outside the condensate interaction volume. Again, F-NDA, just as NDA, is shown to be another byproduct

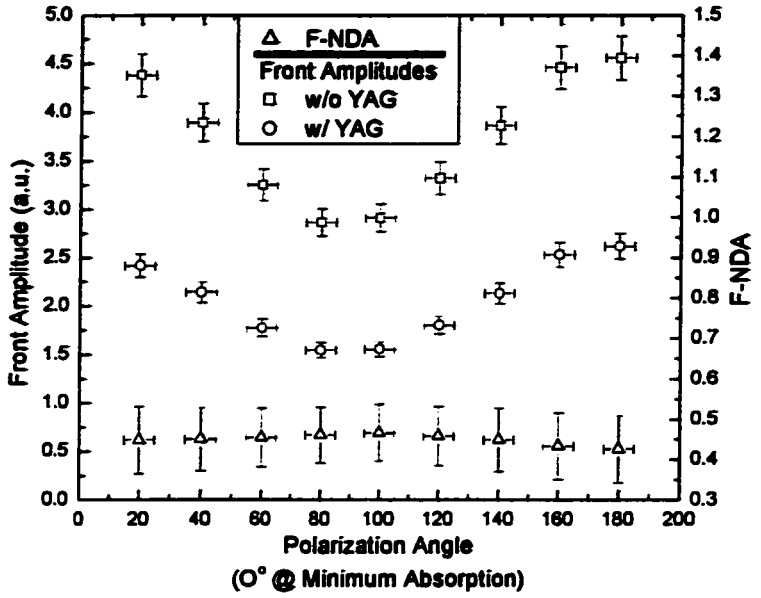

Figure 4.23: Like NDA, F-NDA remains relatively constant with secondary probe polarization.

of the condensate-induced line-broadening generated by a local symmetry-breaking crystal distortion.

Finally, in figure 4.24 the F-NDA is plotted for various secondary laser intensities; like the NDA, the F-NDA seems to remain relatively constant. As explained in section 4.2.2, no matter how many resonant photons interact with this distortion volume, they will be submitted to the same supplementary probability of absorption. Therefore, F-NDA remains invariant with secondary pulse intensity.

Clearly, considering the similarities in F-NDA and NDA variations with secondary pulse wavelength, polarization and intensity, we can conclude that they are measures of the same effect: a condensate-induced local line-broadening which produces an interaction volume of higher absorption. Any resonant light which penetrates this volume will experience the additional probability of absorption, whether the light is being transmitted through the crystal, or scattered toward the electrodes. In both cases, this differential attenuation provides a great means for condensate detection and analysis.

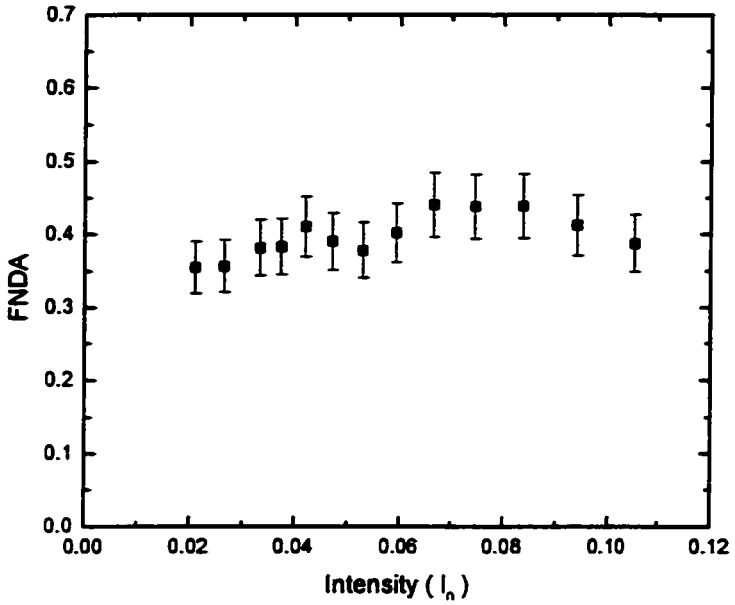

Figure 4.24: Like NDA, F-NDA remains relatively constant with secondary probe intensity.

Chapter 5

Final Discussion

This last chapter aims to put everything together, hoping to develop one model that can plausibly explain the results observed in chapters 3 and 4. Throughout this thesis, thoughts and ideas were presented as new results were brought forward; yet, although all the analyses provided were guided by one specific model which would encompass all the various observations made pertaining to our experiments, it is important to show all of the results together, clearly indicating the validity of the proposed model.

As mentioned throughout this work, the main interest in this research project is to qualify the various parameters that influence and govern condensate amplification. At the same time, probing experiments conducted on the condensates also provide interesting information on the travelling packet itself. Combining all of these results, both from recent experiments conducted by the author and from previous experiments conducted by Benson [6] and Massé [14], we arrive at a relatively complete view of the probe-condensate (or probe-packet) interactions that take place in our experiments. To properly present this model, and how it relates to our experimental observations, we divide this chapter into 3 sections. The first section will review the idea of single condensate propagation, and its effects on, and interaction with, the crystal itself; in essence, this brings forth the local sample distortion concept initiated in previous chapters. In the following section, NDA and F-NDA will be discussed with regards to this concept. Finally, the last section will review condensate amplification by lateral secondary pulse excitation.

5.1 Travelling Condensate and Crystal Distortion

As first presented in section 1.2.4, excitonic BEC is observed when particle densities, created at approximately $2\,K$ by YAG pulse illumination, reach a certain threshold. At

this point, the exciton packet condenses and travels ballistically through the crystal at velocities approaching the speed of sound in the crystal. Evidently, as excitons are created at the crystal surface, so are a great number of phonons; these must then be included when wanting to fully characterize our system. Nonetheless, even though phonons are present in all of our experiments, they do not hinder our ability to successfully observe and study excitonic Bose-Einstein condensation.

Now, although characterization of the initial condensate creation processes relates mainly to experimental parameters outside the crystal, such as bath temperature and YAG laser intensity, probe-condensate experiments must also consider what kind of effects the travelling comet-like exciton packet will induce in the crystal itself. Taking that into account will lead to a better understanding of such phenomena as NDA and condensate amplification.

When the condensate is created, both with its surrounding incoherent "coma" and "tail", it will travel toward the opposite crystal face, pushed by a density gradient; at the same time, a great number of phonons will also propagate throughout the crystal. What we propose is that the condensate will induce some type of local crystal "distortion", only to be observed in, and in the close vicinity of the travelling packet. This effect would not drastically change the crystal, but as will be put forth in the next section, it would be significant enough to induce such variations as absorption line-broadening and crystal symmetry breaking; much like external stresses on a crystal can alter some of its absorption properties, the energetic passage of an excitonic packet can locally distort our samples. We then consider how secondary probe pulses behave in this region, and how interactions lead to differential attenuation and condensate amplification.

5.2 NDA and F-NDA as Related to the Induced Crystal Distortion

When the probe pulse reaches the aforementioned distortion volume, it then interacts with modified crystal properties. For example, if the secondary excitation is tuned around the sharp 1S orthoexciton resonance, and if this absorption line is mildly broadened by the passage of an exciton packet, then an additional absorption of the exciting light is observed; essentially, the condensate interaction volume provides a region where the effective absorption coefficient (remember that the laser bandwidth is wider than the transition line width$\sim$ 60 : 1) is higher than throughout the rest of the crystal. This

thus explains NDA and F-NDA measurements at resonance. Transmitted and scattered light, which would otherwise be absorbed uniformly, now interacts locally with a region presenting a higher effective absorption coefficient, hence a greater total cumulative absorption is detected. Yet, when probing near the band edge where the absorption spectrum is flatter, line-broadening has no effect and there is no differential attenuation. This works well with our results.

Of course, to investigate the validity of this model, we must also use it to explain previous NDA and F-NDA results. For instance, [13] reports that NDA varies considerably with probe-condensate synchronization. If the secondary pulse reaches the crystal before the condensate reaches the excitation axis, the NDA is small. When both the probe and the condensate are synchronized to meet at the center of the crystal, the NDA reaches a maximum. Finally, if the probe arrives once the crystal has passed, it only interacts with the tail of the packet, which leads again to a weaker NDA. Not only does this provide a great method for detecting the passage and the shape of the travelling exciton packet, it provides a measure of the extent of the line-broadening induced locally in the crystal. As the packet travels across the probe interaction region, its effect on the crystal absorption will increase and decrease based on how much of the packet intercepts the transmitted probe pulses. The extent of the local crystal distortion is then proportional to the size of the initial packet, controlled by the YAG pulse intensity which determines the number of initial excitons and phonons that will propagate through the crystal, and hence to the quantity of excitons present in the packet at a given point within the crystal volume.

To further support the model, we look at NDA (F-NDA) variations with both YAG and secondary pulse intensities. In figure 4.18, we observe that the NDA increases with initial YAG intensity (the condensate and probe are synchronized); this is in good agreement with the proposed model. As the YAG intensity is increased, so is the initial exciton density, leading to a greater, more condensed packet. Likewise, the number of phonons also increases. Naturally, the greater the exciton-phonon packet, the greater the distorted interaction volume, and hence, the greater the NDA. On the other hand, increasing the secondary pulse intensity has no effect on reported NDA (and F-NDA) measurements (figure 4.19). This is because the interaction volume is the same for all probe intensities, and since the line-broadening only acts as an additional absorption coefficient, the probe experiences the same additional probability of absorption. This also explains the relatively constant NDA (and F-NDA) measurement made with probe light polarization.

Clearly, the concept of packet-induced crystal distortion, manifested by local absorption line-broadening, works well with all NDA and F-NDA results. Unfortunately, we still do not know whether NDA would persist were there fewer phonons created. In [14], work was done with condensates initially created with $585\,nm$ laser pulses instead of the usual YAG illumination ($532\,nm$). Since the excitation energy is lower at this new wavelength ($\sim 2.32\,eV$ as opposed to $\sim 2.11\,eV$), approximately one fourth of the phonons are generated (Number of phonons $\propto E_{Laser} - E_{Gap}$: $E_{585} - E_{gap} \approx 7\,meV$, $E_{532} - E_{gap} \approx 28\,meV$). NDA measurements with such an initial excitation could then help to determine whether the packet-induced crystal distortion is attributed to the excitons or to the phonons. Unfortunately, such experiments would require two dye lasers, one at $585\,nm$ to create the initial condensate and one at $609.51\,nm$ to probe and amplify it; our lab has only one. Yet, despite this uncertainty, we know that NDA provides a great means for detecting and studying the passage of high density exciton packets in our experiments.

5.3 Condensate Amplification: How it Works

When the condensate is probed by a secondary pulse, either tuned at the orthoexciton resonance, or again near the exciton band edge, drastic condensate amplifications are observed. If our model is correct, amplification related results will show that the probe interacts with the crystal locally, within the distortion volume, to produce the gains in excitonic signals.

Amplification only occurs either at resonance, or near the band edge. In other words, light must first be absorbed into the crystal, creating paraexcitons (processes discussed in section 1.2.2) that can then interact with the travelling packet to amplify it. A photon-exciton interaction is an unlikely mechanism for amplification even when probing at resonance as the resonant pulse energy corresponds to the orthoexciton, and not to the less energetic paraexciton ($12\,meV$ lower). Amplification is more likely attributed to the creation of paraexcitons directly in the interaction volume, that are then trapped by the condensate potential, inducing the further condensation of neighboring quasi-condensed excitons travelling within the comet-like packet coma and tail.

To verify this contention, we must look at how our secondary pulses behave once they enter our sample. Part of the probe is absorbed directly along the secondary axis, outside the aforementioned distortion volume, another part is absorbed locally within the travelling packet's interaction volume, a third part will be scattered, namely in the direction of the electrodes to produce the observed front signals (section 3.2), and finally,

some of the light is transmitted through the crystal and can be collected by an optical fibre. Studying amplification, as well as the packet-induced differential attenuation of these light pulses, we can isolate which excitons actively participate in the amplification process.

After a thorough study of the instantaneous and diffusive front signals with probe wavelength, polarization and relative time-delay, we conclude that the excitons responsible for these signals are not predominant in amplification. Although we can observe front-induced signals in detected amplified condensates for certain experimental configurations, they are of much interest. For example, we observed in sections 4.1.1 and 4.1.3 that as the front signal was reduced, either by probing the initial packet at lower wavelengths (figure 4.6), or again by varying the resonant probe polarization (figure 4.10), we could considerably reduce the observed front-induced shoulder in the detected exciton signals, without considerably changing the amplified condensate. Furthermore, as the probe-condensate delay was changed to reduce the front's interaction with the amplified condensate (figures 4.12 and 4.13), the additional front-induced signal disappeared. This suggests that the excitons created along the main axis by the scattered part of the probe pulse are not important in the condensate amplification process of interest . This thus leaves us with the investigation of excitons directly created along the secondary axis, either outside, or within the initial packet, the excitons likely responsible for the amplification phenomenon of interest

To study amplification in relation to optical absorption along the secondary axis, many experimental tools and techniques can be utilized. For starters, one seeks to differentiate between optical absorption outside and inside the travelling packet. This was achieved using polarization-dependent absorption in sample (F) in conjunction with the packet-induced local crystal distortions observed through NDA (F-NDA). Comparing transmitted signals in the presence and in the absence of an interceptive exciton packet, one observes that the measured NDA, likely related to a packet-induced absorption line broadening, is also polarization-independent (figures 4.20 and 4.23). In conjunction with the simple calculations presented in section 4.1.3, we can explain why no amplification variation with probe polarization is observed. These results show clearly that amplification is mainly, if not entirely induced by the direct absorption of excitons created within the packet-induced local crystal distortion volume, which stimulate the further condensation of incoherent excitons in the comet-like packet coma and tail.

Conclusion

Experimental results were presented on excitonic effects related to the Bose-Einstein condensation (BEC) of excitons in Cu_2O. Such effects included resonant light polarization dependent absorption, exciton creation and diffusion by absorption of scattered light, and resonant exciton induced absorption. These results were then utilized, in conjunction with similar results on excitonic BEC, to better isolate the various parameters that govern and influence Bose condensate amplification. Condensates were initially created at T=1.8K with high intensity ND:YAG pulses ($\lambda = 532\,nm$) and then stimulated laterally by a secondary source tuned around the 1S orthoexciton resonance ($\lambda = 609.51\,nm$); the latter induces the observed condensate amplifications. By careful analysis of the various interactions between the secondary light source, the crystal, and the condensate itself, an improved understanding of how the secondary pulse excitations interact with the passage of a high density exciton packet is obtained.

In the first chapter, we discussed the various theoretical concepts related to our experimental system that were required to attain an adequate level of understanding of the various interactions that take place in our samples. At first, basic BEC theory was covered to be then applied to an excitonic system in our Cu_2O samples; this was complemented by a discussion of Bose condensate amplification. It was presented that our travelling excitonic condensate, accompanied by an intense phonon field, would locally perturb the crystal so as to induce symmetry-breaking absorption line-broadening within a given interaction volume delimited by the exciton packet itself. It was proposed that excitons, created within this interaction volume, were the most likely cause for amplification; as the cold excitons are created within the travelling packet, they will further induce the condensation of neighboring incoherent excitons travelling within the comet-like packet coma and tail, hence the drastically amplified signals. In chapter 2, we reviewed the various experimental techniques and equipment utilized in our studies, offering an overview of all sample preparations and setups. Then came the results.

Chapter 3 presented the first of the results, covering single laser experiments required

to adequately characterize the interactions and effects related to the stimulation of our samples with near resonance optical pulses. We first discussed the various absorption properties of our crystals in the spectral region of interest, namely at wavelengths around the 1S orthoexciton resonance. We showed that we could adequately vary the resonant absorption coefficient along certain crystal axes by rotating the probe's polarization. We then proceeded to study excitonic signals generated by the scattered part of the probe pulses, which was absorbed within the crystal volume, and detected at the exciton detector. These signals, termed fronts, are comprised of three components, an instantaneous signal generated within the detector electrodes themselves, an instantaneous signal generated by the absorption of light directly at the detector surface, and a diffusive excitonic signal generated by the diffusion of excitons created along the main axis. These front signals were also shown to vary with probe polarization. When more light is absorbed, less is available for scattering, and the fronts are smaller; when less light is absorbed, more is available for scattering, and the fronts are larger. The study of absorption and of scattered front signals in the spectral range of interest provided useful tools in the following chapter for the study of condensate amplification.

In the next chapter, condensate-probe interactions were investigated. Condensates created with an initial YAG pulse were probed by a secondary pulse tuned either around the exciton resonance or near the exciton absorption edge. By varying the probe wavelength, intensity and polarization, we adequately characterized various parameters involved in the observed gains in exciton packet signals. For starters, front-induced effects detected within our amplified condensate signals were shown to be of secondary interest in the actual direct Bose condensate amplification phenomenon of interest. We showed that excitons, created by scattered light along the crystal main axis did not participate in the amplification process per say, but actually appeared to amplify the front of the incoherent coma of the travelling comet-like packet, generating the observed front-induced shoulder in detected excitonic condensate signals. Likewise, it was presented that only excitons created within the condensate interaction volume induce the direct condensate amplification of interest. Using results on amplification variations with probe intensity, we explained that even though absorption may be polarization-dependent along certain crystal axes, observation of polarization variations in amplification could not be expected. We then turned to NDA and F-NDA for further information on condensate amplification and condensate-induced effects.

For starters, the observation of differential attenuations of the lateral probes indicates that the passage of a high density exciton packet, accompanied by a strong phonon

field, induces some local perturbations in our crystals. These are manifested by local symmetry-breaking optical absorption line-broadening, and observed through probe polarization and intensity independent NDA and F-NDA. We have seen that as NDA increases, either with probe delay or initial YAG intensity, so does the amplification. In addition, we observe that the NDA can be considered as a simple localized increase in the effective absorption coefficient; as the lateral pulse intensity is increased, the NDA remains constant, but the amplification increases as more and more photons, all subjected to the same additional probability of absorption, can be absorbed within the initial packet volume to induce the condensate amplification process. NDA then provides a window onto how the secondary pulses behave in the presence of a high density exciton packet.

In the fifth and last chapter, a final analysis of results needed to formulate a plausible model believed to adequately explain condensate amplification is presented. It incorporates results, both from the present paper and from previous works by Benson [6] and Massé [14], on amplification and on NDA, leading to a clearer understanding of how the secondary pulse excitations interact with the passage of a high density exciton packet. Briefly, excitons created directly within the travelling exciton packet volume, encouraged by the local symmetry-breaking line-broadening effects generated by the packet itself, will scatter into the condensed state and induce the further condensation of neighboring incoherent excitons travelling within the comet-like packet coma and tail; the latter will generate the drastic condensate amplifications detected in our experiments.

The local addition of cold excitons in the travelling packet acts as the triggering element for amplification. The incoherent cloud of quasi-condensed cold exctions that travels with the initial packet needs only a small increase in density to condense. As observed in previous experiments [6, 14] seeking to characterize excitonic condensate formation by single YAG pulse excitation, only a small increase in the initial YAG pulse intensity is required to pass from the creation of a diffusive packet to the creation of a ballistic condensate. Likewise, once the initial packet is created in our condensate amplification experiments, the modest addition of cold excitons to the initial packet by means of a secondary excitation will further entice the condensation of the nearly condensed cloud of incoherent excitons that surround the travelling condensate. Excitonic Bose-Einstein condensate amplification is thus predicted to result from the injection of cold excitons directly within a high density exciton packet; these newly injected excitons then stimulate the further condensation of incoherent excitons travelling with the initial packet, producing the drastic gains in measured excitonic condensate signals.

Bibliography

[1] A. Griffin, D.W. Snoke and S. Stringari, *Bose-Einstein Condensation*, Cambridge University Press, Cambridge, 1995.

[2] S.A Moskalenko and D.W. Snoke,*Bose-Einstein Condensation of Excitons and Biexcitons: and Coherent Nonlinear Optics with Excitons*, Cambridge University Press, Cambridge, 2000.

[3] E. Benson, E. Fortin and A. Mysyrowicz, *Phys. Stat. Sol. (b)*, **191**, 345 (1995).

[4] E. Benson, E. Fortin, B. Prade and A.Mysyrowicz, *Europhys. Lett.*, **40**(3), 311 (1997).

[5] A. Mysyrowicz, E. Benson and E. Fortin, *Phys. Rev. Lett.*, **77**, 896 (1996).

[6] E. Benson, *Ph.D. dissertation*, 140 (1999).

[7] I. Loutsenko and D. Roubtsov,*Phys. Rev. Lett.*, **78**, 3011 (1997).

[8] G.A. Kopelevich, N.A. Gippius and S.G. Tikhodeev, *Solid State Commun.*, **99-2**, 93 (1996).

[9] A.R. Vasconcellos, M.V. Mesquita and R. Luzzi, *Europhys. Lett.*, **49**, 637 (2000).

[10] G.M. Kavoulakis and A. Mysyrowicz, *Phys. Rev. B*, **61-24**, 16619 (2000).

[11] O.M. Schmitt, D.B. Tran Thoai, L. Bànyai, P. Gartner and H. Haug, *Phys. Rev. Lett.*, **86**, 3839 (2001).

[12] D. Roubtsov and Y. Lépine, *Phys. Rev. B*, **61**, 5237 (2000).

[13] E. Fortin and M. Massé, *Proceeding of International Conference on Excitonic Processes in Condensed Matter (Osaka, August 2000)*, World Scientific, 31-37 (2001).

[14] M. Massé, *M.Sc. dissertation*, 82 (2001).

[15] N. Caswell, J.S. Weiner and P.Y. Yu,*Solid State Commun.*, **40**, 843 (1981).

[16] M. Kavoulakis, G. Baym and J.P. Wolfe, *Phys. Rev. B*, **53**, 7277 (1996).

[17] D. Fröhlich, A. Kulik, B. Uebbing, *Phys. Rev. Lett*, **67**, 2343 (1991).

[18] M. Certier, *M. Sc. Dissertation*, 167 (1967).

[19] D.W. Snoke, A.J. Shiels and M. Cardona,*Phys. Rev. B*, **45**, 11693 (1992).

[20] A.I. Bobrysheva and S.A. Moskalenko,*Phys. Status Solidi (b)*, **119**, 141 (1983).

[21] D.W Snoke, J.P. Wolfe and A. Mysyrowicz, *Phys. Rev. Lett.*, **64**, 2543 (1990).

[22] E. Hanamura and H. Haug,*Phys. Rep. C*, **33**, 209 (1977).

[23] A. Imamoglu, R. J. Ram, S. Pau, and Y. Yamamoto,*Phys. Rev. A*, **53**, 4250 (1996).

[24] D. Snoke, J.P. Wolfe, and A. Mysyrowicz, *Phys. Rev. B*, **41**, 11171 (1990).

[25] D. Hulin, A. Mysyrowicz and C. Benoit a la Guillaume, *Phys. Rev. Lett.*, **45**, 1970 (1980).

[26] D. Snoke, J.P. Wolfe, and A. Mysyrowicz, *Phys. Rev. Lett.*, **59**, 827 (1987).

[27] A. Mysyrowicz, D. Snoke and J.P. Wolfe, *Phys. Stat. Sol. (b)*, **159**, 387 (1990).

[28] E. Tselepis, E. Fortin and A. Mysyrowicz, *Phys. Rev. Lett.*, **59**, 2107 (1987).

[29] L.C. Olsen and R.C. Bohara, *Appl. Phys. Lett.*, **34**, 47 (1979).

[30] E. Fortin and W.M. Sears, *Can. J. Phys.*, **60**, 901 (1982).

[31] J. Bardeen, *Phys. Rev.*, **71**, 717 (1947).

[32] C. Olsen, F.W. Addis and W. Miller, *Solar Cells*, **7**, 247 (1982-1983).

[33] A.A. Berezin and F.L. Weichman, *Phys. Stat. Sol. (a)*, **71**, 265 (1992).

[34] A. Merizzi, M. Massé and E. Fortin *Solid State Communications*, **120-11**, 419 (2001).

[35] A. Jolk, M. Jörger, C.F. Klingshirn, M. Franco, B. Prade and A. Mysyrowicz, *Phys. Stat. Sol. (b)*, **221**(2000).